# Fractional-N PLL-Based Waveform Synthesis for FMCW SAR


**Thomas Gwasira**

Department of Electrical Engineering
University of Cape Town
South Africa

*Supervisors:*
Dr. Stephen Paine &
Prof. Emer. Michael Raymond Inggs

**April 30, 2024**

Submitted to the Department of Electrical Engineering at the University of Cape Town in partial fulfillment of the academic requirements for the degree of Master of Science in Electrical Engineering

This page is intentionally left blank.

# Declaration

I know the meaning of plagiarism and declare that all the work in the document, save for that which is properly acknowledged, is my own. This thesis/dissertation has been submitted to the Turnitin module (or equivalent similarity and originality checking software) and I confirm that my supervisor has seen my report and any concerns revealed by such have been resolved with my supervisor.

Signed by candidate

Thomas Gwasira

Department of Electrical Engineering
University of Cape Town

Tuesday 30th April, 2024

# Abstract

Achieving high-quality transmitted and local oscillator signals is a core objective in the design and implementation of high-resolution radar imaging systems, as the reconstructed images depict the interaction of the signals with elements in the scene.

This dissertation concerns optimisation of the imaging capabilities of a frequency modulated continuous wave (FMCW) synthetic aperture radar (SAR) system, named the miloSAR, by improving the frequency synthesis aspects of the system. This is done by considering the phase-locked loop (PLL) synthesiser employed and waveforms, thereof, in terms of dynamic response characteristics and frequency response characteristics.

The dynamic response component entails studying parameters which include the modulation period, modulation bandwidth, sweep rate, pulse repetition frequency (PRF) and slew rate among others and their influence on SAR image quality of the system in question.

It was discovered that to better the performance of the system as it relates to these parameters, the radar system and the synthesiser had to be modelled and characterised in order to realise more optimal waveforms such as the sawtooth waveform which previously was not possible owing to limited information on the PLL's dynamics. Furthermore, the signal acquisition system was redesigned to increase the data rate of the system from 11 MB/s to 43.231 MB/s, thus, allowing support for higher PRFs and sample rates.

Frequency response characteristics involve stability of both the synthesiser and the generated waveforms. The main issues related to this were identified to be ramp non-linearity, spurs and phase noise. Phase noise was the primary concern for this work since sufficient ramp linearity was achieved by the synthesiser and spurs have been addressed in another author's work on the miloSAR.

Two independent synthesisers were, in fact, used to realise the heterodyne architecture required for the miloSAR and they were observed to exhibit significant phase instability. Due to the range correlation filtering effect achieved by using the same clock as the

reference inputs of the PLLs and the ADC clock, phase noise caused by strong targets was considered to be less of a concern. However, the phase noise skirt of antenna leakage was identified as a major cause of performance degradation since the leakage is high in power and its phase noise skirt, in regions where range correlation filtering does not occur, swamps weaker radar returns. This becomes an even bigger problem when the PLL bandwidth is increased to improve the PLL's dynamics.

The insights from both perspectives of the waveform synthesis problem were combined to give an instructive conclusion on how waveform synthesis must be carried out for the miloSAR and recommendations for a more performant system were proposed.

# Acknowledgements

My postgraduate journey has been an incredible one with its challenges, triumphs, and countless moments of personal and intellectual growth. For all the good stuff, I have so many people to thank.

First and foremost, I would like to thank my supervisors Dr. Stephen Paine and Prof. Michael Inggs.

Stephen for being the catalyst for my interest in the exhilarating world of radar. I am forever grateful for assistance with obtaining funding to pursue my master's, all the opportunities you have provided me with and for all the good times — the trips, the dinners, the braais and everything else. But most importantly, I am grateful for the academic guidance and support — sharing your expertise and getting me everything I required at lightning speed. I could not have asked for a better supervisor.

Michael, it was an incredible honour to work with such a renowned legend. Thank you for the opportunity to work on the miloSAR, for financial support along the way, and for being my reference. But most importantly, thank you for the academic support and for everything I've learned from you about SAR.

I would like to acknowledge the droneSAR team (past and present): Darryn Jordan, Jonathan Inggs, Tlotliso Mapana and Kevin Gema for the help with acquiring and processing the data, with the hardware, as well as for the memories at Oudtshoorn.

I am incredibly grateful to my friends Grant Norrie, Zamuxolo Solomon, Zaheer Dhunny, all my favourite gym bros and everyone I have not mentioned for making my postgraduate experience as fun as it was.

Last but not least, I would like to thank my family: everyone in the entire clan that has supported me but most importantly, my mom, dad, sister and little brother for your unwavering love and belief in me.

# Contents

# List of Figures

# List of Tables

# List of Acronyms and Abbreviations

**ACF** Autocorrelation function 69

**ADC** Analog-to-digital converter 7, 10, 12, 23, 26, 27, 61, 76, 83, 100, 101, 111, 114

**ADS** Automated driving systems 1

**AMBR** Ambiguity ratio 33

**BPF** Band pass filter 22, 25, 26

**CF** Compact flash/ Chop factor 21, 27, 65

**CMOS** Complementary metal oxide semiconductor 43, 47

**CNR** Clutter to noise ratio 34

**CP** Compression point 25, 43

**CPG** Charge pump gain xii, xiv, 24, 44, 52–58, 63, 85–87, 93, 98, 99, 105, 108, 113, 116, 117

**CPI** Coherent processing interval 31, 62, 95

**CPU** Central processing unit 21

**CW** Continuous wave 10, 20

**DAC** Digital-to-analogue converter 17

**DC** Direct current 26

**DCR** Direct conversion receiver 15

**DDC** Digital downconverter 27

**DDS** Direct digital synthesis/ Direct digital synthesiser x, 8, 9, 16–21, 27

**DF** Decimation factor 27

**DFT** Discrete Fourier transform 10

**DR** Data rate 25, 28

**DSP** Digital signal processing 12

**DUT** Device under test 104

**DVGA** Digital variable gain amplifier 26

**EMI** Electromagnetic interference 5, 11

**EVM** Error vector magnitude 68

**FFT** Fast Fourier transform 10, 30, 32, 59, 60, 62, 71, 91, 92

**FIR** Finite impulse response xi, 27, 78, 79

**FM** Frequency modulation 10

**FMCW** Frequency modulated continuous wave x, 1, 2, 4–6, 9–11, 13, 14, 16, 19, 20, 23, 25, 26, 30, 37, 42, 55, 59, 63, 64, 70, 76, 77, 81, 85, 98, 101, 108, 115–118

**FPGA** Field programmable gate array 17, 21, 27, 28

**FTL** Flash translation layer 21

**FVT** Final value theorem 58

**GMTI** Ground moving target indication 62

**IBS** Integer boundary spurs 66

**IF** Intermediate frequency xii, xiii, 3, 4, 7, 12–15, 20, 22, 23, 25, 26, 28, 30, 31, 39, 60, 64, 76, 81–83, 98–106, 108, 110, 111, 113, 114, 118

**IIR** Infinite impulse response 78

**IP** Intellectual property 27

**IP** Internet protocol 7, 28, 29, 41, 88, 89, 116

**IPN** Integrated phase noise 68

**IPR** Impulse response x, xii, 36–38, 84, 89–95, 100, 113

**IQ** Image quality 22, 37, 41, 89

**ISR** Integrated sidelobe ratio 33, 38, 91

**LFM** Linear frequency modulation 16, 58, 91

**LNA** Low noise amplifier x, 15, 25

**LO** Local oscillator 13, 15

**LPF** Low pass filter 27, 63, 72

**LTI** Linear time-invariant 36

**MMC** Multi-media card 7, 28, 41

**MNR** Multiplicative noise ratio 33, 38

**MOS** Metal oxide semiconductor 45

**NCI** Noncoherent integration 39

**OLTF** Open-loop transfer function 50

**PA** Power amplifier x, 12, 16

**PCB** Printed circuit board 19

**PDF** Probability density function 105

**PF** Pre-summing factor 24, 27

**PFD** Phase frequency detector 43–45, 49, 50, 57, 58

**PFS** Primary fractional spurs 66

**PLL** Phase-locked loop x–xiv, 3–9, 13, 16–19, 21–25, 42–56, 58, 59, 62–66, 69, 71, 73–75, 78, 80, 82, 84–87, 98–102, 104, 105, 108–114, 116–118

**PRF** Pulse repetition frequency xii, xiv, 2, 3, 7, 19, 20, 24, 25, 27, 28, 40, 41, 59–63, 84, 89, 90, 94–97, 109, 113, 115, 116

**PRI** Pulse repetition interval 14, 60, 85

**PSD** Power spectral density xiii, 33, 67–71, 82, 102–106

**PSF** Point spread function 36

**PSR** Point spread response/ Peak sidelobe ratio 36, 38, 91, 119

**PTCR** Point target contrast ratio 39

**QNR** Quantisation noise ratio 33

**RBW** Resolution bandwidth 101

**RCS** Radar cross section 33, 35, 36, 38, 101, 104, 108, 114

**RDA** Range-Doppler algorithm 30, 32

**RDM** Range-Doppler map 32

**RF** Radio frequency 10, 14, 15, 25

**RMS** Root mean square 67, 68, 74

**RPC** Reflected power canceller 12

**RRE** Radar range equation 35

**RVP** Residual video phase 31

**SAR** Synthetic aperture radar xii, 1, 2, 4–7, 9, 19–22, 28, 30, 32, 35–39, 41, 42, 59, 61, 66, 76–80, 83, 84, 89, 91, 95–98, 100, 101, 103, 105, 108, 115–118

**SBR** Signal-to-background ratio 32, 102, 114, 116, 118

**SCR** Signal-to-clutter ratio 7, 35, 39, 104, 118

**SFS** Sub-fractional spurs 66

**SNR** Signal-to-noise ratio 2, 3, 7, 27, 30, 31, 35, 56, 68, 80, 92, 95, 98, 113, 116

**SPC** Stationary point concentration 12

**SR** Short-range 11

**SSB** Single sideband 67

**SSD** Solid state drive 26

**TCP** Transmission control protocol 7, 28, 29, 41, 88, 89, 116

**UAS** Unmanned aerial system 20

**UAV** Unmanned aerial vehicle 1, 2, 5, 19, 102

**UDP** User datagram protocol 28, 29

**USB** Universal serial bus 21

**VCO** Voltage controlled oscillator xii, 13, 16, 17, 43, 45–47, 49, 52, 57, 63, 66, 69, 71, 74, 82, 85–87, 98, 99, 110, 111

**WOSA** Welch's overlapped segmented average 70

**WSS** Wide-sense stationary 69

# List of Terms

**ACF** Autocorrelation function 69

**ADC** Analog-to-digital converter 7, 10, 12, 23, 26, 27, 61, 76, 83, 100, 101, 111, 114

**ADS** Automated driving systems 1

**AMBR** Ambiguity ratio 33

**BPF** Band pass filter 22, 25, 26

**CF** Compact flash/ Chop factor 21, 27, 65

**CMOS** Complementary metal oxide semiconductor 43, 47

**CNR** Clutter to noise ratio 34

**CP** Compression point 25, 43

**CPG** Charge pump gain xii, xiv, 24, 44, 52–58, 63, 85–87, 93, 98, 99, 105, 108, 113, 116, 117

**CPI** Coherent processing interval 31, 62, 95

**CPU** Central processing unit 21

**CW** Continuous wave 10, 20

**DAC** Digital-to-analogue converter 17

**DC** Direct current 26

**DCR** Direct conversion receiver 15

**DDC** Digital downconverter 27

**DDS** Direct digital synthesis/ Direct digital synthesiser x, 8, 9, 16–21, 27

**DF** Decimation factor 27

**DFT** Discrete Fourier transform 10

**DR** Data rate 25, 28

**DSP** Digital signal processing 12

**DUT** Device under test 104

**DVGA** Digital variable gain amplifier 26

**EMI** Electromagnetic interference 5, 11

**EVM** Error vector magnitude 68

**FFT** Fast Fourier transform 10, 30, 32, 59, 60, 62, 71, 91, 92

**FIR** Finite impulse response xi, 27, 78, 79

**FM** Frequency modulation 10

**FMCW** Frequency modulated continuous wave x, 1, 2, 4–6, 9–11, 13, 14, 16, 19, 20, 23, 25, 26, 30, 37, 42, 55, 59, 63, 64, 70, 76, 77, 81, 85, 98, 101, 108, 115–118

**FPGA** Field programmable gate array 17, 21, 27, 28

**FTL** Flash translation layer 21

**FVT** Final value theorem 58

**GMTI** Ground moving target indication 62

**IBS** Integer boundary spurs 66

**IF** Intermediate frequency xii, xiii, 3, 4, 7, 12–15, 20, 22, 23, 25, 26, 28, 30, 31, 39, 60, 64, 76, 81–83, 98–106, 108, 110, 111, 113, 114, 118

**IIR** Infinite impulse response 78

**IP** Intellectual property 27

**IP** Internet protocol 7, 28, 29, 41, 88, 89, 116

**IPN** Integrated phase noise 68

**IPR** Impulse response x, xii, 36–38, 84, 89–95, 100, 113

**IQ** Image quality 22, 37, 41, 89

**ISR** Integrated sidelobe ratio 33, 38, 91

**LFM** Linear frequency modulation 16, 58, 91

**LNA** Low noise amplifier x, 15, 25

**LO** Local oscillator 13, 15

**LPF** Low pass filter 27, 63, 72

**LTI** Linear time-invariant 36

**MMC** Multi-media card 7, 28, 41

**MNR** Multiplicative noise ratio 33, 38

**MOS** Metal oxide semiconductor 45

**NCI** Noncoherent integration 39

**OLTF** Open-loop transfer function 50

**PA** Power amplifier x, 12, 16

**PCB** Printed circuit board 19

**PDF** Probability density function 105

**PF** Pre-summing factor 24, 27

**PFD** Phase frequency detector 43–45, 49, 50, 57, 58

**PFS** Primary fractional spurs 66

**PLL** Phase-locked loop x–xiv, 3–9, 13, 16–19, 21–25, 42–56, 58, 59, 62–66, 69, 71, 73–75, 78, 80, 82, 84–87, 98–102, 104, 105, 108–114, 116–118

**PRF** Pulse repetition frequency xii, xiv, 2, 3, 7, 19, 20, 24, 25, 27, 28, 40, 41, 59–63, 84, 89, 90, 94–97, 109, 113, 115, 116

**PRI** Pulse repetition interval 14, 60, 85

**PSD** Power spectral density xiii, 33, 67–71, 82, 102–106

**PSF** Point spread function 36

**PSR** Point spread response/ Peak sidelobe ratio 36, 38, 91, 119

**PTCR** Point target contrast ratio 39

**QNR** Quantisation noise ratio 33

**RBW** Resolution bandwidth 101

**RCS** Radar cross section 33, 35, 36, 38, 101, 104, 108, 114

**RDA** Range-Doppler algorithm 30, 32

**RDM** Range-Doppler map 32

**RF** Radio frequency 10, 14, 15, 25

**RMS** Root mean square 67, 68, 74

**RPC** Reflected power canceller 12

**RRE** Radar range equation 35

**RVP** Residual video phase 31

**SAR** Synthetic aperture radar xii, 1, 2, 4–7, 9, 19–22, 28, 30, 32, 35–39, 41, 42, 59, 61, 66, 76–80, 83, 84, 89, 91, 95–98, 100, 101, 103, 105, 108, 115–118

**SBR** Signal-to-background ratio 32, 102, 114, 116, 118

**SCR** Signal-to-clutter ratio 7, 35, 39, 104, 118

**SFS** Sub-fractional spurs 66

**SNR** Signal-to-noise ratio 2, 3, 7, 27, 30, 31, 35, 56, 68, 80, 92, 95, 98, 113, 116

**SPC** Stationary point concentration 12

**SR** Short-range 11

**SSB** Single sideband 67

**SSD** Solid state drive 26

**TCP** Transmission control protocol 7, 28, 29, 41, 88, 89, 116

**UAS** Unmanned aerial system 20

**UAV** Unmanned aerial vehicle 1, 2, 5, 19, 102

**UDP** User datagram protocol 28, 29

**USB** Universal serial bus 21

**VCO** Voltage controlled oscillator xii, 13, 16, 17, 43, 45–47, 49, 52, 57, 63, 66, 69, 71, 74, 82, 85–87, 98, 99, 110, 111

**WOSA** Welch's overlapped segmented average 70

**WSS** Wide-sense stationary 69

# Chapter 1

# Introduction

Radar imaging has emerged as a powerful remote sensing technology, distinguished from its optical-based counterparts by characteristics such as operability in the absence of light and penetrative capabilities.

The challenges of achieving reliability, ease of use and accessibility are, however, daunting and have precluded its adoption as a mainstream imaging approach. With that said, several advancements in the state of the art of radar imaging have begun fostering its rise to prominence.

One such development is the frequency modulated continuous wave (FMCW) radar concept which, unlike traditional pulsed radar systems, can achieve high resolution at an appreciably low transmit power. Marrying this technique with synthetic aperture radar (SAR) allows for the realisation of light, low cost, high resolution imaging systems with a wide range of exciting applications such as precision agriculture, scenario perception in automated driving systems (ADS), unmanned aerial vehicle (UAV) surveillance, and many others.

This has motivated the implementation of an S-band FMCW radar system named the miloSAR to be deployed on UAVs and light, fixed wing aircraft.

## 1.1 Background to Study

Developed by Tchekashkin [1] and Jordan [2], the miloSAR is a time-offset, FMCW, high resolution radar imaging system whose capability to generate SAR imagery has been demonstrated in the work of Jordan. The system, however, suffers from performance

limitations owing to a number of causes.

A broad classification of issues that have peaked the interest of the present author are those related to waveform synthesis. Only a heuristic approach was used for waveform synthesis, which resulted in a fixed and sub-optimal waveform configuration being used. This is a component of the system design and implementation that urgently needs addressing as the radar signal is the mainstay of successful operation of the system.

Considerations for frequency synthesis in FMCW SAR, can be categorized into two types: those related to the dynamic response characteristics of the synthesizer, and those related to the frequency response characteristics of the synthesizer.

Parameters related to the dynamic response include modulation period, modulation bandwidth, sweep rate, pulse repetition frequency (PRF) and ramp linearity. These are fundamental to the response of the radar system and dictate innumerable other system specifications such as resolution, signal-to-noise ratio (SNR) and maximum unambiguous range to name a few. Their role is well understood and documented in literature.

Associated with the frequency response of the synthesiser are such issues as phase noise and spurs which arise from instability in the synthesiser and result in the non-ideal output spectrum illustrated in Figure 1.1. There is considerably less discussion of these topics in the space of FMCW radar, let alone FMCW SAR, although there is a consensus that the phenomena can result in devastating performance degradation of range-Doppler systems.

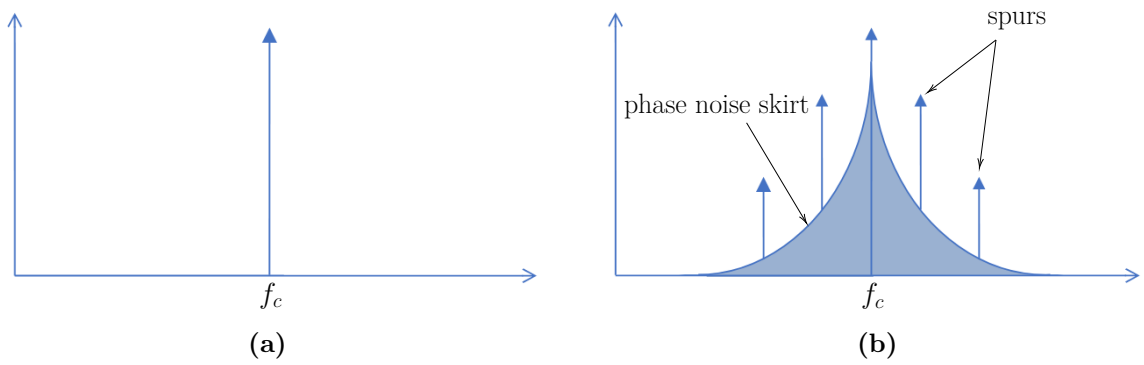


**Figure 1.1:** Illustration of (a) ideal and (b) real frequency tone output of synthesisers.

## 1.2 Problem Statement

The miloSAR has shown great promise as a compact UAV and light aircraft radar imaging system. Operation in its present state, however, is restricted by the waveform synthesis

approach and limited information on the synthesiser.

The following key problems have been identified:

1. Owing to a limited study and characterisation of the PLL synthesiser's dynamics, its maximum sweep rate constraints, its non-linear behaviour in response to large frequency excursions such as those required for sawtooth waveforms, and other such considerations are unknown.

   This significantly impacts the degree of design flexibility and results in indeterminate behaviour when parameters are changed. Consequently, a symmetric, triangular waveform with a fixed set of parameters has been used for each SAR mission.

   It is, particularly, important to implement sawtooth waveforms to achieve optimal performance because the processing architecture of the miloSAR does not support use of complete triangular waveforms and this results in half of the available data being discarded. This is inefficient as it wastes half the radiated energy.

2. The phase and frequency instability characteristics are also little understood.

   Jordan, successfully, investigated and mitigated the effects of spurious frequencies in the synthesised waveforms. However, the issue of phase noise is yet to be treated in depth and it is unknown what ramifications this has on the system performance.

   To aggravate the situation, there exists a complex relationship between the dynamic response characteristics and the frequency response characteristics of the PLL whereby improving behaviour in one domain deteriorates that in the other.

3. Signal acquisition rates beyond 11 MB/s cannot be achieved by the system which has necessitated measures such as reducing both the effective ramp period and the PRF. This results in a low processing gain and, consequently, a lower SNR than what is possible.

   Furthermore, the low PRF imposes an upper bound on the platform velocity that can be used without incurring the so-called Doppler aliasing. This problem is even more significant when the system is used in its fully-polarimetric mode which further divides the already low PRF by a factor of 2.

   Decimation is also employed to reduce the data rate which limits the maximum range that the system can image without violation of the Nyquist criterion. A decimation factor of 40 means that only 3.125 MHz of the available 3.8 MHz IF bandwidth could be sampled unambiguously resulting in a loss of range of the system.

Remedying these issues and contributing to the general pool of knowledge on FMCW SAR is the current author's main focus.

For this work, the following hypothesis is put forth:

*Accuracy of FMCW SAR systems can be eminently improved by improving the quality of the radar waveform and its manipulation.*

## 1.3 Research Objectives

Building on the identified challenges with the miloSAR and the proposed hypothesis, the following set of research objectives is derived:

1. **RO1:** To design aspects of, analyse and characterise the PLL synthesiser dynamics such that parameters such as maximum sweep rate and settling time may be extracted and used to drive implementation of more performant waveforms.
2. **RO2:** To investigate the role of waveform parameters on SAR image quality.
3. **RO3:** To assess the phase and frequency stability of the synthesised signal and approaches to optimise it.
4. **RO4:** To create software models of both the synthesiser and the SAR system for faster future design and optimisation without requiring time and resource-intensive experiments.
5. **RO5:** To make the required hardware, software, and firmware changes for improved performance including implementation of a high speed signal acquisition system to support data rates of up to 31 MB/s. By Equation 3.1, this specification allows for the sampling of the full 3.8 MHz IF bandwidth.

During the research, the author seeks to answer the following questions:

1. **RQ1:** How does the theory on FMCW radar design match up with practical systems? Can theoretically predicted parameters be relied on for system design?
2. **RQ2:** What is the relationship between dynamic response characteristics and frequency response characteristics of the synthesiser and how do these affect the generated waveforms?

3. **RQ3:** Phase noise is widely reported to be a major problem in radar systems. To what extent is it a concern in FMCW SAR and how much should it drive the design process?

4. **RQ4:** What are the performance limitations of a time-offset heterodyne architecture as it relates to waveform synthesis?

## 1.4 Scope and Limitations

Due to a finite time frame for completion of the current research, or in the interest of keeping this work concise, the current study will not include the following:

- **Custom PLL hardware implementation:** The miloSAR uses a pre-made PLL evaluation board, the LMX2492EVM [3]. This does reduce the amount of control the engineer has on the waveform synthesis and a better solution would be to implement one's own synthesiser board. However, for the purposes of this work, the evaluation board is sufficient to perform the desired analysis and prescribe future recommendations.

- **In depth consideration of SAR processing algorithms and compensations:** Artifacts of SAR data collection distort or degrade quality of the image. These include range migration, non-ideal motion and electromagnetic interference (EMI). However, these will not be compensated for in the obtained results.

Additionally, the research is limited by the following:

- **Cost of acquiring SAR data:** Collecting SAR data using the miloSAR is, at this point in time, a very resource intensive exercise. It requires a fixed wing aircraft or a licensed UAV system both of which are expensive to procure. Therefore, there is a significant limitation to the collection of SAR data and the author uses other techniques to make the most of the available data in analysis.

## 1.5 Plan of Development

A profile of the current document is as follows:

**Chapter 1** has introduced the context of the study. The research objectives and questions have been identified, and the value of such research argued. The limitations of the study have also been discussed.

**Chapter 2** reviews existing literature. It explores and critiques the ideas brought up by other researchers on some of the topics pertinent to successful waveform synthesis including performance limitations of FMCW systems, FMCW architectures, frequency synthesis approaches and other FMCW SAR systems.

**Chapter 3** gives the details of implementation of miloSAR. Redundant repetition of content brought up in the works of Tchekashkin and Jordan is avoided and instead, the author focuses on new contributions such as the high speed acquisition system and noteworthy insights missing in the aforementioned works. A brief account of SAR data processing is also given and standard image quality metrics which will be used to evaluate system performance are introduced.

**Chapter 4** focuses on the modelling, design, implementation and characterisation of the fractional-N PLL and its waveforms for accurate FMCW operation. It includes an overview of the PLL architecture in the context of the LMX2492EVM hardware used and a model of the synthesiser system which defines several critical parameters and characteristics. The dynamic response and frequency response of the PLL are assessed and finally, waveform design considerations are reviewed.

**Chapter 5** concerns the role of phase and frequency stability in FMCW SAR and presents theoretical ideas supported with simulation results. It is divided into three primary sections, the first pertaining to ramp non-linearity, the second to spurs and the third to phase noise. As will be shown, ramp non-linearity is not a major concern for the designed PLL setup and the effects of spurs were investigated in great detail in the work of Jordan. The chapter therefore, places more emphasis on analysing the effects of phase noise.

**Chapter 6** presents the results of integration of all aspects considered in prior chapters.

The maximum sweep rate constraint and the pull-in time constraint — the synthesiser's settling time after a large change in frequency — are measured and compared to theoretical predictions. A strong agreement is observed between the measurements and predictions.

Using these parameters and by increasing the PLL bandwidth, a sawtooth waveform configuration was implemented such that a higher modulation period was realised. It is shown that this results in improved frequency resolution, from 0.5 m per range bin with the original $T_r = 6.125 \times 10^{-6} s$ to 0.3 m per range bin with the maximum achievable

$T_r = 6.843 \times 10^{-4}$. Furthermore, SNR is seen to improve by 8.669 dB due to an increased range processing gain.

A related parameter is modulation bandwidth, $B_r$, and it is shown that increasing the bandwidth results in better range resolution, with an improvement of 1.8464 m for a 75 MHz increase.

The TCP/IP signal recording module allowed for unlimited recording time not limited by the 20 GB limit of the MMC on board the STEMlab. Additionally, and more importantly, this allowed for the system to be used with a lower decimation factor such that the IF sampling rate was improved from 3.125 MHz to 3.8 MHz which increased maximum range by 50 m for a sweep rate, $k_r$, of $1.739 \times 10^{12}$ Hz/s.

A combination of better throughput and using higher sweep rates — also enabled by an increase in PLL bandwidth — allowed for higher PRFs, up to 10 000 Hz, to be used. The relationship that scaling the PRF by a factor of $N$ results in an SNR improvement by $10\log(N)$ dB is shown to manifest in the case of a real static radar. It is also demonstrated that if the PRF is below a rate of the Doppler bandwidth, Doppler aliasing is seen to occur; hence, support for high PRFs allows for the system to be deployed on very fast aircraft.

The chapter then shifts attention towards assessing the phase and frequency stability of the system. The PLL is seen to have -66.5 dBc/Hz in-band phase noise and approximately -115 dB/Hz out-band phase noise. As a result of both the transmit and receive PLLs as well as the ADC being synchronised to the same clock, the noise processes are correlated inside the PLL passband which results in a reduction of the phase noise. The digitised signal has around -90 dBc/Hz phase noise in-band while the out-band phase noise remains the same. The phase noise is seen to raise the noise floor or sidelobe levels (depending on the context) but it is shown that for signal to clutter ratios SCR below 50 dB, phase noise due to targets within the scene may not be too much of a concern as their phase noise skirts fall below the clutter. However, phase noise due to the leakage signal is still a primary issue because the leakage signal is very strong and it is shown to degrade image contrast and prevent other targets from being detected. This is especially a problem for wide PLL bandwidths which allow more in-band phase noise to pass through unfiltered. Techniques to mitigate this problem are then reviewed including changing the reference oscillator, the PLL bandwidth and architecture modifications.

Finally, **Chapter 7** summarises the findings of the work. The hypothesis is found to be true, as all aspects of the waveform are seen to manifest in the SAR system impulse response or, directly, in the SAR image.

Recommendations are also made for future design iterations which include implementation of a hybrid PLL-DDS synthesiser, a frequency offset heterodyne architecture, and parameter optimisation algorithms, among others.

# Chapter 2

# Literature Review

Successful implementation of an FMCW SAR system relies on the aggregation of ideas under different themes to build up subsystems that cohesively work together.

As will be shown in this chapter, there are various design decisions to be made, and different authors have discussed the different aspects of these design choices. The objective of this chapter is to review the research that has been led on implementing FMCW SAR systems with a focus on the waveform synthesis component.

The concept of FMCW is first, briefly, reviewed to give context to the discussion within this chapter and to the rest of the work.

Subsequently, problems afflicting FMCW radar systems are identified and the main issues, which are leakage and distortion in modulation, are discussed in greater detail.

Following this, architectures of FMCW radar systems are explored. With the help of literature references, the design rationale behind miloSAR's architecture is also highlighted.

Options available for frequency synthesis are then reviewed and the mainstream approaches, namely phase-locked loop (PLL) synthesisers, direct digital synthesisers (DDS) and hybrid synthesisers are considered.

Finally, the chapter explores existing work that has been done in the space of FMCW SAR with the objective of identifying some interesting approaches other engineers used to tackle specific problems.

## 2.1 FMCW Radar Concept

Due to their recent and widespread usage in industry, FMCW radars are often referred to as the 'radars of the future' [4].

Instead of relying on short pulse transmissions, long, continuous wave (CW) transmissions are used, allowing for the same amount of energy to be transmitted at a lower peak power. Intrapulse frequency modulation (FM) is also applied to address the conflicting relationship between range resolution and transmit energy by making the resolution dependent on the modulation bandwidth. The result is a low power, high resolution radar concept offering attractive benefits such as low detectability, cost, and form factor among others.

Resolving the targets illuminated by the radar, in range, is done by matched filtering or, more commonly, stretch processing their signal reflections. The latter entails demodulating the received RF signal with a copy of the transmit signal, also known as 'dechirping', such that the mixer output is a monochromatic sinusoid whose frequency is directly proportional to target range. The spectral content of the dechirped signal is viewed via the Discrete Fourier Transform (DFT), which is more efficiently computed through the Fast Fourier Transform (FFT), such that the targets at a particular range appear as a distinct peak in a frequency bin corresponding to that range. This process is illustrated in Figure 2.1 and an analytical development has been performed in Appendix A.

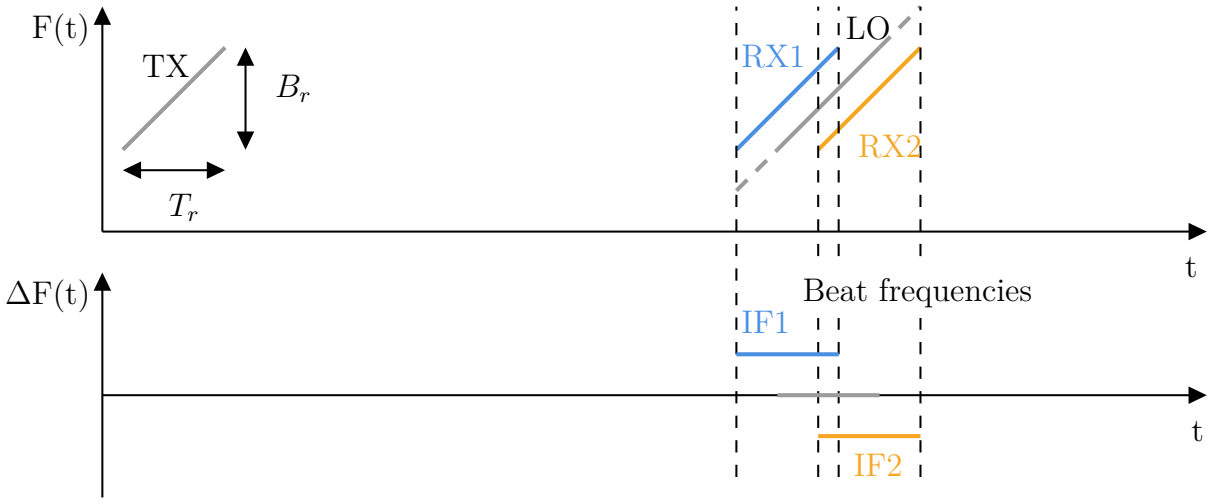


**Figure 2.1:** Illustration of stretch processing. $B_r$ is the FMCW waveform modulation bandwidth and $T_r$ is its modulation period.

Stretch processing has the advantage of reducing the bandwidth of the sampled signal which reduces the sampling rate requirements for the ADC further reducing implementation cost and size.

## 2.2 Performance Limitations of FMCW Radar

Decoupling the range resolution from transmit energy is a compelling case for FMCW systems over the traditional pulsed systems which do not use pulse compression waveforms.

However, various issues that degrade range and Doppler estimation accuracy have been identified in literature including leakage [5], [6], ramp non-linearity [7], [8], susceptibility to EMI due to the low transmit power [9], internal delay within the radar system [5] and several others.

In this section, the most problematic issues of leakage and ramp non-linearity are reviewed.

### 2.2.1 Leakage

Leakage is a prevalent problem reported in FMCW radar literature and a primary concern in this work. Various types have been recognised such as antenna leakage, internal leakage and short range leakage.

For FMCW radar applications, achieving sufficient transmitter-receiver isolation is a critical and challenging issue, but it can be addressed by leveraging the experience gained from previous FMCW radar implementations [10].

Antenna leakage has been brought up in [10], [11] and several other sources. It arises from the concurrent operation of the transmitter and receiver and the non-ideal isolation in the circulator, for the monostatic case, and between the transmit and receive antennas, for the quasi-monostatic and bistatic cases.

Non-ideal isolation of internal components results in what is referred to as internal leakage which entails, part of the transmitted signal coupling directly from the transmit circuitry into the receive chain and being mixed down like other target returns.

Short range (SR) leakage has been brought up in literature such as that by Melzer et al. [12] and is due to fixed, undesirable objects near the transmit antenna(s). In the case of Melzer's work, this was the car bumper on which an automotive radar was mounted.

A combination of these and other such means by which the transmit signal leaks into the receive chain causes two major problems. The first is that antenna and SR leakages, are very high power and can saturate and damage receive chain components especially when

a power amplifier (PA) is used to amplify the received target echoes. Secondly, due to oscillator instability, the leakage signal contains a phase noise skirt which extends through the entire IF spectrum, raising the noise floor of the system and degrading dynamic range [5].

Several investigations into how to resolve the leakage problem have been carried out. A common technique, discussed in greater detail in Section 2.3 is implementing a heterodyne architecture with analogue filters designed to filter out the peak of the leakage response in the IF spectrum. This however, does not eliminate the leakage phase noise as do the rest of the techniques discussed in the present section.

Beasly et al. [6] built on the work of O'Hara and Moore [13] to propose what has come to be a standard cancellation scheme known as the Reflected Power Canceller (RPC). It involves a closed-loop leakage canceller that adaptively generates an error vector equal in amplitude and anti-phase to the leakage signal in order to cancel out the leakage. In the work of Beasly, this achieved a remarkable cancellation of over 35 dB. In all of its implementations encountered, however, it is applied for the monostatic architecture. It would be interesting to see how the approach may be modified to work for quasi-monostatic systems.

Lin et al. [14] implemented a Digital Signal Processing DSP version of the RPC and achieved 30 dB cancellation over a 1.7 GHz modulation bandwidth; but similarly, this was demonstrated for a monostatic system.

Melzer et al. [12] designed what appears to be the perfect solution for a quasi-monostatic architecture such as the miloSAR. His cancellation scheme introduces an artificial target, using a delay line, which is tuned to have the same amplitude and delay as the leakage. This is then passed through the same receive sequence as the reflected signals and is subtracted from the measured signal as shown in Figure 2.2.

The work reports 6.4 dB of leakage suppression and would be able to achieve even more if more delay lines could be added. The main criticism of this approach, however, is that for a system where two input channels are required, 4 ADCs would be needed which increases the cost and complexity of the system.

Software techniques have also been put forth, such as the Stationary Point Concentration (SPC) technique by Park [5] which improves the noise floor by up to 7 dB.

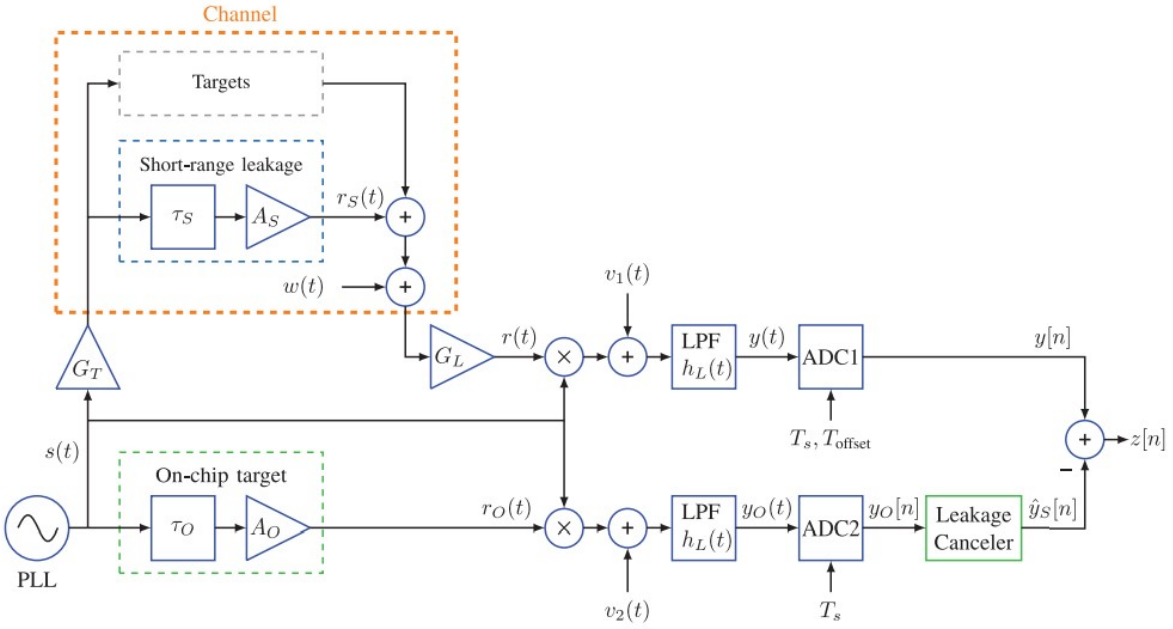


**Figure 2.2:** Leakage cancellation scheme based on artificial target.
Leakage cancellation scheme based on artificial target [12].

### 2.2.2 Ramp Non-linearity

Deviations of the transmit and local oscillator (LO) signals from the ideal linear ramps, unsurprisingly, result in measurement inaccuracy on account of estimated target range and velocity being represented by the frequency difference between the two signals.

These non-linearities can have all manner of causes but all result in phase and frequency errors in the IF signal such that target energy is dispersed across various frequency bins in the IF spectrum.

In systems which directly use an open loop voltage controlled oscillator (VCO) to produce the FMCW waveforms such as in [15], [16], modulation distortions stem from the non-linear characteristic curve of the VCO. This is a big problem as has been reported by the authors of the cited literature.

VCOs are typically enclosed in closed-loop feedback systems such as PLLs to linearise the input-output relationship. However, PLLs, may have digital effects that result in quantised or curved output ramps, cycle-slips when the PLL unlocks, or other forms of distortion as discussed in [17], [18].

To address these errors, several non-linearity correction approaches, both hardware-based and software-based, have been proposed in literature.

Traditional compensation approaches use the Principle of Derivative Algorithm discussed in [7], [8] which uses a delay line to approximate the phase error due to ramp non-linearity. The phase error in the IF signal is approximated as the scaled derivative of the transmit phase error as

$$\Delta\phi_e(t, \tau_{ref}) = \phi_e(t) - \phi_e(t - \tau_{ref}) \approx \tau_{ref}\phi'_e(t) \tag{2.1}$$

where $t$ is the fast-time variable, $\tau_{ref}$ is the delay of the local oscillator signal relative to the received signal through the delay line, and $\phi_e$ is the phase error of the synthesised ramp (assuming the transmit and local oscillator ramps have identical phase errors).

The phase error is, therefore, estimated by

$$\phi_e(t) \approx \int_0^{\text{PRI}} (\Delta\phi_e(t, \tau_{ref})/\tau_{ref})\, dt \tag{2.2}$$

and can be compensated for in the IF spectrum.

This approach only works, however, under the assumption that $\tau_{ref}$ is far smaller that the PRI and becomes more inaccurate the larger $\tau_{ref}$ is. Nonetheless, it is a very efficient technique which is simple to implement.

Homomorphic deconvolution, proposed by Bogert et al. [19], is an alternative approach to estimating the phase error and is also applied in [8]. It entails regarding $\Delta\phi_e(t, \tau_{ref})$ as the convolution of $\phi_e(t)$ and a $\delta$ function series, the details of which are unnecessary to include in this literature review.

A comparative study of the former and latter algorithms was performed in [8] and it was proven that for $\tau_{ref} = 0.2\ \mu$s, the accuracy in non-linearity estimation was about the same for both and they deviated for larger $\tau_{ref}$ with homomorphic deconvolution performing better.

## 2.3 System Architectures

Resolving the challenges that have been identified, especially, the leakage problem, is the primary objective influencing FMCW system architectures. In addition to this are other minor factors such as cost, size etc.

The three main architectures used in RF receivers are the homodyne, heterodyne and superheterodyne architectures.

### 2.3.1 Homodyne Architecture

In a homodyne receiver, also known as a direct-conversion receiver (DCR), the incoming RF signal is demodulated by a local oscillator (LO) signal whose instantaneous frequency is identical or very close to that of the RF signal. The signal is, therefore, converted to baseband with one mixer stage as shown in Figure 2.3.

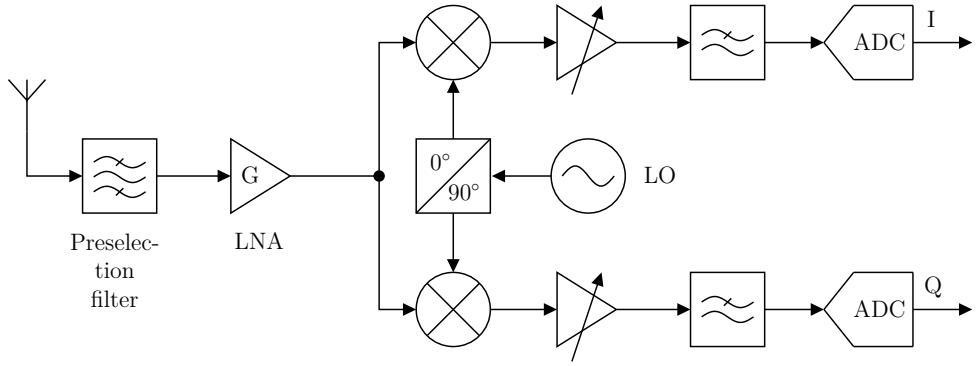


**Figure 2.3:** Homodyne receiver architecture [20]. LNA stand for low noise amplifier, I denotes in-phase samples and Q denotes quadrature samples.

### 2.3.2 Heterodyne Architecture

The heterodyne architecture requires an additional mixer to convert the modulated RF signal into a modulated intermediate frequency (IF) signal, which is then passed into a second mixer stage that transforms it into a baseband (zero-IF) signal as shown in Figure 2.4. The IF signal may also be digitally down-converted.

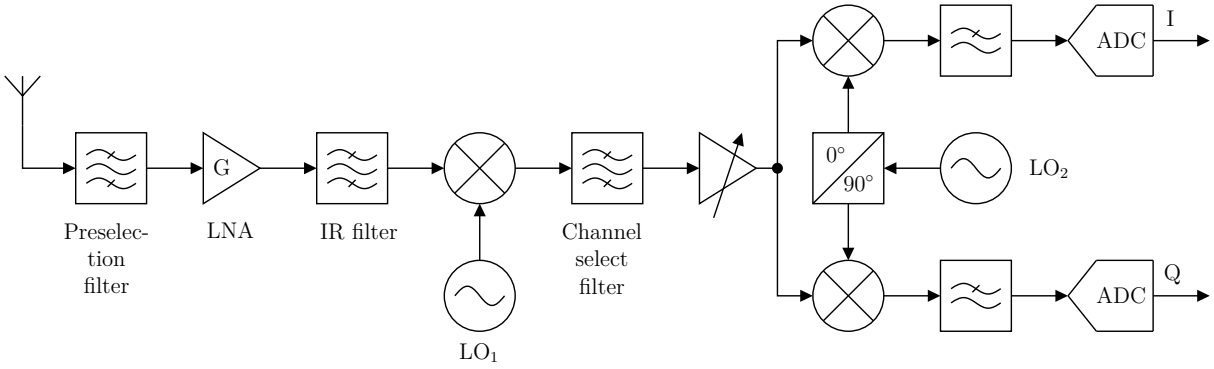


**Figure 2.4:** Heterodyne receiver architecture [20].

A constant frequency difference is required between the transmit and local oscillator signals such that, the filtered IF signal is at a frequency given by this frequency difference.

To achieve this, either a frequency offset is applied directly to one of the signals or a time offset is introduced between the signals such that the instantaneous frequencies have a constant frequency difference between them.

Frequency offset heterodyne architectures are the norm and apply for most, if not all, modulation types. Their application in FMCW systems has been reported in [21] and many other resources. A major drawback is that a second signal source would always be required to upconvert the other signal which results in an increase in phase noise and negation of range correlation filtering [22] used to reduce it.

Time offset heterodyne architectures are less common and apply only for linear frequency modulated (LFM) signals. An example of this, by Kim et. al [23], is shown in Figure 2.5.

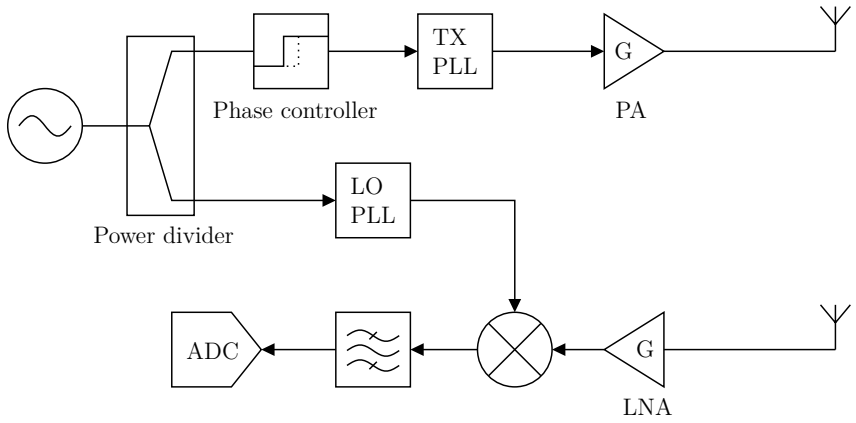


**Figure 2.5:** Time offset dual-PLL FMCW architecture [23]. PA stands for power amplifier.

## 2.4 Frequency Synthesis

Frequency synthesis is a key facet of the transceiver, predominantly accomplished through use of phase-locked loop (PLL) synthesisers, direct digital synthesisers (DDS) or hybrid combinations of the two.

### 2.4.1 Phase-Locked Loop Synthesiser

PLLs, as has been noted previously, enclose the VCO in a negative feedback loop such that the phase and frequency of its output tracks that of an input reference clock. A simplified, typical PLL architecture is as shown in Figure 2.6.

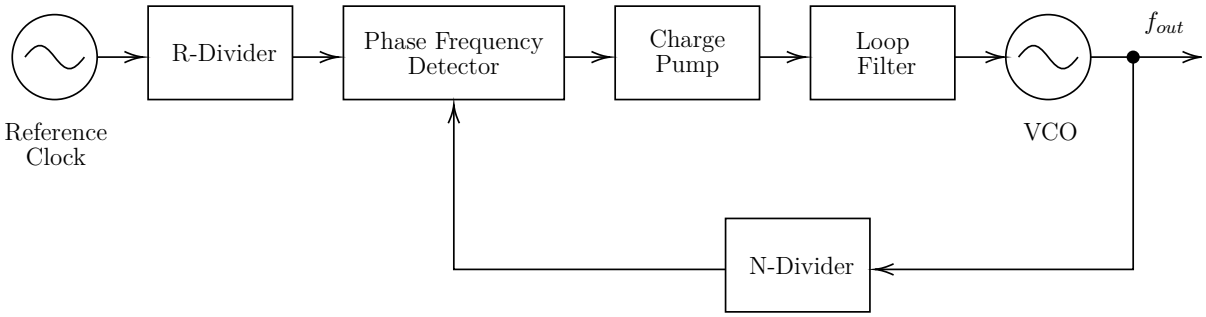


**Figure 2.6:** Simplified PLL architecture.

The VCO output is given by

$$f_{out} = \frac{f_{\text{OSC}}}{N} \tag{2.3}$$

where $N$ is a scaling factor of the frequency scaler (N-divider) in the feedback path of the loop.

Traditionally, analogue PLLs were used; today there are three PLL designs: analogue, digital (hybrid) and all-digital. Ye [24] discusses an implementation of an all-digital PLL based on the FPGA.

The main selling points for PLLs are high output linearity; ability to achieve high output frequencies as well as the filtering characteristic of the closed-loop transfer function which results in low spurs and phase noise in the stopband of the filter.

### 2.4.2 Direct Digital Synthesis

Direct Digital Synthesis (DDS) is a technique for creating an analogue waveform by first generating a time-varying signal in digital form and then converting it to an analogue signal. Since the operations in a DDS device are mainly digital, it can provide fast frequency switching, precise frequency resolution, and a wide range of operational frequencies.

Figure 2.7 shows a typical DDS architecture.

The frequency register's binary number is the primary input for the phase accumulator. The phase accumulator determines a phase address for a look-up table which then outputs an amplitude value for the corresponding function of the phase value e.g. sine of the phase angle, in the case of a sine look-up table. The discrete amplitude signal is then converted to an analogue voltage or current by the DAC. In order to produce a fixed-frequency sine wave, the phase accumulator adds a constant value, known as the phase increment, to its value during each clock cycle. A high phase increment value results in the phase

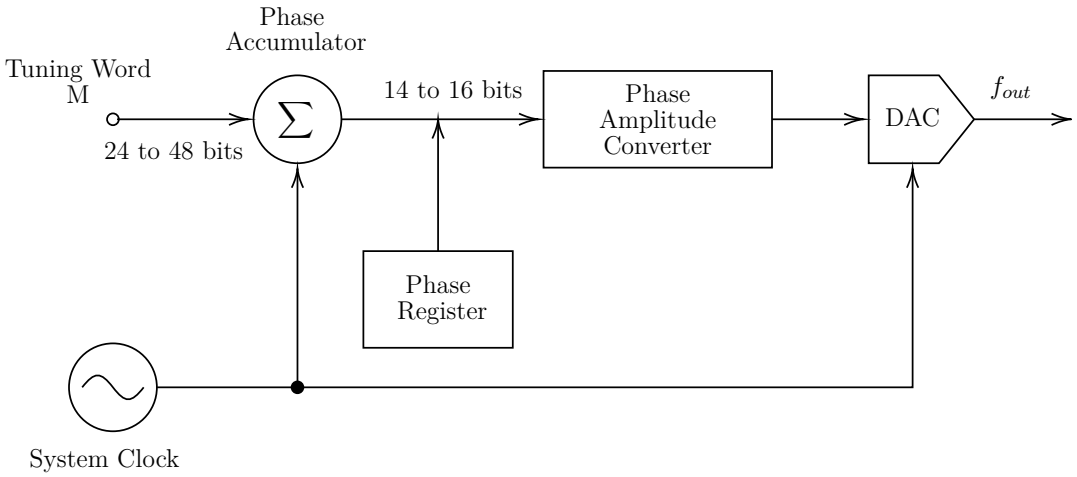


**Figure 2.7:** Simplified DDS architecture

accumulator quickly cycling through the sine look-up table, producing a high-frequency sine wave. Conversely, a small phase increment value causes the phase accumulator to take more steps, generating a slower waveform.

A DDS has the advantages of higher frequency agility and better phase noise performance than a PLL. However, it may have higher spurious responses due to truncation effects.

### 2.4.3 Hybrid Synthesisers

Hybrid synthesisers, which combine the PLL and the DDS to obtain the aforementioned benefits of both, have also been proposed in literature.

One such system is that by Du [25] et al. shown in Figure 2.8.

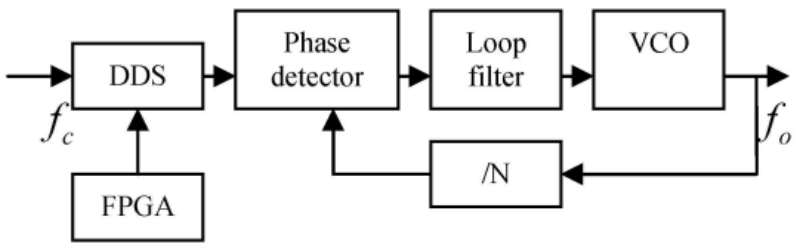


**Figure 2.8:** Hybrid DDS-PLL system [25].

In this case, the DDS is used to generate the reference input for the PLL which results in a combination of the frequency agility and phase noise performance strengths of the DDS being combined with the filtering characteristic and ability to generate high frequencies

of the PLL. Du's synthesiser is implemented on custom PCB which makes for a compact system.

## 2.5 State of the Art in FMCW SAR

Thus far, the elementary components of an FMCW SAR system have been considered in isolation.

It is of interest to explore how these and other additional elements are combined to form functional FMCW SAR systems.

### 2.5.1 microASAR

Brigham Young University (BYU) and Artemis Inc. collaborated on a small, low-cost, FMCW SAR system named the microASAR [26] which, like the miloSAR, is deployed on UAVs and other small aircraft.

The microASAR is a C-band system employing the dechirp-on-receive technique. Its architecture is as shown in Figure 2.9.

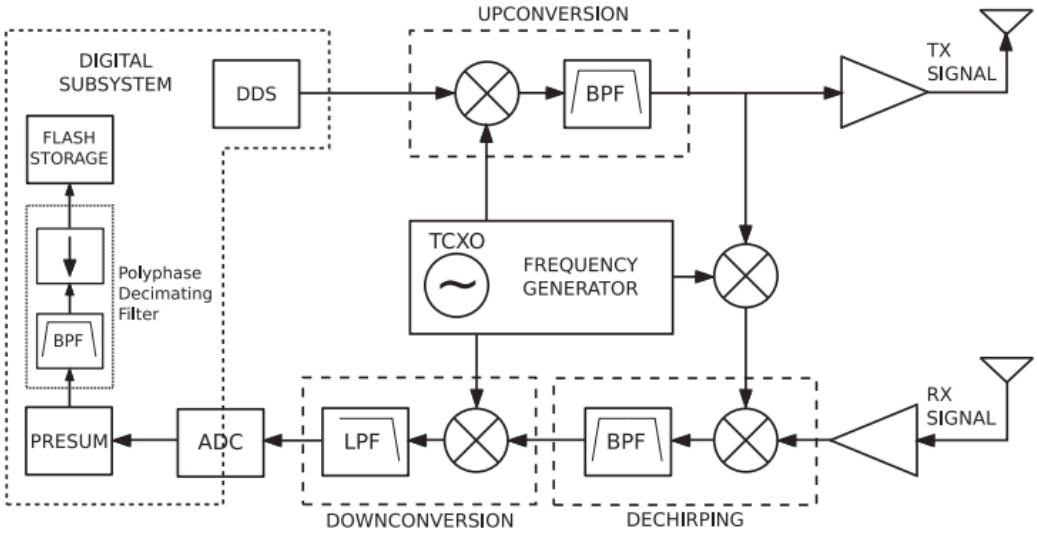


**Figure 2.9:** microASAR architecture [26].

It uses the DDS to generate mono-directional frequency ramps so as to 'more easily achieve high PRFs' unlike the microSAR [27] from which it was derived, which used a triangular waveform. The DDS requires some cycles between transmitted chirps in order

to reset; therefore, the system is not CW in a strict sense, which will be shown to be the case with the miloSAR. It achieves a variable signal bandwidth in the range of 80-200 MHz and variable PRFs in the ranges of 7 — 14 kHz.

It is noteworthy that the PRF weighs heavily in the design considerations. Data rates are also a concern, with the system only achieving 5 MB/s and having to use presumming in order to reduce the amount of data for a given PRF.

In order to maximise transmit and receive isolation the system is 'bistatic'[1] It uses a $2 \times 8$ patch array with a beamwidth of $8.5° \times 50°$.

### 2.5.2 SlimSAR

The SlimSAR [28] developed by Artemis is also a striking FMCW SAR system which was actually based on the microASAR [26] and the Naval Research Laboratory UAS SAR (NuSAR).

What stands out about the SlimSAR is that it is a multi-frequency system capable of operating in the L-band and X-band. This allows for enhancement of the SAR imagery by combining the returns from different frequencies, over which the targets in the scene may very different characteristics [29].

The system uses a pair of DDSs for the transmit and local oscillator signals where one is delayed in time to achieve a configurable IF much like the miloSAR.

### 2.5.3 Mini-SAR

The Mini-SAR [30] is a 2.4 kg, Ku-band system developed by the College of Electronic Science and Engineering (CESE) of the National University of Defense Technology (NUDT) in China.

The Ku-band is susceptible to higher atmospheric and precipitation losses. Higher bands, however, offer several distinct benefits such as improved visibility of man-made objects in SAR images, relaxation of motion compensation requirements for a given cross-range resolution, and the possibility of component miniaturization due to its high frequencies.

It also uses the microstrip patch antenna which is proving to be a favourite in FMCW

[1] In the current work, a radar with separate transmit and receive antennas which are still in close proximity to each other, such that they appear as collocated to point targets, is referred to as quasi-monostatic.

SAR, likely, because of being lightweight and having a small form factor. This, however, makes achieving multi-polarimetric imaging and good transmit–receive isolation very challenging endeavours.

For waveform synthesis, the system uses a hybrid DDS-PLL synthesiser having a transmit bandwidth of 900 MHz.

What is particularly impressive about the Mini-SAR is it's mass storage and real-time imaging capabilities with supported data rates of over 169 MB/s. It is one of the best performant systems in this regard among non-commercial systems encountered. The architecture of the signal acquisition system is as shown in Figure 2.10

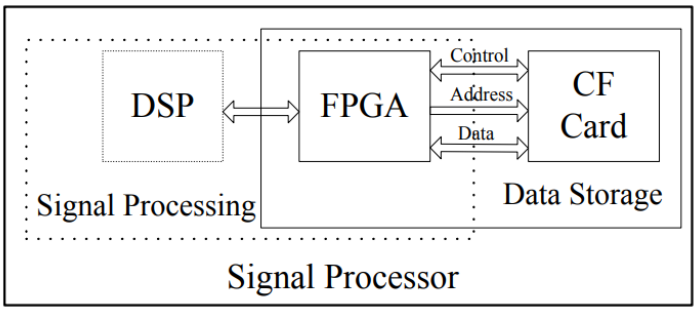


**Figure 2.10:** Signal acquisition system for the Mini-SAR [30].

It directly offloads data from the XC6VLX75T FPGA to a 128 GB compact flash CF storage card which is hosted by the FPGA. This eliminates the need for slow CPU intervention in the storage process which was the more commonly observed approach. Parameters for the FPGA are programmed using USB. Additionally, the system uses a buffer scheme using the DDR3 SDRAM to deal with the unpredictable response time due to implicit operations in the flash translation layer (FTL). The CPU in the miloSAR would handle this buffering.

# Chapter 3

# Overview of the miloSAR

The miloSAR, and its challenges have been briefly introduced in Chapter 1. Presently, a more detailed overview of the system is given.

The chapter first walks through the hardware and firmware elements of the system in the order in which the radar signal propagates through it, focusing primarily on the new contributions and insights made by the present author.

Characterisation of the receiver thermal noise is then performed, which is an essential exercise because the phase noise assessed in this work will add to the already-existing noise floor.

A model of the miloSAR is then developed for use throughout this work and for faster future designs. This also satisfies RO4.

Following this, SAR data processing for the miloSAR is explored and the prevalent SAR image quality (IQ) metrics, used to quantify the success of a particular implementation of the system's waveforms, are reviewed.

## 3.1 System Hardware and Firmware

Driving the design of the miloSAR was the fundamental desire to circumvent persistent leakage. To face this problem, a heterodyne architecture was used to place the IF spectrum at a configurable IF center frequency within the passband of a 9.5 MHz — 11.5 MHz BPF such that the strong leakage peak is filtered out.

Figure 3.1 shows the architecture of the dual-PLL time-offset heterodyne system while

Figure 3.2 shows the assembled system hardware.

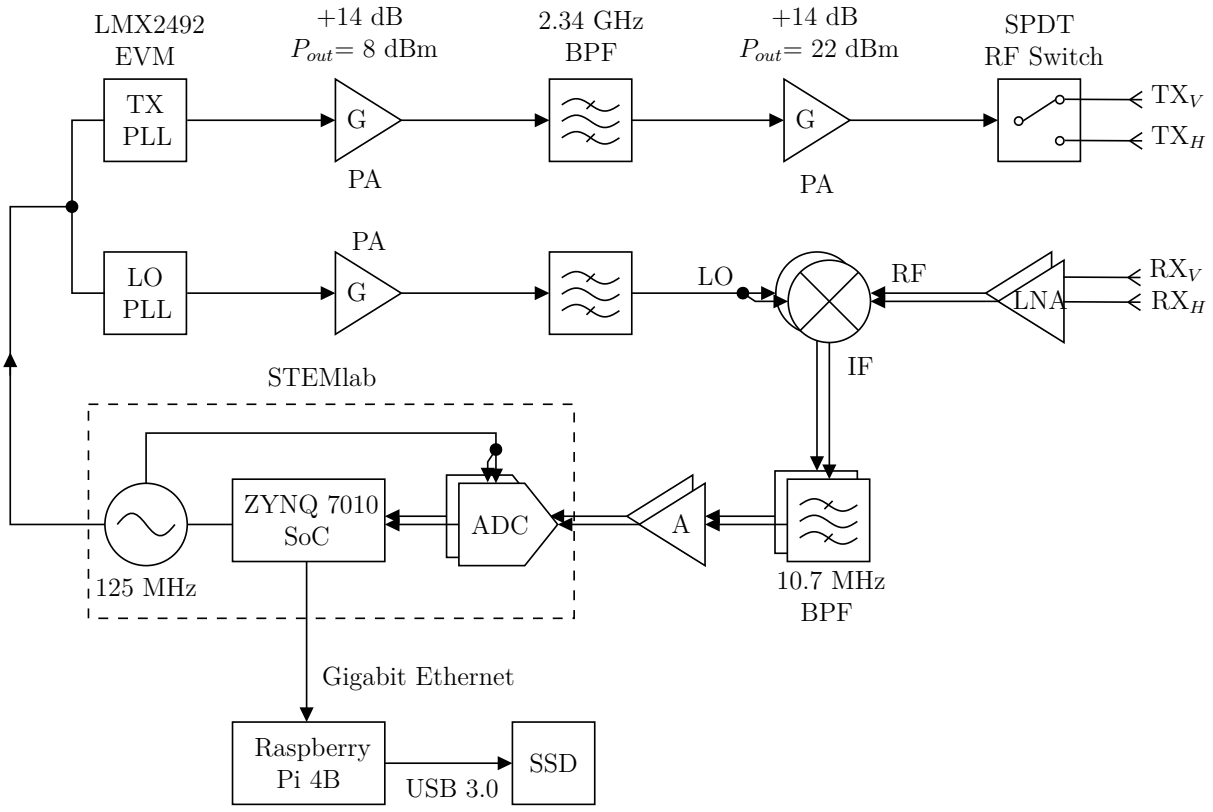


**Figure 3.1:** Architecture of the miloSAR.

The basic operational principle of the system is that, two FMCW waveforms, with the same parameters except for a delay in the start time of one, are synthesised using two independent PLL synthesisers. One signal is radiated by the transmit antenna and the target reflections of this signal are measured by the receive antenna. The echoes at the receive antenna are then mixed with the second FMCW waveform to create a beat signal which is sampled by the ADC and processed to represent the scatterers in the imaged scene.

The most notable characteristic of this architecture is the use of the two PLL synthesisers to achieve a configurable IF, which departs from traditional heterodyne architectures, as discussed in Section 2.1.

It is of interest to determine the performance of this approach in terms of phase stability, as the use of two PLLs results in uncorrelated or partially correlated phase noise which does not cancel out as it would if it were correlated [22].

Table 3.1 summarises the parameters of the fixed waveform used in the miloSAR prior to the involvement of the present author. This serves as a benchmark waveform against

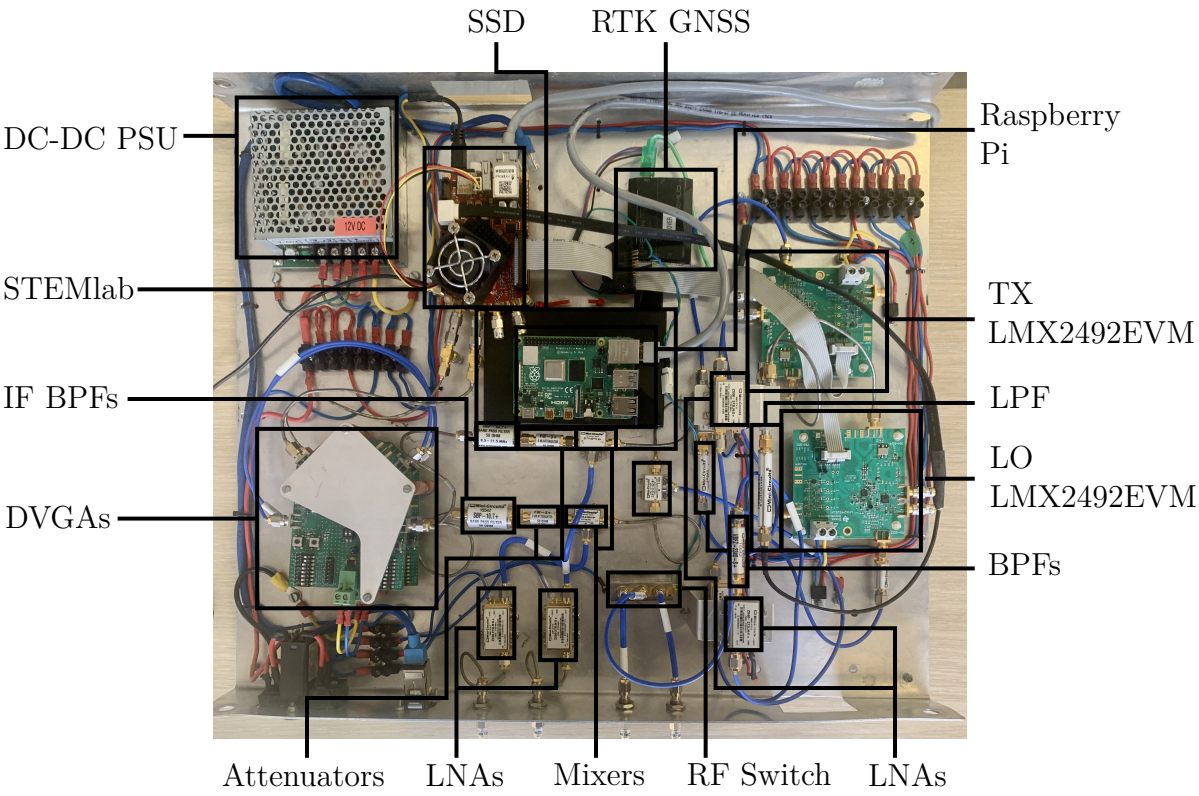


**Figure 3.2:** miloSAR Hardware.

which other waveform configurations will be compared.

**Table 3.1:** PLL and the fixed waveform parameters used in miloSAR prior to work undertaken by author.

| **Parameter** | **Symbol** | **Value** |
|---|---|---|
| Charge pump gain (CPG) | | 0.2 mA |
| Modulation bandwidth | $B_r$ | 175 MHz |
| Modulation period | $T_r$ | $4.026 \times 10^{-4}$ s |
| Sweep rate | $k_r$ | $1.739 \times 10^{12}$ Hz/s |
| Pulse repetition frequency (PRF) | | 1250 Hz |

Table 3.2 identifies parameters which require improvement. These parameters are limited by a variety of factors including the waveform configuration and the system implementation and are discussed in greater detail in the forthcoming sections.

The maximum PRF is computed as the sum of the periods of the up-ramp and down-ramp divided by the pre-summing factor (PF) which was 2 to ensure data rates did not exceed 11 MB/s.

**Table 3.2:** Parameters identified for improvement.

| Parameter | Symbol | Value |
|---|---|---|
| Maximum IF bandwidth | $B_{\text{IF}}$ | 3.125 MHz |
| Maximum data rate (DR) | | 11 MB/s |
| Minimum up-ramp (usable) period | $T_{r_{max}}$ | $36.032 \times 10^{-6}$ s |
| Minimum down-ramp (discarded) period | | $246.518 \times 10^{-6}$ s |
| Maximum PRF | | 1770 Hz |

### 3.1.1 Transmit Module

For the generation and transmission of the RF signal a transmit chain consisting of the transmit LMX2492EVM [3] fractional-N PLL synthesiser, a VBFZ-2340 [31] 2020 - 2660 GHz band-pass filter (BPF), two ZX60-272LN-S+ [32] low noise amplifiers (LNAs), and a single-pole double throw RF switch is used.

The synthesised FMCW waveform has a maximum bandwidth of 175 MHz about the nominal carrier frequency of 2.4375 GHz and is derived from a 125 MHz differential square wave supplied as a reference clock to the PLLs from the TXC Corporation CXO BFBC90 crystal oscillator onboard the STEMlab.

The transmit PLL output is amplified by a series cascade of the aforementioned LNAs, separated by the BPF. Each LNA provides a typical output power of 18.5 dBm at the 1 dB compression point (1 dB-CP). The measured output of the first LNA is 8 dBm which drives the output of the second LNA to 22 dBm such that it is not quite operating at the 1 dB-CP. This is likely to cause distortion of the transmitted waveform and should be investigated in future iterations of the system.

An RF switch is then used at the output of the amplification scheme to perform a demultiplexing operation such that the signal is directed to either of the two transmit antenna input ports resulting in varying — horizontal or vertical — polarisation. Consequently, three transmit modes can be realised, horizontal polarisation, vertical polarisation and interleaved polarisation.

### 3.1.2 Antennas

Antennas are a major concern in this work because of Doppler bandwidth specifications and leakage which will be revealed to be core considerations in the waveform design.

The system uses a quasi-monostatic antenna made up of two, cylindrical antennas with

a separation of 30 cm but perceived to have a phase center at the same range.

Each antenna has a diameter of 10 cm which, at a carrier of 2.4375 GHz, results in an azimuth beamwidth of approximately 70.517°. The significance of this, as it pertains to the Doppler bandwidth, is discussed in Section 4.5.2.

### 3.1.3 Receive Module

In this work, elements within the receive chain — from the input port of the receive antenna to just before digitisation by the analogue-to-digital converters (ADCs) — are, collectively, referred to as receive module. Two channels, one for each receive polarisation, are used.

The function of this module is to demodulate or 'dechirp' the received FMCW waveforms by mixing them with a local oscillator, the details of which have been discussed in Section 2.1. The dechirped signals are then band-pass filtered by the SBP-10.7+ [33] 9.5 MHz — 11.5 MHz BPF which attenuates undesired spectral components, especially around the IF bandwidth. With the correct system configuration, the leakage signals can be placed in the stopband of the filter, thus achieving the desired suppression of the strong return to prevent it from saturating and damaging subsequent components in the receive chain.

The analogue, dechirped signals are then amplified by a pair of Digital Variable Gain Amplifiers (DVGAs) before being sampled by the ADCs.

### 3.1.4 Signal Acquisition Module

Following the analogue dechirp procedure carried out by the receive module, each dechirped signal is digitised and pre-processed by the signal acquisition module.

In the miloSAR, this comprises of the ADC, the STEMlab gateware and software and the Raspberry Pi which offloads data to a storage device such as the solid state drive (SSD) as shown in Figure 3.3.

#### Analogue-to-Digital Converter

Onboard the STEMlab is the LTC2145CUP-14 [34] ADC which is a two-channel, 14-bit ADC with a bandwidth of DC — 60MHz and sampling at rate of 125 Msps.

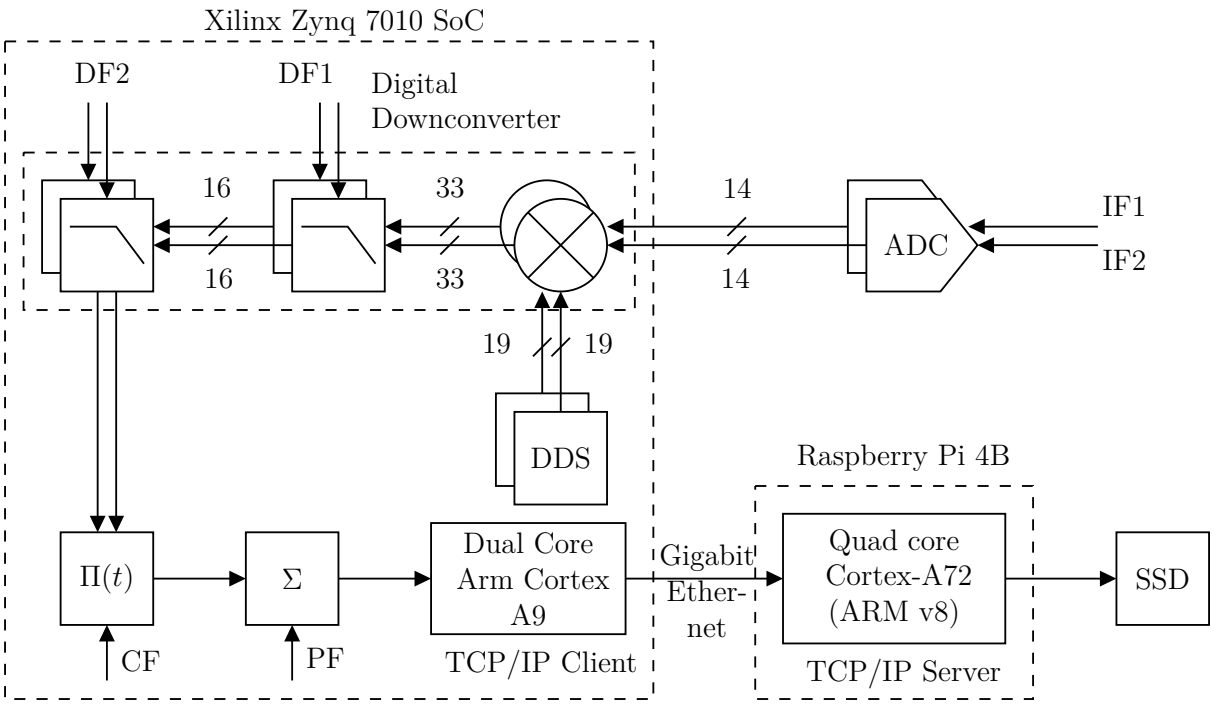


**Figure 3.3:** Signal acquisition module architecture. DF is the decimation factor, CF is the chopping factor (i.e. duty cycle), and PF is the pre-summing factor (i.e. number of pulses coherently summed to reduce the PRF).

It has an SNR of 73.1 dB which is a significant parameter and 55 dB of input isolation at 1 MHz and 10 MHz.

### Gateware

Each ADC channel's 14 bit output is passed to the channel's digital downconverter (DDC), implemented on the Zynq SoC's FPGA, to be translated to baseband by heterodyning with a 19 bit configurable local oscillator sinusoid generated by the Xilinx DDS Intellectual Property (IP) core.

Subsequently, each DDC channel's output is filtered by a two-stage polyphase Finite Impulse Response (FIR) LPF which, in addition to filtering the signal, decimates it by an overall decimation factor DF.

A profile chopper and integrator is implemented at the output of the cascaded FIR filter, which discards a configurable fraction — the duty factor, $D$ — of each received pulse. If required, a configurable number of consecutive pulses, specified by the pre-summing factor (PF), are coherently summed to reduce the PRF.

The finer details of the gateware can be found in [2]; what is important to highlight here

is that the gateware was designed under stringent data rate (DR) requirements where the maximum supported speed of data storage on the multi-media card (MMC) on the STEMlab was approximately 11 MB/s.

Using the equation

$$\mathrm{DR} = 2\left(4\,\frac{f_{\mathrm{OSC}}}{\mathrm{DF}}\right)\frac{\mathrm{CF}}{\mathrm{PF}} \quad [\mathrm{B/s}]\,, \tag{3.1}$$

the required throughput to sample the full 3.8 MHz of the IF spectrum is 30.4 MB/s which is beyond what the system can handle.

The original system used DF = 40, CF = 0.7 and PF = 2 to bring the required data rate to within the 10 MB/s throughput of the system in its original state. However, this means that only 3.125 MHz of the available 3.8 MHz IF bandwidth could be sampled unambiguously resulting in a loss of range.

The implementation of support for faster data rates was done in the scope of the current work and is discussed in greater detail in the following section. This implementation opens up opportunities for lower decimation factors, higher duty factors (resulting in a more efficient use of the modulation period), and higher PRFs (which makes the profile integrator redundant).

### Internet Protocol-Based Signal Recording

A significant challenge of the original version of the system, as has been identified in the previous section, was its inability to acquire the SAR data at a fast enough rate. The primary bottleneck was the MMC write speed which resulted in several compromises, to the detriment system performance, having to be made.

To address this, the fastest interface on the STEMlab, which is the gigabit Ethernet, was employed to offload data from the FPGA memory to a Raspberry Pi 4B which has a USB 3.0 interface capable of write speeds of up to 600 MB/s. This makes the 1 Gb/s transportation speed the data rate limitation.

Two protocols considered for this were Transmission Control Protocol/Internet Protocol (TCP/IP) and User Datagram Protocol/Internet Protocol (UDP/IP) implemented as shown in Figure 3.3.

The algorithm for implementation of the server (i.e. the Raspberry Pi) is as shown in Algorithm 1.

The algorithm for implementation of the client is as shown in Algorithm 2.

**Algorithm 1** IP-Based Signal Recording Server (Raspberry Pi)

```
Create TCP/UDP socket
Assign IP, PORT
Bind socket to port
Listen for incoming connections on socket. /* Blocking operation.*/

while an incoming socket connection is present and accepted do
    Open file for recording of binary data.

    while there is data in the TCP/UDP buffer do
        Read TCP/UDP buffer
        Write the read data to file
    end while

    if a new socket connection is not present then
        Block until a new socket connection is present.
    end if
end while

if socket connection accept failed then
    Exit
end if
```

**Algorithm 2** IP-Based Signal Recording Client (STEMLab)

```
Create TCP/UDP socket
Assign IP, PORT
Connect socket to server

for n ← 1 to NUM_PULSES do
    Transmit pulse
    Store received samples in FPGA memory
    Copy data from FPGA buffer to CPU
    Transmit data through TCP/UDP socket
end for

Close socket connection
```

While UDP offered a faster rate of packet delivery, the TCP/IP solution was adopted as the protocol of choice because it was able to achieve an acceptable average data rate of 43.231 MB/s for continuous recording intervals beyond 30 minutes, while guaranteeing packet delivery and in the same order in which the data is sent.

## 3.2 SAR Processing Chain

Equally significant to the SAR image quality as the radar hardware and firmware is the SAR data processing chain.

The miloSAR uses the G2 processor [35] which makes use of the range-Doppler algorithm (RDA). As such RDA is considered to be the standard processing approach in this work and other algorithms fall out of the current scope.

Of relevance to this work are the range processing and azimuth compression modules which improve signal to noise ratio (SNR) of a scatterer in the SAR image by the range processing gain and azimuth processing gain respectively.

### 3.2.1 Range Processing

During SAR image reconstruction, range compression is first performed to compress the received signal in the range dimension.

In the case of dechirp-on-receive FMCW systems, this is done by performing an FFT on the time domain IF data, along the fast time axis, to obtain a sequence of range profiles.

As derived in Appendix A, each range profile is a sum of spectral components corresponding to return echoes of scatterers in the scene. Each object's response is represented by

$$X_{\text{IF}}(t, t_a) = \exp(j(2\pi f_0 \tau_d + 2\pi k_r t \tau_d - \pi k_r \tau_d^2)) \ , \tag{3.2}$$

where

- $t$ is the fast-time variable,
- $t_a$ is the slow-time variable,
- $f_0$ is the center frequency of the transmitted band of frequencies,
- $\tau_d$ is the round trip delay time for the object, and
- $k_r$ is the transmitted ramp sweep rate

Markedly, this is a constant frequency sinusoid with a frequency that is directly proportional to target range, $R$, and is given by

$$f_{\text{IF}} = k_r \tau_d = \frac{2k_r}{c} R \quad [\text{Hz}] \ . \tag{3.3}$$

The last term in Equation 3.2 is the so-called residual video phase (RVP) and is removed during range processing by multiplying each pulse's IF spectrum by the quadratic phase filter transfer function $H_{\mathrm{RVP}}(f)$. The impulse response and corresponding transfer function for the filter are as follows:

$$h_{\mathrm{RVP}}(t) = \sqrt{-jk_r}\exp\left(j\pi k_r t^2\right) \xrightarrow{\mathcal{F}} H_{\mathrm{RVP}}(f) = \exp\left(-j\pi\frac{f^2}{k_r}\right) . \tag{3.4}$$

The range processing gain achieved by performing pulse compression is given by [36]

$$G_r = \frac{T_r B_N}{L_r} , \tag{3.5}$$

where $T_r$ is the ramp modulation period, $B_N$ is the receiver noise bandwidth and $L_r$ is SNR loss due to windowing, typically approximated to be the response broadening factor of the window function.

This is directly related to the waveform parameters which demonstrates the significance of this study for achieving optimal system performance.

### 3.2.2 Azimuth Processing

After the range processing routines, azimuth compression is performed to resolve targets by their Doppler shifts, thereby placing them at the correct azimuth locations.

Azimuth processing involves a coherent integration operation, to which the azimuth processing gain is attributed. Coherent integration is the complex vector sum of $N$ consecutive pulses in a collection of pulse data to increase SNR of the scatterer by a factor of $N$, otherwise known as integration gain.

The period over which the $N$ pulses are collected, given by $NT_r$, is known as the coherent processing interval (CPI).

Accounting for azimuth losses, $L_a$, the overall azimuth processing gain, $G_a$, is given by

$$G_a = \frac{N}{L_a} , \tag{3.6}$$

where, for a broadside stripmap configuration, the number of pulses coherently integrated is given by [36]:

$$N = \frac{\mathrm{PRF}\cdot\lambda\cdot R\cdot\kappa_a}{2\cdot\delta a\cdot v} . \tag{3.7}$$

$\kappa_a$ is the azimuth impulse response broadening factor, $\delta a$ is azimuth resolution, and $v$ is platform velocity.

In the specific case of an RDA processor (and other similar algorithms), an FFT is performed on the vector of range profiles along the azimuth dimension, wherein the coherent integration occurs, to obtain a range-Doppler map (RDM). The phase history of a point target in the range-Doppler plane is that of an azimuth chirp and by matched filtering of the RDM with a sequence of azimuth reference chirps, the targets are focused into the appropriate azimuth locations.

A conventional azimuth reference function for range $R$ and as a function of the pulse index $n$ is [37]

$$h_a(R, n) = \exp\left(\frac{2\pi f_0 n^2 v^2}{c \cdot R \cdot \mathrm{PRF}} - \frac{4\pi f_0 v^2 n}{c^2 \cdot \mathrm{PRF}}\right). \tag{3.8}$$

The filtering operation is, efficiently, performed as a multiplication of the RDM and the frequency domain form of the azimuth reference vector.

## 3.3 System Performance

A brief overview of the miloSAR's structure and signal processing routines has been given in the preceding sections; however, clear descriptions of how the system's performance is evaluated, how it actually performs and how performance can be improved are yet to be given.

The present section addresses the first aspect by exploring themes related to performance and by defining performance metrics as a precursor to performance characterisation and optimisation exercises carried out in the chapters to follow.

### 3.3.1 Signal to Background Ratio

The end goal of SAR is to produce imagery which represents objects within the illuminated scene. As such, maximising visibility of the objects is the fundamental objective in SAR system design and detection of specific objects of interest in the image is influenced by the signal-to-background ratio (SBR) [38].

The 'signal' is the return from a point-like scatterer in a single resolution cell or a distributed scatterer such as terrain having many scatterers per resolution cell and the

background refers to a combination of total noise and background clutter when not the target of interest.

### System Noise

Total noise, $\sigma_N$, involves combining the contributions of various noise sources, which can be classified as additive noise or multiplicative noise and are characterised by the effective backscatter coefficient of additive noise, $\sigma_n$, and multiplicative noise ratio (MNR) respectively. This is represented by [38]

$$\sigma_N = \sigma_n + (\text{MNR})\bar{\sigma}_0 \ , \tag{3.9}$$

where $\bar{\sigma}_0$ is the average backscatter coefficient of local terrain[1] (RCS per unit ground area).

Multiplicative noise comprises, primarily, integrated sidelobes of the system impulse response, quantisation noise, and energy due to range and azimuth ambiguities. It is formulated as follows:

$$\text{MNR} = \text{ISR} + \text{QNR} + \text{AMBR} \ , \tag{3.10}$$

where ISR is integrated sidelobe ratio (discussed in the forthcoming section), QNR is quantisation noise ratio and AMBR is ambiguity ratio.

The energy of the noise sources is distributed in the neighborhood, in the entire scene, and outside the scene respectively. According to Equation 3.9, the impact of multiplicative noise is influenced by the received signal level; and as will be shown, MNR dictates the image contrast ratio between uniform clutter and dark, in an RCS sense, regions e.g. radar shadows [39].

Additive noise is spatially distributed within the whole image and, unlike MNR, it is not related to the received signal level. In fact, it exists even in the absence of the received signal.

Figure 3.4 shows the PSD of the sampled signal for the first receive channel[2] with the transmit synthesiser powered down and input ports into the receive chain terminated. The local oscillator synthesiser was kept on, since it is a part of the receive chain, but its output ports were also terminated.

It can be observed that the receiver has an average noise floor with a PSD of -121.741

[1]Tables can be found for typical values of $\bar{\sigma}_0$ for various types of terrains at different frequencies.
[2]The result for the second receive channel is very similar.

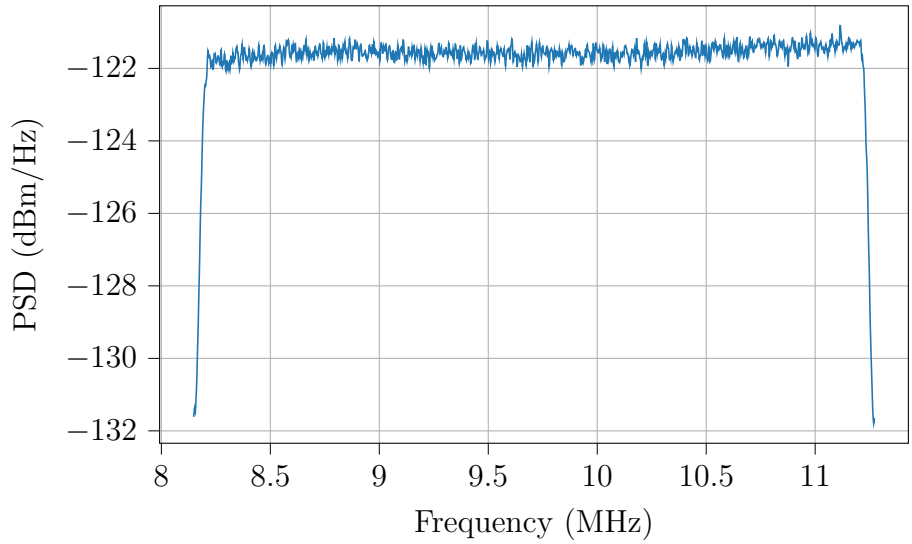


**Figure 3.4:** Noise floor of receiver.

dBm/Hz.

Another important performance metric is the clutter to radar receiver noise ratio (CNR) given by [38]

$$\text{CNR} = \frac{P_{av} G_A^2}{2 N_0 L} \left( \frac{\lambda}{4\pi R} \right)^3 \left[ \frac{\sigma_0 \cdot \delta r}{\kappa_r v \sin(\alpha_{dc}) \cos(\psi_{ac})} \right] \tag{3.11}$$

where

- $P_{av}$ is the average transmitted power in Watts (W),
- $G_A$ is the antenna gain,
- $L$ is a loss factor,
- $\delta r$ is range resolution,
- $\alpha_{dc}$ is the Doppler cone angle,
- $\psi_{ac}$ is the grazing angle, and
- $N_0$ is the one-sided receiver noise power spectral density (W/Hz), given by

$$N_0 = kTF_N \ , \tag{3.12}$$

where $k$ is Boltzmann's constant ($1.38 \times 10^{-23}$ J/K), $T$ is the ambient temperature in Kelvins (K), and $F_N$ is the receiver noise figure.

This is related to the aforementioned additive noise by [38]

$$\text{CNR} = \frac{\sigma_0}{\sigma_n} \ , \tag{3.13}$$

where $\sigma_n$ is the effective backscatter coefficient of the additive noise which represents the

equivalent terrain radar backscatter coefficient giving rise to a signal in the receiver equal to the receiver noise signal.

### Signal to Noise Ratio

SAR signal to noise ratio (SNR) is given by the ratio of the received power as computed from the radar range equation (RRE) to the receiver noise and with the processing gains applied:

$$\text{SNR} = G_r G_a \frac{P_{av} G_A A_e \sigma_t}{(4\pi)^2 R^4 N_r L} \tag{3.14}$$

where

| | |
|---|---|
| $G_A$ | is the transmit antenna gain, |
| $A_e$ | is the receive antenna effective aperture area in square meters ($m^2$), |
| $\sigma_t$ | is the target radar cross section (RCS), |
| $L$ | encapsulates losses such as atmospheric loss, microwave transmission loss etc., |
| $G_r$ and $G_a$ | are the range processing gains discussed in the previous section. |

Substituting $T_r = D \cdot T_p$ in Equation 3.5 where $D$ is the duty factor and $T_p$ is pulse duration; and $\text{PRF} = 1/T_p$ in Equation 3.6 gives a convenient result for SNR:

$$\text{SNR} = \frac{D \cdot B_N}{L_r} \cdot \frac{\lambda \cdot R \cdot \kappa_a}{2 \cdot \delta a \cdot v} \cdot P_r \tag{3.15}$$

where duty factor is the waveform parameter to be increased to achieve a higher SNR.

### Signal to Clutter Ratio

As mentioned, the second limitation to object detection in the SAR image is signal to clutter ratio (SCR).

In most cases, the system specification for noise is such that background clutter (i.e. returns from the rest of the scene and not the specific target of interest) is first to limit visibility of a specific target of interest in the SAR image before noise is even a concern.

SCR is given by

$$\text{SCR} = \frac{\sigma_t \cos(\psi_{ac})}{\sigma_0 \cdot \delta a \cdot \delta r} \tag{3.16}$$

where $\sigma_t$ is the RCS of the target in local clutter.

### 3.3.2 Impulse Response

Given that a SAR system is nominally linear, its response can be understood via its impulse response (IPR). This is the response of the system while imaging a hypothetical, infinitesimally small scatterer having an RCS such that it can be observed in the SAR image[3].

The IPR is also referred to in other literature as the point spread response (PSR)[4] or point spread function (PSF). However, 'impulse response' appears more frequently in literature, thus, is adopted in the present work for consistency.

Since the output of a 2D SAR system[5] is a 2D complex reflectivity map of the imaged scene, its IPR is also a 2D entity with a range component ($\text{IPR}_r$) — obtained by taking a slice across the range dimension of the SAR image for a constant azimuth time — and an azimuth component ($\text{IPR}_a$) — obtained by taking a slice across the azimuth dimension for a constant range.

Figure 3.5 shows an IPR obtained via the model described in Section 3.4.

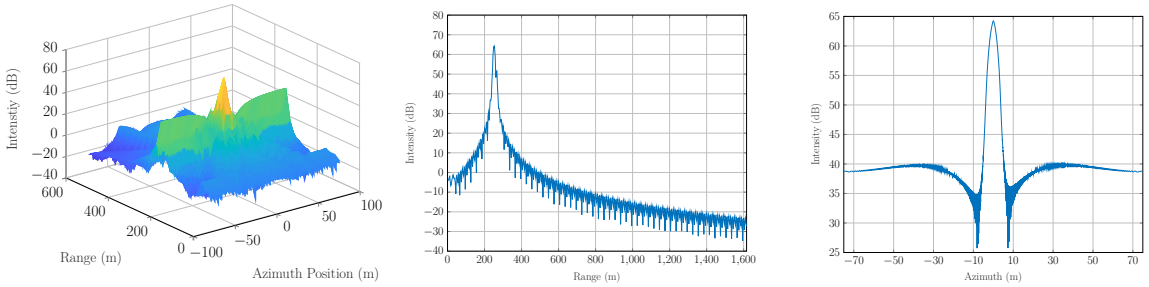


**(a)** **(b)** **(c)**

**Figure 3.5:** IPR of simulated dechirp-on-receive SAR system. Shown are the (a) 3D view of IPR (b) range IPR (c) azimuth IPR.

The impulse response is as expected with peaks at the correct range and azimuth locations. $\text{IPR}_a$ shows an interesting shape which is not what a typical matched filter response would look like due to the antenna weighting function and uncertainties inherent in the estimated azimuth reference chirp.

In practice, the IPR can be approximated by measuring the response of the system to a corner reflector. The range IPR can also be approximated using a loopback cable as will

[3]Otherwise known as an isotropic point scatterer.

[4]This is recommended by Showman [40] over the term 'impulse response' which is typically used in the context of linear time invariant (LTI) systems. The time invariance property is not satisfied by SAR systems.

[5]3D SAR systems also exist but the focus of the current work is on 2D systems.

be shown in future sections.

### 3.3.3 Image Quality Metrics

Image quality (IQ) of the generated SAR image is dictated, primarily, by the IPR; hence, several image quality metrics are derived from the IPR characteristics.

The rest of this section discusses the commonly used image quality metrics which will be essential for evaluation of results in this work.

#### Resolution

Spatial resolution, by the Rayleigh criterion, refers to the distance between the peak and the first null of the IPR [40].

For the FMCW waveform, resolution in the range dimension is well known to be given by

$$\delta r = \frac{c\kappa_r}{2B_r} \,, \tag{3.17}$$

where $c$ is the signal velocity, $\kappa_r$ is a factor to account for bandwidth reduction (mainlobe broadening) caused by a sidelobe apodization weighting function and low-frequency phase errors in the signal and $B_r$ is the modulation bandwidth.

Azimuth resolution, at range $R$, is also well documented to be approximated by [40], [41]

$$\delta a \approx R\theta_{\mathrm{SAR}} \approx \frac{R\lambda}{2D_{\mathrm{SAR}}\cos\theta} \,, \tag{3.18}$$

where $\theta_{\mathrm{SAR}}$ is the the (two-way pattern) azimuth beamwidth of the synthesised antenna and $D_{\mathrm{SAR}}$ corresponds to the synthetic aperture size which is related to aperture or dwell time, $T_a$, by [40], [41]

$$D_{\mathrm{SAR}} = vT_a \,. \tag{3.19}$$

Aperture time is, however, limited by the physical antenna beamwidth at the range of interest and the maximum effective aperture time that can be achieved is

$$T_{a_{max}} = \frac{R\theta_{az}}{v} \tag{3.20}$$

which results in a bound on the achievable azimuth resolution.

### Peak Sidelobe Ratio

High levels of sidelobes in the IPR are problematic and can severely impact performance of the SAR system.

Sidelobes associated with a bright — in an RCS sense — target may mask weaker targets located near the strong one. Additionally, they, erroneously, add energy into adjacent resolution cells which resembles the presence of a target that is not actually there.

The peak sidelobe ratio (PSR) is a measure of the sidelobe level close to the peak and is defined as the ratio of the peak sidelobe intensity to the peak mainlobe intensity [40], [41] and is formulated as[6]

$$\mathrm{PSR}|_{\mathrm{dB}} = 10\log_{10}\frac{|y_M|^2}{|y_S|^2}\,, \tag{3.21}$$

where $|y_M|^2$ is the peak intensity of the mainlobe and $|y_S|^2$ is the peak intensity of the sidelobes.

### Integrated Sidelobe Ratio

Integrated sidelobe ratio (ISR) is the ratio of total sidelobe energy to that of the mainlobe [38] computed as[7]

$$\mathrm{ISR}|_{\mathrm{dB}} = 10\log_{10}\frac{\int_{-\infty}^{a}|y(\eta)|^2 d\eta + \int_{b}^{\infty}|y(\eta)|^2 d\eta}{\int_{a}^{b}|y(\eta)|^2 d\eta}\,, \tag{3.22}$$

where $a$ and $b$ are the limits for the region of the IPR corresponding to the main lobe and $|y(\eta)|^2$ is the intensity at either range or azimuth spatial frequency $\eta$.

ISR is very important in distributed clutter and multi-scatterer environments such as SAR. When imaging an evenly distributed weaker scene, ISR degrades contrast and makes low return and shadow areas appear less dark in the image. This is further shown in the next section where the significance of MNR, of which ISR is a key component, in the contrast metric is demonstrated.

[6] The equation can be deduced directly from the given definition.

[7] The equation can be deduced directly from the given definition, taking the energy of the signal over a finite period as $E_x = \int_a^b |x(t)|^2 dt$ for a continuous time signal and $E_x = \sum_{n=a}^{b} |x[n]|^2$ for a discrete time signal as defined in most signal processing literature.

**Contrast Ratio**

Contrast ratio between two regions in the SAR image is ratio of the image intensities in the two regions.

In a task where the objective is to detect a point target in local clutter, such as mine detection, the point target contrast ratio (PTCR) is relevant and is given by [38]

$$\text{PTCR} = \frac{\frac{\sigma_t \cos(\psi_{ac})}{\delta a \cdot \delta r} + \sigma_n + \text{MNR} \cdot \bar{\sigma}_0}{\sigma_0 + \sigma_n + \text{MNR} \cdot \bar{\sigma}_0} \tag{3.23}$$

where the target of interest has the RCS $\sigma_t$ in local clutter of backscatter coefficient $\sigma_0$ within a larger scene of average backscatter coefficient $\bar{\sigma}_0$.

The significance of SCR and system noise are evident here.

Without noncoherent integration (NCI), a standard PTCR requirement is 15 dB for reliable point detection [38].

## 3.4 System Simulation Model

Using the functional specifications in Table 3.6 analytical development carried out in Appendix A, a model was derived for the miloSAR to satisfy RO4.

**Table 3.6:** miloSAR Functional Specifications

| **Specification** | **Symbol** | **Current** | **Required** |
|---|---|---|---|
| SAR mode | | Stripmap | |
| Operational Frequency | | 2.35 — 2.525 GHz (nom. $f_c = 2.4$ GHz) | |
| Bandwidth | BW | $\leq$ 175 MHz | |
| IF Sampling Rate | $f_s$ | 3.125 MHz | 3.8 MHz |
| Peak Transmit Power | $P_t$ | 22 dBm | Undefined |
| System Impedance | $Z$ | 50 Ω | |
| Antenna azimuth beamwidth | $\theta_{az}$ | $\sim 70.517°$ | Undefined |

A MATLAB® implementation of this model is given in Appendix C.

The model assumes a simple, single-phase-center, single-beam, perfectly efficient, uniformly-

illuminated aperture antenna whose far-field pattern is given by [42], [43]

$$F(\theta) = \text{sinc}\left(\frac{D_{az}}{\lambda}\sin\theta\right), \tag{3.24}$$

where $D_{az}$ is the physical size of the antenna in the azimuth dimension and $\theta$ is the direction of arrival angle with respect to broadside.

The general normalised power pattern is given by

$$P(\theta) = |F(\theta)|^2 \tag{3.25}$$

The arrival angle, $\theta$, is related to azimuth position, $x$, by

$$\theta = \tan^{-1}\left(\frac{vt_a}{R_0}\right) \tag{3.26}$$

where $R0$ is the minimum range during acquisition from the scatterer to antenna's phase center, $v$ is the platform velocity and $t_a$ is azimuth time, sampled at the PRF. This allows for computation of the power as a function of azimuth position, $P(x)$ and the result is as shown in Figure 3.6. This is used as a weighting function on the simulated reflected target echoes.

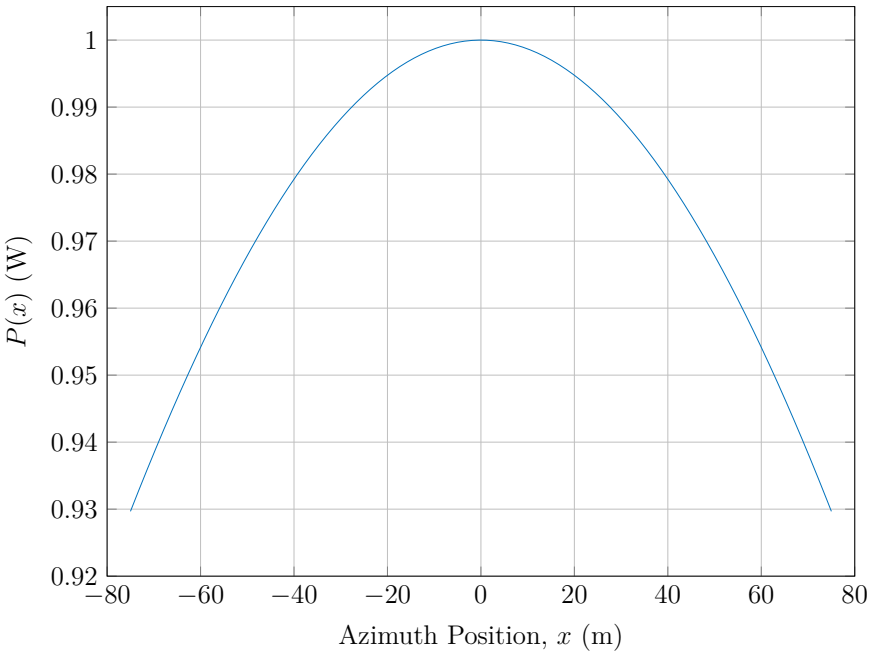


**Figure 3.6:** Normalised antenna power pattern for modelled antenna.

The above described model was used throughout the current study to validate design

choices, to support theoretical predictions and to observe the effects of phase and frequency instabilities.

As previously mentioned, the main benefit of such a model, however, is that it will allow for rapid design and analysis of the miloSAR and algorithms to be performed on the data without requiring time consuming experiments.

## 3.5 Summary

A brief outline of the miloSAR's hardware, firmware and processing routines has been presented in this chapter.

The details of the system's architecture and operational principle were discussed to give context to the work done on improving its performance.

The implementation of a TCP/IP-based signal acquisition module enabled the system to store SAR data at a much faster rate than it was previously capable of. This allows the system to be used with higher PRFs and sampling rates and for extended periods of time, without the 28 GB storage limitation due to the MMC previously used. Performance characterisation, in this regard, is detailed in Chapter 6.

A review of the data processing routines was also carried out and the most commonly used performance and IQ metrics namely signal to background ratio, resolution, peak sidelobe ratio, integrated sidelobe ratio, and contrast ratio were discussed for use in evaluation of system performance.

System noise characterisation was also performed and it was found that the system has a noise floor of -121.741 dBm when no return signal is present, which is essential in quantifying the contributions of phase noise assessed in the forthcoming sections.

Finally, a model of the miloSAR was created and will prove useful in the next chapters for investigating how the system responds to various design changes.

# Chapter 4

# Fractional-N PLL-Based Waveform Synthesis

Measurements made by SAR systems are influenced by the parameters of their synthesised signals.

To this end, rigorous design and analysis of the frequency synthesiser, and waveforms thereof, has been carried out and the primary aspects of this are presented in the current chapter.

This chapter is divided into two major sections. The first focuses on the PLL synthesiser used in the miloSAR. It starts off with a brief overview of the PLL architecture and then segues into the practicalities of frequency synthesis using the said synthesiser.

The second section deals with the waveform component and discusses the critical parameters of FMCW signals, their interactions with each other and the role they play in the system performance.

By carefully analyzing and integrating the findings from this chapter, effective strategies and approaches to optimise system performance are devised and demonstrated in Chapter 6.

## 4.1 Phase-Locked Loop Architecture

Phase-locked loops (PLLs) are a prevalent approach to generating stable output frequencies from reference clocks and can be found in a vast amount of electronic systems requiring high frequency sources.

A simplified architecture diagram for a typical PLL has been presented in Figure 2.6 and the advantages and disadvantages of using this approach to frequency synthesis have been reviewed in Section 2.4.1.

The current section examines the finer details of the architecture of a PLL in relation to the LMX2492EVM. Its significance lies in providing contextual information and identifying potential opportunities for the waveform design and optimisation process.

### Reference Input Clock and R-Divider

A single ended or differential input reference clock with a frequency of $f_{\text{OSC}}$, which may be scaled by a factor of $1/R$ by the R-divider, is supplied to the PLL. This is tracked by the VCO which outputs a scaled replica of the reference and whose instantaneous frequency is given by

$$f_{\text{VCO}} = N f_{\text{PD}} \ , \tag{4.1}$$

where $f_{\text{PD}}$ is the phase detector frequency given by $f_{\text{OSC}} \cdot 1/R$ and $N$ is the N-divider value discussed shortly.

As previously stated, it is the 125 MHz differential square wave from the TXC Corporation CXO BFBC90 on the STEMlab 125-14 that is used as the reference input.

### Phase Detector and Charge Pump

To determine the phase error between the reference input and the VCO output, one of several phase detection schemes is used. These are discussed in literature such as [44] and [45].

Relevant to the current design is the tri-state, digital phase frequency detector (PFD) with a charge pump (CP) and whose output depends not only on the phase error but also frequency error.

The charge pump consists of a pair of — ideally, symmetric — current sources [1] switched on by the phase detector logic. One sources current, $I_{\text{CP}}$, to the output, whereas the other sinks the same amount from the output.

Operation of the phase detector can be represented by the finite state machine shown in Figure 4.1, where state transitions are triggered by the rising edges (or falling edges or even both, depending on the configuration) of the reference clock and the VCO output

[1] Usually CMOS transistors.

signals. This is relevant in understanding the linearity limitation of the PFD and the cycle-slips observed in the PLL output under certain circumstances.

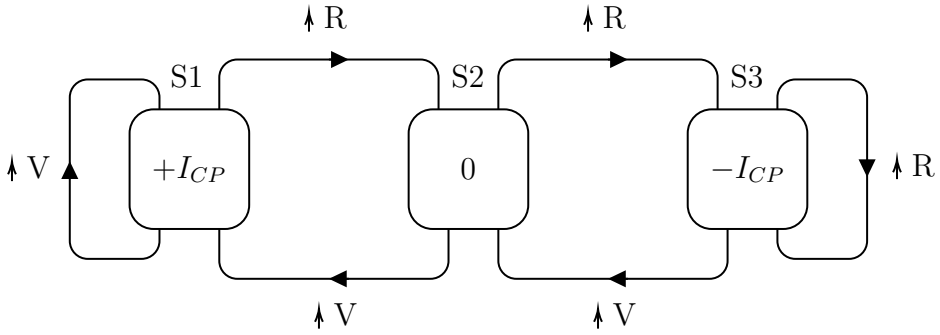


**Figure 4.1:** State diagram for the tri-state PFD.

Each current pulse's width is, therefore, proportional to the phase difference between the PFD's two inputs. As such, a current pulse is delivered by the charge pump to the loop filter for a duration of $t_{\mathrm{CP}}$, and since each cycle has a period of $2\pi/\omega_{\mathrm{OSC}}$, the average current over a single cycle is given by [46]

$$\bar{i}_{\mathrm{CP}} = \frac{I_{\mathrm{CP}}\ \phi_e}{2\pi} = K_{\mathrm{PD}}\ \phi_e \quad [\mathrm{A}]\ , \tag{4.2}$$

from which the phase detector gain is defined as

$$K_{\mathrm{PD}} = \frac{I_{\mathrm{CP}}}{2\pi} \quad [\mathrm{A/rad}]\ . \tag{4.3}$$

The value of $I_{\mathrm{CP}}$ is programmable in the LMX2492 and has a considerable impact on the system as will be revealed in the forthcoming sections. Throughout the rest of this work, $I_{\mathrm{CP}}$ will be referred to as the *charge pump gain* (CPG) to be consistent with the nomenclature used by the manufacturers of the LMX2492 [47].

A characteristic curve for the full relationship between the phase error and average charge pump output is as shown in Figure 4.2. Phase errors of greater than $2\pi$ result in the PFD behaving as though phase error cycled back to 0 zero which implies periodicity with a period of $2\pi$.

The size of the phase error defines three regions of interest for operation of the synthesisers.

1. **Linear Region ($-2\pi < \phi_e < 2\pi$):** When the PFD is operating within the linear region, this is typically defined as the *locked state* and the relationship $\bar{i}_{\mathrm{CP}} = K_{\mathrm{PD}}\ \phi_e$ is valid. The fact that the PFD characteristic behaviour, in this state, can be described by a linear equation makes it possible to use Laplace transform tools to analyse and design the system in the Laplace domain for this region.

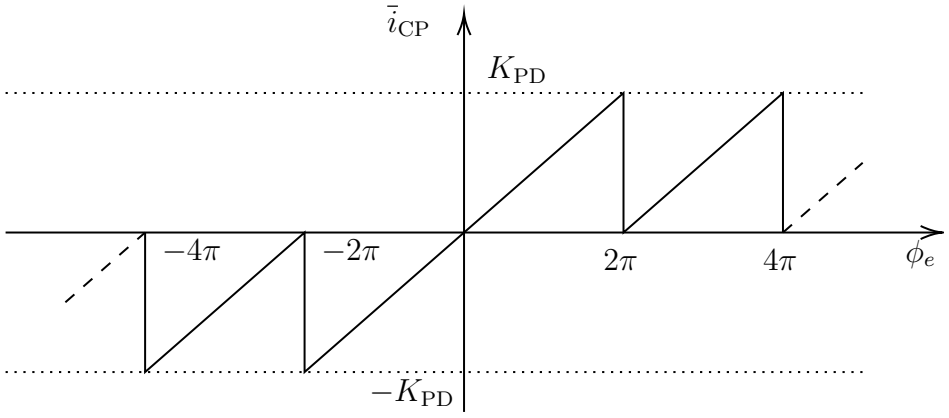


**Figure 4.2:** PFD characteristic curve showing the averaged charge pump, $\bar{i}_{\mathrm{CP}}$, output versus phase error, $\phi_e$.

2. **Dead Zone of Linear Region:** When the phase error is near zero, it is important to note that there are, in reality, non-idealities such as unequal sink and source currents, as well as non-zero turn-on times of the sink and source currents.

   The non-zero turn on times of the MOS devices have the effect of significantly decreasing the slope around $\phi_e = 0$ which means that the value of $K_{\mathrm{PD}}$ is significantly decreased thereby increasing the loop bandwidth. This will result in inability to suppress VCO noise, phase noise and spurs if not compensated for.

3. **Non-linear Region ($\phi_e < -2\pi,\ \phi_e > 2\pi$):** A phase error larger than $2\pi$ implies that there is a full frequency error and the PLL is in the *unlocked state*.

   While the PFD output current will be in the correct direction, the time averaged current is not necessarily directly proportional to the phase error.

   A consequence of this are 'cycle slips' which manifest as spikes in the time domain response and occur when two rising edges (or falling or both edges, depending on the configuration) from one input are encountered before the edge from the other input. Because the PFD would already be supplying a correction pulse to respond to the first edge, it ignores the second edge which leads to an erroneous correction current.

### Loop Filter

The loop filter is a significant element in the PLL and it greatly impacts the loop characteristics e.g. loop bandwidth, frequency agility, loop stability, noise performance etc.

It is a low pass filter whose main role is to convert the charge pump's output current into a tuning voltage for the VCO. Furthermore, the loop filter smooths the charge pump output,

which is discretised and would, otherwise, correspond to a ramp staircase waveform.

The LMX2492EVM board layout provides footprints for fourth order degenerate[2] passive and active loop filters where one has to be selected and whose structures are as shown in Figure 4.3.

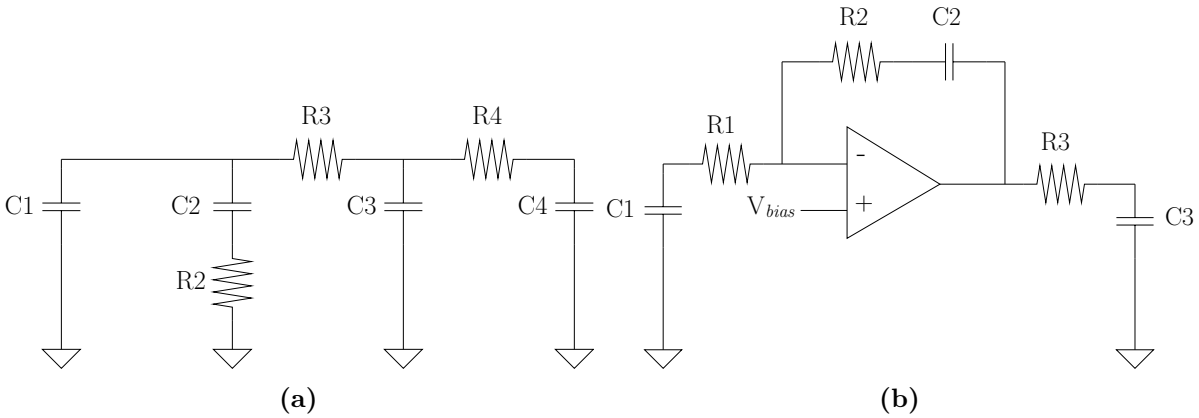


**Figure 4.3:** (a) Passive and (b) active loop filter circuits onboard the LMX2492EVM.

The active filter also provides amplification of the VCO control voltage which allows for a larger output frequency bandwidth at the expense of amplifier related distortion and noise. For simplicity, only the passive loop filter is used in the current version of the miloSAR.

### Voltage Controlled Oscillator and VCO Divider

As the name suggests, the voltage controlled oscillator (VCO) generates a frequency based on the voltage applied at its tuning pin. The output signal has an angular frequency given by

$$\omega_o(t) = \omega_{fr} + K_{\text{VCO}} V_{tune}(t) \ , \tag{4.4}$$

where $\omega_{fr}$ is the VCO free-running frequency and $K_{\text{VCO}}$ is the VCO sensitivity in rad/s/V.

A challenge with using VCOs to directly synthesise the waveforms, however, is that the relationship between the tuning voltage and the output frequency is not linear and $K_{\text{VCO}}$ takes on different values over the VCO range. For this reason, the VCO is enclosed in the PLL negative feedback loop to linearise the input-output relationship.

Other non-idealities such as VCO ripple are discussed in [46]; these are not of much

[2]A degenerate filter is one with zero valued components either unintentionally or intentionally where, in the latter case, this may be done so that a printed circuit board is made for a larger order filter and then by using zero valued components, a filter of a lower order may be realised

concern in this work.

The current PLL system uses the RFVC1843 [48] VCO over the range 9.4 GHz[3] to 10.1 GHz with a passive loop filter, though it can reach up to 11.3 GHz with an active loop filter. This output is then divided down by a factor of 4 using the integrated VCO divider such that an S-band radar operating at a center frequency of 2.4375 GHz with a 175 MHz bandwidth is realised as desired.

### Delta-Sigma Modulator-Based N-Divider

A frequency divider making use of the Delta-Sigma modulator is incorporated in the negative feedback path to downscale the VCO output by a programmable factor of $N$ such that the divider's output can be compared and synchronised to the reference clock.

In the case of an integer-N PLL, $N$ is an integer value and implementation of the clock divider can be done using a pre-scaler and a CMOS counter. The primary drawback of integer-N PLLs is that the PLL would have a coarse frequency tuning resolution. A fractional-N PLL solves this problem by allowing for fractional values of $N$ which can be expressed as

$$N = N_{int} + \alpha \ , \tag{4.5}$$

where $N_{int}$ is the integer part and $\alpha$ is the fractional part.

Since frequency dividers are digital circuits that can only, inherently, support integer values, dividing by a fractional value is achieved through dividing by a sequence of integers i.e.

$$N = N_{int} + y[n] \ , \tag{4.6}$$

with the result that the average output frequency is the desired fractional value.

The instantaneous value of $N$ is not correct and the instantaneous frequency errors $y[n] - \alpha$, also referred to as quantisation noise, give rise to N-divider phase noise on the PLL output.

A design objective becomes selecting a sequence $y[n]$ such that $y[n] - \alpha$ has little low frequency content (in the region where it is not suppressed by the low-pass filtering function of the PLL) and also is not periodic, which would result in strong spurious content.

[3]The datasheet [48] quotes 9.8 GHz as the minimum; however, from experiential knowledge, the VCO can, safely, be operated at 9.4 GHz.

A popular means to satisfy both requirements is through the Delta-Sigma modulator which entails enclosing a quantiser in a negative feedback loop as shown in Figure 4.4.

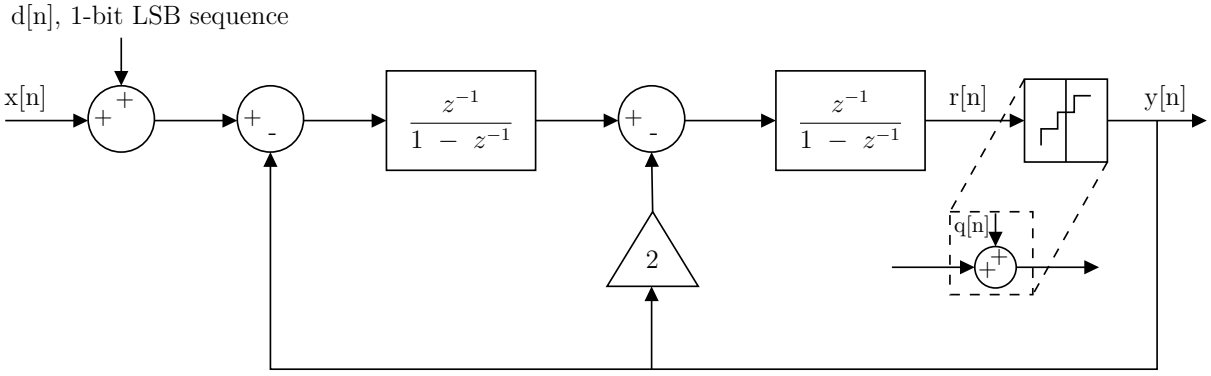


**Figure 4.4:** Delta-Sigma modulator block diagram.

The quantiser rounds fractional values to nearest integers and can be thought of as an additive error source, $q[n]$ [49]. Without giving too much detail, for this loop, the quantisation noise can be shown to be

$$y[n] - \alpha = q[n] - 2q[n-1] + q[n-2] \ , \tag{4.7}$$

and because the right hand side is a second order difference equation, the quantisation noise is high-pass filtered which leads to it having little low frequency content as desired.

Adding a random 1-bit to the least significant bit of the input is referred to as (1-bit) dithering and is incorporated to break up any periodic behaviour of y[n] such that there is less spurious content in the PLL output.

## 4.2 Phase Domain Transfer Function Model of Synthesiser

Representing the dynamics and steady state behaviour of the PLL system by means of the phase domain transfer function model allows for the description of several of its characteristics such as its time dependent outputs and frequency response.

This is done to enable rapid design iterations without having to carry out time and labour intensive experiments and the modelling partially satisfies RO4.

The validity space of the model is, however, constrained by the magnitude of the phase excursion of the feedback signal relative to the reference. This should be within the range

of linearity of the PLL which is, for the PFD PLL, $|\phi_e| < 2\pi$.

Figure 4.5 illustrates the phase domain model of the PLL.

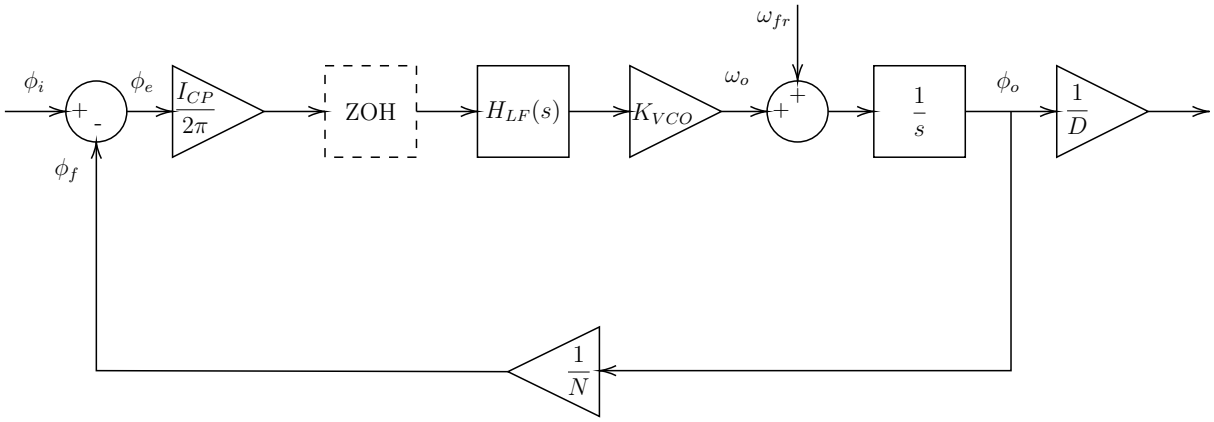


**Figure 4.5:** Phase domain transfer function model of PLL synthesiser.

The model supplies a phase reference, $\phi_i$, which is modulated in a way that is different but equivalent to the real system. In the real system, the reference remains constant, and excitation of the system is achieved by modulating $N$ to change the value of $\phi_f$.

The PFD and charge pump are represented by a subtractor and a gain $K_{\mathrm{PD}} = I_{\mathrm{CP}}/2\pi$ derived in Equations 4.2 and 4.3.

$Z_{\mathrm{LF}}(s)$ is the loop filter transfer function derived in [45] to be

$$Z_{\mathrm{LF}}(s) = \frac{1 + \tau_2 s}{s(a_3 s^3 + a_2 s^2 + a_1 s + a_0)} \ , \tag{4.8}$$

where

$$\tau_2 = R_2 C_2 \ . \tag{4.9}$$

and the expressions for computing the filter coefficients are given in Appendix D.

The VCO, as described by Equation 4.4, is modelled by the gain block, $K_{\mathrm{VCO}}$, and the summer which sets the free-running frequency of the VCO (i.e. the initial VCO output when the VCO tuning voltage is 0 V). The $1/s$ integrator block converts the VCO output frequency back into phase[4].

In the feedback path is the N-divider or 'sensor' having a gain of $1/N$ and denoted by $H(s)$ as is the convention in Control theory.

[4]Phase is the time integral of frequency.

A parameter known as loop gain is also commonly defined in PLL literature [44], [45] as

$$K = \frac{K_{\mathrm{PD}} K_{\mathrm{VCO}}}{N} = \frac{\mathrm{CPG} \cdot K_{\mathrm{VCO}}}{2\pi \cdot N} \, . \tag{4.10}$$

Another deviation of the model from the real case is through use of the continuous time Laplace variable, $s$, which is not necessarily appropriate given that the PLL behaves as a discretised system due to sampling action of the PFD.

Gardner [46] gives a thorough analysis of the validity of the continuous time approximation, the details of which are far too vast to recapitulate here. The conclusion he arrives at is that, switching granularity effects can be neglected if $\omega_i/K > 7.5$ where $K$, in [46], is defined as

$$K = 2\zeta\omega_n \, . \tag{4.11}$$

For some margin, $\omega_i/K$ of at least 10 is what is recommended as a conventional rule of thumb; this criteria is met in the present context.

All this leads to a set of important phase domain transfer functions presented in Table 4.1 which will be used to investigate and design the frequency and dynamic response of the system.

**Table 4.1:** Phase Domain Transfer Functions of the PLL

| **Name** | **Symbol** | **Transfer Function** |
|---|---|---|
| Feedforward Transfer Function | $G(s)$ | $G(s) = \frac{K_{\mathrm{PD}} K_{\mathrm{VCO}} Z_{\mathrm{LF}}}{s}$ |
| Open-loop Transfer Function (OLTF) | $G_o(s)$ | $G_o(s) = G(s)H(s) = \frac{K Z_{\mathrm{LF}}(s)}{s}$ |
| System Transfer Function | $Z_{\mathrm{PLL}}$ | $Z_{\mathrm{PLL}} = \frac{G(s)}{1+G(s)H(s)} = \frac{KN(1+\tau_2 s)}{a_3 s^5+a_2 s^4+a_1 s^3+a_0 s^2+K\tau_2 s+K}$ |
| VCO Tune Voltage Transfer Function | $Z_{V_{tune}}$ | $Z_{V_{tune}} = \frac{K_{\mathrm{PD}} Z_{\mathrm{LF}}}{1+G(s)H(s)} = \frac{sK_{\mathrm{PD}}(\tau_2 s+1)}{a_3 s^5+a_2 s^4+a_1 s^3+a_0 s^2+K\tau_2 s+K}$ |
| VCO Output Transfer Function | $Z_{f_{\mathrm{VCO}}}$ | $Z_{f_{\mathrm{VCO}}} = \frac{K_{\mathrm{PD}} K_{\mathrm{VCO}} Z_{\mathrm{LF}}}{1+G(s)H(s)} = \frac{sK_{\mathrm{PD}} K_{\mathrm{VCO}}(\tau_2 s+1)}{a_3 s^5+a_2 s^4+a_1 s^3+a_0 s^2+K\tau_2 s+K}$ |
| Complementary Sensitivity Function (Feedback Transfer Function) | $Z_{\phi_2'}(s)$ | $Z_{\phi_2'}(s) = \frac{G(s)H(s)}{1+G(s)H(s)} = \frac{K(1+\tau_2 s)}{a_3 s^5+a_2 s^4+a_1 s^3+a_0 s^2+K\tau_2 s+K}$ |

| | | |
|---|---|---|
| Sensitivity Function (Error Transfer Function) | $Z_{\phi_e}(s)$ | $Z_{\phi_e}(s) = \frac{1}{1+G(s)H(s)} = \frac{s^2(a_3s^3+a_2s^2+a_1s+a_0)}{a_3s^5+a_2s^4+a_1s^3+a_0s^2+K\tau_2s+K}$ |

The last four transfer functions can be grouped as 'closed-loop' transfer functions as they relate to the output obtained by the PLL when operating in its closed-loop feedback mode.

The polynomial in the denominator of the closed-loop transfer functions is known as the *characteristic polynomial*. In this case, its highest power of $s$ is 5, which means that this is a fifth-order PLL. The roots of the polynomial show that the PLL has five poles, three of which are contributed by the third order loop filter. The zero is a critical aspect of loop stability, a concept which is discussed in further detail in Section 4.3.

In Control theory, a closed-loop system is also characterised by its 'Type' which is obtained from determining the number of $1/s$ terms that can be factored out of the closed-loop transfer functions. This has implications as is shown in Section 4.4 on the steady state error when the PLL is required to track an input signal. The current PLL is Type II which is the most common kind on the market.

## 4.3 Frequency Response of Synthesiser

Steady state behaviour of the PLL in response to sinusoids of varying frequency is observed through Bode plots which foster the design and analysis of the PLL's frequency domain characteristics.

This is important in the present study because phase and frequency instability is, for the most part, analysed in the frequency domain and the frequency response shapes of the closed-loop transfer functions represent the filtering characteristics of the PLL on the spectrum of its output signal.

Furthermore, certain parameters that play a critical role in the dynamic behavior of the PLL, such as loop bandwidth and stability margins, appear as distinctive points on the Bode plots.

It will be shown that, generally, a larger loop bandwidth results in poor frequency response characteristics but better dynamic response characteristics and the implications of this will also be demonstrated.

### 4.3.1 Open-Loop Frequency Response

The open-loop frequency response is used in Control theory for frequency-response design to improve transient response and steady state tracking error constants as well as for closed-loop stability assessment among other things.

Figure 4.6 shows the frequency response curves for the open-loop transfer function of the benchmark PLL design with CPG values of 0.1 mA, 0.6 mA and 3.1 mA.

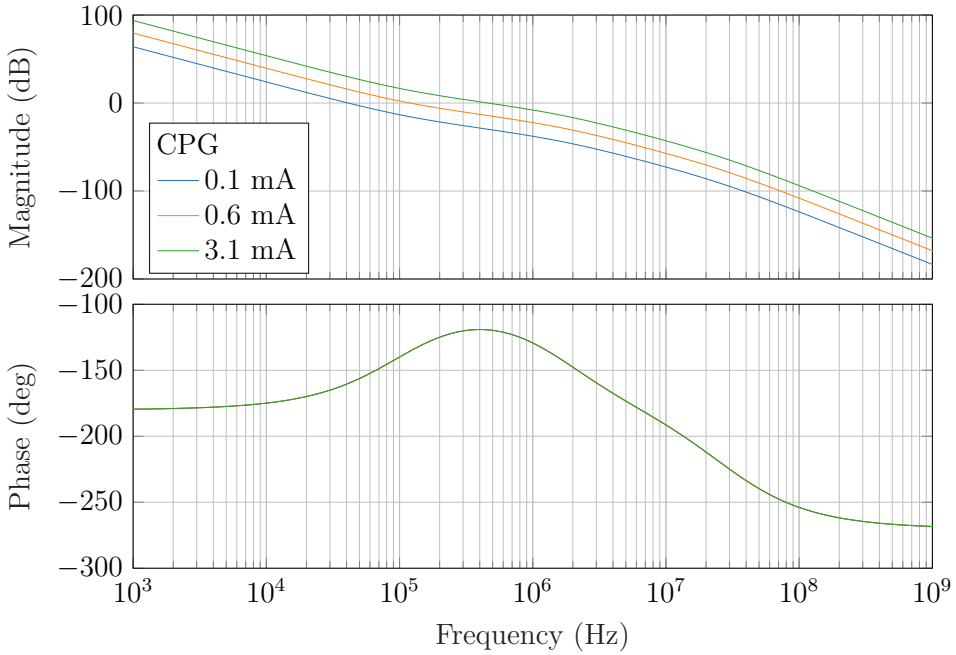


**Figure 4.6:** Open-loop frequency response for benchmark design with varying CPG values.

Markedly, the open-loop transfer function is a low pass function and, from its relationship with the VCO output transfer function, the latter can be inferred to also be low passing.

By the Bode criterion of stability, the closed-loop PLL is stable if the open-loop phase lag at the gain crossover frequency is less than 180° i.e.

$$\angle G(j\omega_{gc}) > -\pi \ , \tag{4.12}$$

provided that the amplitude crosses 0 dB at only one frequency, and the open-loop transfer function $G(s)$ is stable (i.e. does not have poles in the right-half plane) [50].

Applying this to the plotted frequency response curves, it can be ascertained that the benchmark design is stable for CPG values within the range of programmable values. However, any design change that can influence the shape of the frequency response needs

to be preceded by a study of the Bode plot as it can result in violation of the stability criterion.

Gain and phase margins can also be used to quantify the stability and are defined, respectively, as [51]

$$\text{GM} = -20 \log |G(j\omega_\pi)|, \text{ and} \tag{4.13}$$

$$\text{PM} = \angle G(j\omega_{gc}) + \pi \tag{4.14}$$

### 4.3.2 Closed-Loop Frequency Response

As specified earlier, there are several closed-loop transfer functions used to describe the system. The PLL transfer function function $Z_{\phi_{\text{PLL}}}(s)$ and the error function $Z_{\phi_e}$ are of interest.

For the benchmark system, with varying CPG values, the Bode plots for the stated transfer functions are shown in Figures 4.7 and 4.8.

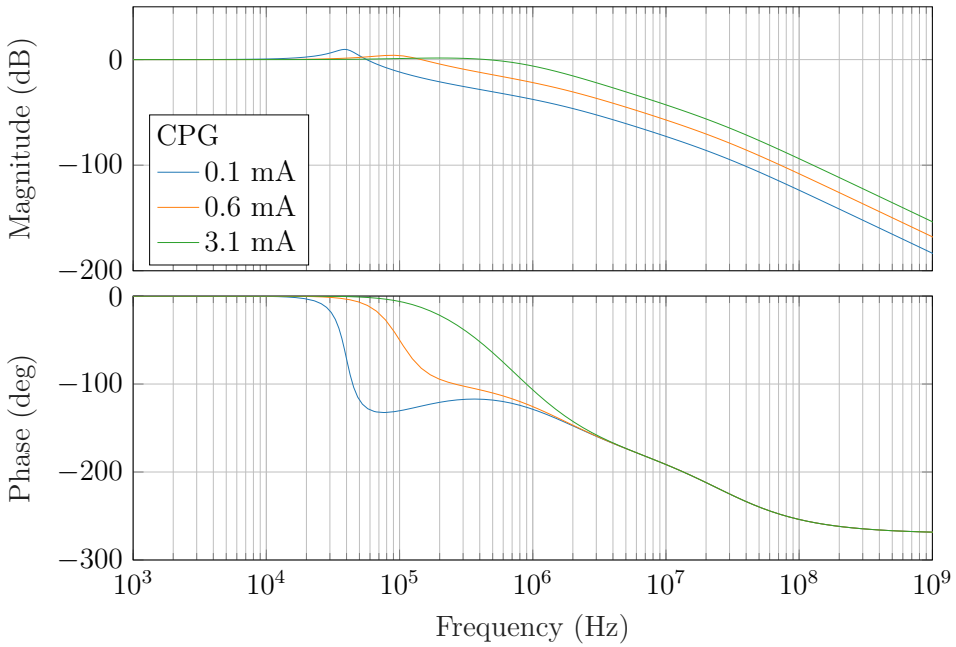


**Figure 4.7:** PLL transfer function frequency response for benchmark design with varying CPG values.

As discussed, the PLL performs a low-pass filtering function on input modulations, with a restricted bandwidth within which it tracks input phase modulation and outside of which it attenuates the modulation. The error function, on the other hand, performs a high-pass filtering operation on the phase error between the reference and the output.

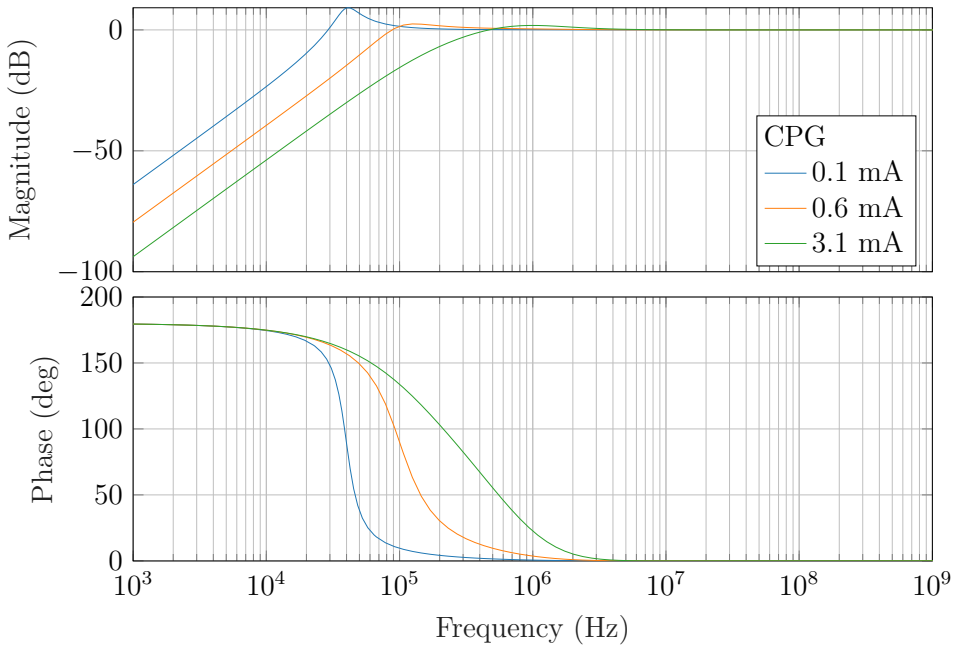


**Figure 4.8:** Error function frequency response for benchmark design with varying CPG values

It is also worth pointing out that for lower CPG values e.g. when a CPG value of 0.1 mA is used, the closed-loop frequency response has an 'upward kink', known as the resonant peak and caused by the zero in the system transfer function. This will be seen to appear in the spectra of the PLL output signals.

### 4.3.3 Phase-Locked Loop Bandwidth

Possibilities for defining the bandwidth of the PLL have been discussed in literature and, by far, the most widely adopted is the *loop bandwidth*, $B_L$, which is the open-loop gain crossover frequency $f_{gc}$ [52].

In filter design, one is typically also interested in the 3 dB bandwidth, $B_{3\text{dB}}$, of the filter which is the frequency at which the closed-loop gain drops by 3 dB. The 3 dB bandwidth of the PLL differs from the so-called loop bandwidth in that the loop bandwidth is computed from the open-loop transfer function, $G_o(s)$, whereas the 3 dB bandwidth is the 3 dB cutoff of the low-pass filtering function, $Z_{\text{PLL}}$, of the closed-loop PLL.

For both cases, an increase in loop gain, $K$, which is related to CPG as shown in Equation 4.10, results in a wider bandwidth.

Table 4.2 summarises the relationship between the values of loop bandwidth, 3 dB bandwidth and CPG for the CPG values whose frequency responses were computed.

**Table 4.2:** Relationship between the values of loop bandwidth, 3 dB bandwidth and CPG for CPG = 0.1 mA, 0.6 mA and 3.1 mA.

| **CPG** | **Loop Bandwidth ($B_L$)** | **3 dB Bandwidth ($B_{3\text{dB}}$) (Hz)** |
|---|---|---|
| 0.1 mA | 26.201 kHz | 1.309 MHz |
| 0.6 mA | 73.568 kHz | 5.863 MHz |
| 3.1 mA | 302.000 kHz | 8.976 MHz |

## 4.4 Dynamic Response

Design, analysis and characterisation of the PLL in terms of its time domain behaviour is an imperative counterpart to the preceding work on the frequency response.

Several aspects such as input tracking ability, lock and pull-in processes, maximum chirp rate and ramp linearity among others are considered in this section. These are studied in the context of the transient response of the PLL[5] to frequency step and frequency ramp input signals and this exercise facilitates the direct design of the FMCW waveforms to be used by the system.

### 4.4.1 Frequency Step Response

Although the phase step response can also be computed in simulation, it is neither useful in the current work nor possible to obtain practically; hence, the first response evaluated here is the step response.

A frequency step input has an angular velocity given by

$$\omega_i(t) = \omega'_{fr} + \Delta\omega_i u(t) \tag{4.15}$$

where $\Delta\omega_i$ is the change of the input's angular velocity and $u(t)$ is the unit step function.

By the relationship

$$\phi_i(t) = \Delta\omega_i t, \tag{4.16}$$

this is equivalent to a phase ramp input which, in the Laplace domain and in terms of the PLL's output angular frequency, gives

$$\Phi_i(s) = \frac{\Delta\omega_o}{Ns^2} \tag{4.17}$$

[5]Its short-term reaction.

In exploring the system's step response, two scenarios are of interest: response to a small frequency excursion such that the PLL operates in the region of linearity as well as response to a large frequency step.

Determining the system's response to a small frequency change allows for validation of the transfer function model. The model's response was simulated by multiplying the phase ramp input of Equation 4.17, for a frequency change of 8 MHz[6], with the VCO tuning voltage transfer function, $Z_{V_{tune}}$. This frequency step was also applied to the real system and Figure 4.9 shows a comparison between the modelled and real transient response for varying CPG.

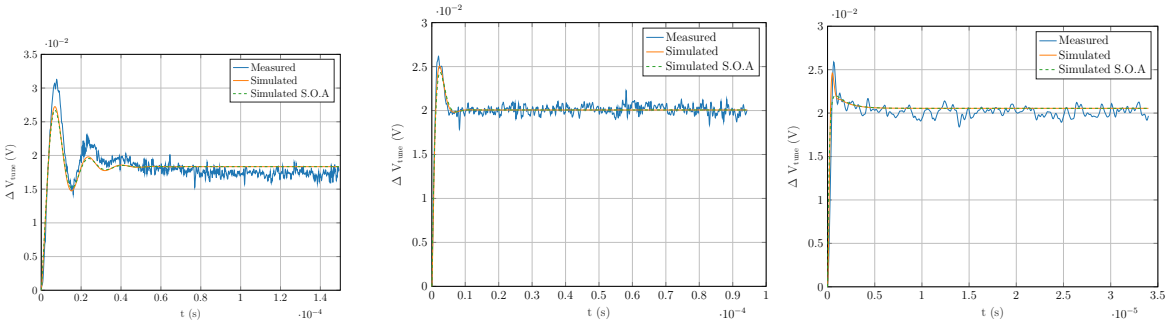


**(a)** **(b)** **(c)**

**Figure 4.9:** Step response for $\Delta f_o = 8.5276$ MHz for CPG values (a) 0.1 mA (b) 0.6 mA and (c) 3.1 mA. Simulated S.O.A stands for simulated second order approximation.

As can be seen, there is strong agreement between the simulated and experimental transient responses although the second order approximation is inaccurate in the peak value, particularly for CPG = 3.1 mA which is expected as it is merely an approximation based on the two most dominant poles in the transfer function.

Given that loop bandwidth is directly proportional to CPG, it can be seen, from the transient response, that settling time is significantly impacted by the loop bandwidth where, the wider the bandwidth, the faster the loop settles to the final value.

Additionally, for a narrower loop bandwidths, it can be observed that the system has more oscillatory behaviour.

A final observation is that the transient response curve overshoots before settling at the final value. This is an expected characteristic of transient responses of systems of second

[6]Admittedly, the frequency step does result in the phase error exceeding the limit for validity of the model but there are no observable non-linear effects in the measured result. This step size was chosen as it was the smallest change that the SNR of the oscilloscope allowed to be seen.

order and above and the percentage overshoot is given by [53]

$$\% \text{ overshoot} = \exp\left(\frac{-\zeta\pi}{\sqrt{1-\zeta^2}}\right) \tag{4.18}$$

which shows that as damping ratio increases, the percentage overshoot decreases.

It is noted, however, that calibration of the model is required for the loop gain $K$ and the nominal values can result in intolerably large modelling errors. For the test results documented above, the model is calibrated to have an average VCO sensitivity of 425 MHz/V which is significantly higher than the nominal 200 MHz/V specified the datasheet.

In addition to the small input response, the response of the physical system to large frequency changes was observed. Such an input would be used in implementation of sawtooth waveforms whereby the frequency is allowed to drop drastically in a very short period of time. Figure 4.10 shows the results of the pull-in process for a frequency change of 700 MHz (without the VCO divider).

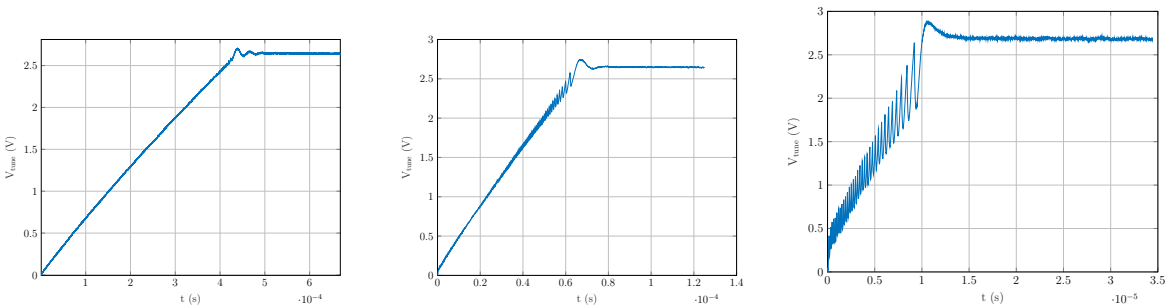


**(a)** **(b)** **(c)**

**Figure 4.10:** Step response for $\Delta f_o = 700$ MHz for CPG values (a) 0.1 mA (b) 0.6 mA and (c) 3.1 mA.

Since this frequency jump is beyond the validity space of the transfer function model, simulations were not carried out for this case.

The pull-in time is modelled to be given by [44]

$$T_{pull\text{-}in} \approx \Delta\omega_o \frac{NC_1}{K_{\text{PD}} K_{\text{VCO}} \pi} \tag{4.19}$$

The key observation in the response to large frequency excursions are the cycle-slips and a lower gradient of ascend which deviates from the exponential shape when the system is behaving as a linear system. The cycle-slips, as has been discussed, are attributed to the PFD missing some clock edges and, therefore, applying incorrect correction pulses.

Again, with a larger CPG, the loop responds much faster and has a faster pull-in process.

### 4.4.2 Frequency Ramp Response

Linear modulation of the PLL's output frequency is most relevant to the current study. Since it is constantly varying, there is not a characteristic transient response curve that can be given for the system; however, the are critical aspects to investigate and design constraints that require extraction.

The LFM input is defined as

$$\Delta\omega_i(t) = \omega_0' + \Delta\dot{\omega}t \tag{4.20}$$

which, when expressed as a phase input is

$$\phi_i(t) = \Delta\dot{\omega}\frac{t^2}{2} \tag{4.21}$$

and in the Laplace domain becomes

$$\Phi_i(s) = \frac{\Delta\dot{\omega}}{s^3} \tag{4.22}$$

Using the final value theorem (FVT), the phase error for a linearly varying frequency input tends to a finite value given by

$$\phi_e(\infty) = \lim_{s\to 0} sZ_{\phi_e} = \frac{a_0 N}{K_{\text{VCO}}K_{\text{PD}}}\frac{\Delta\dot{\omega}_o}{N} \tag{4.23}$$

This shows, as is known in Control theory, that the Type-II PLL is expected to track the frequency ramp with the given, finite steady state error.

To remain locked, for a PFD, the steady-state phase error must not exceed $2\pi$ [44], [50], [54]; therefore, substituting $\phi_e(\infty) = 2\pi$, allows for the extraction of the maximum rate of change of the frequency without causing a loss of lock.

$$\dot{\omega}_{o_{max}} = 2\pi\frac{K_{\text{VCO}}K_{\text{PD}}}{a_0} \quad \text{[rad/s/s]} \tag{4.24}$$

Additionally, if one is to vary the frequency input, the PLL slew rate will need to be able to support the maximum rate of change of frequency. Akin to operational amplifier slew

rate, in PLL design, PLL slew rate is defined as [45], [55]

$$\frac{df}{dt} = \frac{K_{\text{VCO}} K_{\text{PD}}}{a_0} \quad \text{[Hz/s]} \tag{4.25}$$

Incidentally, the two constraints obtained for maximum rate of change of input frequency and maximum slew rate are identical.

## 4.5 Waveform Design Considerations

An FMCW waveform is a sequence of frequency modulated segments and is defined by a set of key parameters namely, sweep rate, $k_r$; modulation period, $T_r$; modulation bandwidth, $B_r$, and pulse repetition frequency, PRF.

These parameters influence the SAR image quality and the basis of the waveform design problem is bringing together all the parameters and managing conflicting requirements such that optimal performance is achieved.

### 4.5.1 Range and Frequency Resolutions

Range resolution has been has shown to be inversely proportional to the effective modulation bandwidth and given by

$$\delta r = \frac{c\kappa_r}{2B_r} \tag{4.26}$$

where $\kappa_r$ is the $\text{IPR}_r$ broadening factor due to the windowing function.

The LMX2492EVM synthesisers, with a divide-by-4 factor on the output, achieve bandwidths of 175 MHz with a passive loop filter and 475 MHz with an active loop filter which evaluates to range resolutions of 0.857 m and 0.316 m respectively.

The process of pulse compression, introduces an additional complexity to the range resolution relationship because, owing to the properties of the Fourier transform, the frequency bins generated by the FFT limit the size of the represented range bins, $\delta R$, to

$$\delta R = \frac{c}{2k_r} \cdot \frac{f_s}{N} \tag{4.27}$$

where $N$ is the number of samples in each processed pulse.

While sinc interpolation (i.e. zero-padding the data before performing an FFT in order to increase $N$) improves the frequency resolution, it merely allows for a smoother looking spectrum and does not add any extra spectral information as increasing the number of samples by collecting more data would. Granularity of the spectrum can, therefore, be limiting factor regardless of having enough bandwidth to resolve two targets.

Sampling requirements are dictated by the IF spectrum bandwidth of interest which is related to the maximum range to be measured by

$$B_{\text{IF}} = f_{b_{max}} - f_{b_{min}} = \frac{2k_r}{c}(R_{max} - R_{min}) = \frac{2k_r}{c}\Delta R \tag{4.28}$$

which means that maximum unambiguous range, by the Nyquist criterion[7], is given by

$$R_u = \frac{f_s c}{2k_r} \tag{4.29}$$

This is in contrast to pulsed systems where maximum unambiguous range is dictated by the pulse repetition interval (PRI).

### 4.5.2 Pulse Repetition Frequency

Pulse repetition frequency (PRF) is the rate of repetition of a sequence of frequency modulated segments which form the pulse.

This is related to the pulse repetition interval (PRI) by

$$\text{PRI} = \frac{1}{\text{PRF}} \tag{4.30}$$

In practice, some portions of the pulse are typically not used in processing for a variety of reasons. This gives rise to the concept of effective pulse repetition frequency, $\text{PRF}_e$ which is the rate of repetition of the useful portion of the pulse, taking into account any processing techniques that also affect the PRF such as pre-summing.

The significance of the PRF is that, moving radars induce a spread in Doppler bandwidth of stationary objects in the beam and the Doppler frequency shifts are sampled at a rate (slow-time sampling rate) of the PRF which means that Doppler ambiguities (aliasing) will occur if the PRF is too low.

[7]For complex sampling

By the Nyquist sampling criterion, the PRF must be greater than or equal to the Doppler bandwidth where the Doppler bandwidth is given by [41]

$$B_D = \frac{4v}{\lambda} \sin\left(\frac{\theta_a}{2}\right) \sin\psi \tag{4.31}$$

and $v$ is the platform velocity, $\lambda$ is the pulse's wavelength, $\theta_a$ is the antenna pattern beamwidth and $\psi$ is the squint angle between the antenna's boresight and the platform velocity vector (which in the context of sidelooking stripmap SAR is 90°).

Table 4.3 gives the values of these parameters for the miloSAR. Additionally, the PRF is restricted to factors of the STEMlab ADC clock frequency since the timing control unit counts at this frequency.

**Table 4.3:** miloSAR Parameters for Evaluation of PRF Constraint.

| **Parameter** | **Symbol** | **Value** |
|---|---|---|
| Wavelength (worst case) | $\lambda$ | $118.730 \times 10^{-3}$ |
| Antenna azimuth beamwidth | $\theta_{az}$ | $\sim 70.517°$ |
| Squint angle of boresight from velocity | $\psi$ | 90° |

In addition to the duty factor, other factors that impact the PRF in the miloSAR are as follows:

- **Fully polarimetric operation:** When the radar is operating in a fully polarimetric mode, it alternately transmits in vertical and horizontal polarisations. This has the overall effect of scaling the PRF by a factor of 0.5.
- **Pre-summing:** Coherently summing consecutive profiles together during acquisition may be done to reduce data rate requirements. This has the effect of scaling the PRF by a factor of 1/PF where PF is presumming factor, which is the number of consecutive pulses summed together.

The effective PRF for the miloSAR is, therefore, given by

$$\mathrm{PRF}_e = \begin{cases} \frac{\mathrm{PRF}}{\mathrm{PF}} D, & \text{single transmit polarisation mode} \\ \frac{\mathrm{PRF}}{2\mathrm{PF}} D, & \text{fully-polarimetric mode} \end{cases}, \tag{4.32}$$

where $D$ is the duty factor.

Table 4.4 shows the velocities of prospective aircraft to be used for the SAR system and the PRF values to avoid Doppler aliasing.

**Table 4.4:** Prospective aircraft velocities and PRF requirements.

| Aircraft | Type | Speed (m/s)[8] | Single Pol PRF | Fully Pol PRF |
|---|---|---|---|---|
| Ikarus C42 | Fixed wing light aircraft | 38.889 [56] | 751.478 | 1502.957 |
| Cessna 702 | Fixed wing light aircraft | 61.733 [57] | 1192.911 | 2385.822 |
| DJI Matrice | Commercial drone | 23 [58] | 444.446 | 888.891 |

### 4.5.3 Waveform Type

There are innumerable permutations for combining ramp segments to generate a pulse. The most basic ones which are sawtooth and triangular waveforms are discussed here.

The sawtooth waveform uses a single ramp whose frequency wraps back to the initial frequency at the end of the modulation period. Ideally, this frequency decrement would be instantaneous; however, in practice, the PLL requires non-zero time, as will be discussed in the subsequent sections. The sawtooth waveform is an efficient use of the signal as only a very small portion of the ramp is discarded, thereby achieving either better CPI or FFT resolution.

A triangular waveform is a combination of two ramps with varying sweep directions where one increments the frequency and the other decrements it. The waveform can be symmetric, which means that the upramp and downramp portions have equal modulation periods and bandwidths, or asymmetric, which means that the upramp and downramp portions have unequal modulation periods. Both upramp and downramp data can be processed and must be, in applications such as ground moving target indication (GMTI). However, in the miloSAR the downramp data is discarded which makes sawtooth waveforms a more apt solution.

## 4.6 Summary

The PLL used for frequency synthesis as well as the generated waveforms for the miloSAR have been investigated in the present chapter.

The architecture of the LMX2492EVM PLL was explored and its attributes discussed. This allowed for the derivation of a phase domain model of the synthesiser for the linear region defined by phase errors within the range of $-2\pi$ and $2\pi$.

From this, frequency response analysis was performed and it was observed that the overall

PLL transfer function is that of a LPF whose bandwidth varies with the CPG, VCO sensitivity and loop filter component values.

Following the frequency response analysis, the dynamic response analysis was performed. It was observed that the PLL tracks a scaled replica of the reference input and by modulating the N-divider value, an FMCW waveform can be generated.

The maximum chirp rate constraint was formulated and the pull-in process was demonstrated, both of which are essential for the implementation of sawtooth waveforms as required by RO2.

Considerations for practical implementation of FMCW waveforms were also presented and it was determined that range and frequency resolutions, PRF and the waveform type are all critical elements of the waveform design.

# Chapter 5

# Phase and Frequency Stability

The common simplification in FMCW theory, stating that range of a point target corresponds to a single frequency bin in the IF spectrum, is an idealisation that does not hold true in practice.

In reality, there are deviations from the chirp represented by Equation A.1 which can cause devastating problems for radar systems.

This chapter considers the primary sources of frequency instability in FMCW radar, namely ramp non-linearity, spurs and phase noise.

Ramp non-linearity is deemed to be less of a concern as the PLL achieves sufficiently linear ramps through careful design, and the effects of spurs were thoroughly studied in [2]. Therefore, the main focus of the current chapter is on phase noise, although the former two concepts are briefly reviewed.

## 5.1 Ramp Quantisation and Non-linearity

FMCW radar makes the assumption that the transmitted ramp is perfectly linear and any such uncompensated non-linearities affect range and velocity resolution of range-Doppler radars.

Ramp linearity is quantified as [59]

$$L = \frac{3\sigma_{rms}}{\mathrm{CF} \cdot B_r} \tag{5.1}$$

where $\sigma_{rms}$ is standard deviation of the output frequency relative to that in the ideal ramp and CF is the chop factor (i.e. the fraction of the ramp used in processing).

To achieve optimal ramp linearity when using a PLL-based synthesiser, the PLL must be able to settle quickly enough that it can track the frequency modulation. This is best achieved by increasing the loop bandwidth such that it is appreciably larger than the modulation frequency. However, the PLL must not be too fast such that it settles at a particular frequency, which would result in a staircase output. This implies that the loop bandwidth must be below the stepping rate of the N-divider.

Figure 5.1 illustrates both scenarios as well as the ideal case.

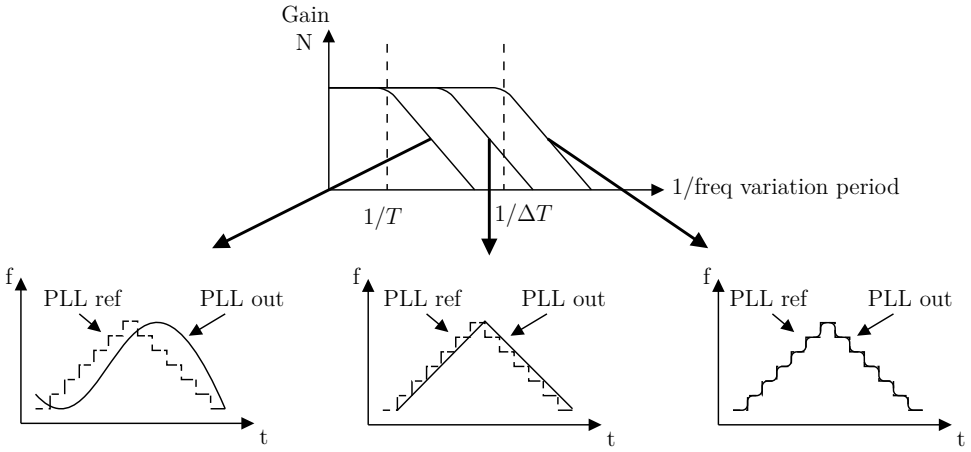


**Figure 5.1:** PLL reference modulation tracking for different loop bandwidth limits [18].

To avoid distortion, the optimum loop bandwidth is within the range [60]

$$\frac{1}{T_r} \ll B_L < \frac{2^{lin} - 1}{T_r/2} \tag{5.2}$$

where $2^{lin}$ is the number of quantisation levels of the modulation signal.

For the current benchmark system, using parameters defined in Chapter 6, the loop bandwidth is always within this range making ramp non-linearity not a concern in the current study.

## 5.2 Spurs

Spurious tones, succinctly referred to as 'spurs', are a phenomenon which results in spectral contamination of the frequency synthesiser's output and degrades performance of SAR systems as the spurious signals erroneously indicate target energy in incorrect range bins.

There are several sources and mechanisms to which they can be attributed, but all fall under either direct spurs or modulated spurs categories.

Direct spurs are the result of an additive frequency component on the VCO output such that, the instantaneous synthesiser output (before the VCO divider, if included) is given by

$$x_{\mathrm{PLL}}(t) = A\sin(2\pi f_{\mathrm{VCO}}t) + B\sin(2\pi f_{spur}t) \tag{5.3}$$

As such, only a single peak, corresponding to the spur frequency, appears in the spectrum of the output signal.

Some of the most common types of direct spurs are external cross-talk to the PLL from such things as the power supply; spurs due to Delta-Sigma modulators; and harmonics from components of the PLL.

Contrastingly, modulated spurs are the result of modulation of the VCO output signal which is formulated as

$$x_{\mathrm{PLL}}(t) = A \cdot B\sin(2\pi f_{\mathrm{VCO}}t) \cdot \sin(2\pi f_{spur}t) \tag{5.4}$$

$$= \frac{A \cdot B}{2}\sin(2\pi(f_{\mathrm{VCO}} - f_{spur})t) - \frac{A \cdot B}{2}\sin(2\pi(f_{\mathrm{VCO}} + f_{spur})t) \tag{5.5}$$

These spurs, therefore, appear at equal offsets from and either side of the carrier.

Three main types of modulated spurs to be concerned with in PLL design are reference spurs, fractional spurs and cross talk spurs.

Fractional spurs are a challenge in the miloSAR, arising from the use of an N-divider to achieve narrow frequency tuning resolutions. These can be further classified as integer boundary spurs (IBS), primary fractional spurs (PFS) and sub-fractional spurs (SFS) occurring at

$$f_{\mathrm{IBS}} = k[\mathrm{round}(N) - N] \cdot f_{\mathrm{PD}}, \quad k = \{1, 2, 3, ...\} \tag{5.6}$$

$$f_{\text{PFS}} = k\frac{f_{\text{PD}}}{F_{den}}, \quad k = \{1, 2, 3, ..., F_{den} - 1\} \tag{5.7}$$

and

$$f_{\text{SFS}} = k\frac{f_{\text{PD}}/F_{den}}{h}, \quad h \in \{2, 3, 4, 5, 12\}\ ;\ k = \{1, 2, 3, ...\} \tag{5.8}$$

respectively, where $F_{den}$ is the denominator of the fractional component of the N-divider factor $N$.

## 5.3 Phase Noise

Phase noise is the random deviation in the phase of a signal from the nominal and is an important field of study in radar and communications. It results in a spectral broadening such as that shown in Figure 1.1 which is known to be a major problem for systems that represent range and velocity as spectral components.

### 5.3.1 Mathematical Definition of Phase Noise

Phase noise is characterised by the power spectral density (PSD) of the signal's random phase fluctuations, $S_\phi(f)$, as follows:

$$S_\phi(f) = \phi^2_{rms}(f)\frac{1}{\text{BW}} \quad [\text{rad}^2/\text{Hz}] \tag{5.9}$$

where $f$ is the frequency offset from the carrier, $\phi_{rms}$ is an RMS value in a specific Fourier frequency band, and BW is the size of the band. Further details pertaining to $S_\phi(f)$ are given in Section 5.3.2.

More common in modern literature is the quantification of phase noise through $\mathcal{L}(f)$ referred to as "single sideband (SSB) phase noise"[61] which is defined as the ratio of power density in one phase noise modulation sideband (per Hz) to the total signal power and is related to $S_\phi(f)$ by [62]

$$\mathcal{L}(f) \equiv \frac{S_\phi(f)}{2} \tag{5.10}$$

$\mathcal{L}(f)$ is typically expressed as $10\log_{10}\mathcal{L}(f)$ with the units of decibels relative to the carrier in a 1 Hz bandwidth (dBc/Hz). This is depicted on a log-log plot of $\mathcal{L}(f)$ vs. frequency offset referred to as a phase noise profile.

It is also a widespread practice to refer to 'close-in', 'far-out' and 'mid-range' phase noise depending on the offset frequency. There is no strictly enforced definition of these regions and for the current work, close-in will imply offsets less that 1 kHz, far-out for offsets greater that 100 kHz and mid-range between the two limits.

To assess the impact of phase instability on performance of the system, metrics such as integrated phase noise (IPN), signal-to-noise ratio (SNR), root mean square (RMS) phase error, phase jitter, and error vector magnitude, (EVM) among others, are used.

IPN is defined as [45], [62]

$$\int_{f_1}^{f_2} S_\phi(f)\ df \tag{5.11}$$

and is related to SNR by

$$\text{SNR} = \frac{1}{\text{IPN}} \tag{5.12}$$

and to RMS phase error by

$$\sigma_v = \sqrt{\text{IPN}} \quad \text{[rad]} \tag{5.13}$$

which is often, also, expressed in time units as phase jitter given by [52]

$$\phi_{jitter} = \frac{1}{f_c} \cdot \frac{\sigma_v}{2\pi} \tag{5.14}$$

Unless otherwise stated, the above outlined framework for phase noise analysis is adopted for the current work.

### 5.3.2 Spectral Analysis of Phase Noise

From its definition, phase noise requires use of the PSD for its analysis because the future variation of the noise cannot be determined exactly; therefore, only probabilistic statements about the variation can be made.

This section discusses the spectral analysis techniques used in this work for phase noise analysis and addresses how the PSD estimation problem was resolved.

**PSD Estimation Problem**

The PSD of a signal $x_T(t)$ is obtained via Parseval's theorem and is given by [63] [1]

$$S_x(f) = \lim_{T\to\infty} \frac{1}{T}|E\{X_T(f)\}|^2 \tag{5.15}$$

where $X_T(f)$ is the Fourier transform of $x_T(t)$.

In the case where the noise process is a wide-sense stationary (WSS) stochastic process, the Wiener-Khinchin theorem [64] applies, which is derived from Equation 5.15 and states that the PSD of the signal is given by the Fourier transform of its autocorrelation function (ACF) i.e.

$$S_x(f) \triangleq \int_{-\infty}^{\infty} R(\tau)e^{-j2\pi f\tau}d\tau \tag{5.16}$$

The autocorrelation of any given stochastic process is defined as

$$R(t_1, t_2) \triangleq E\{x(t_1)x(t_2)\} \tag{5.17}$$

$$= \int_{-\infty}^{\infty}\int_{-\infty}^{\infty} x_1x_2f(x_1, x_2; t_1, t_2)\, dx_1\, dx_2. \tag{5.18}$$

and for WSS processes, the first and second order properties are independent of time such that $R(t_1, t_2)$ only depends on $t_2 - t_1$ and not on individual values of $t_1$ and $t_2$. Setting $t_1 = t$ and $t_2 = t + \tau$, this means $t_2 - t_1 = \tau$ which gives $R(t_1, t_2) = R(t_1 - t_2)$; thus, the autocorrelation function is simplified to

$$R(\tau) = E\{x(t + \tau)x(t)\} \tag{5.19}$$

with $R(0)$ being the variance of the process.

For a non-WSS process, however, the ACF does not exist and a closed-form expression for the PSD cannot be obtained. This is of concern in the current work because the phase noise of PLLs is non-stationary [46], [65]. Two of the most dominant phase noise sources in the PLL — the reference oscillator and the VCO — have power law $(1/f^\alpha)$ phase noises and a primary characteristic of power law noises is the non-integrability of the spectral density for some values of $\alpha$ ($\alpha \geq 1$) implying non-stationarity of the underlying process [65]. This means that the exact PSD cannot be determined by means of the Wiener-Khinchin approach and there exists a spectral estimation problem of determining

[1] The expectation operator is used to denote that this is an ensemble averaged power since random variables are being dealt with.

an estimate $\hat{S}_x(f)$ of the PSD, $S_x(f)$.

Several approaches for spectral estimation have been presented in statistical theory literature and the reader is redirected to such writings for more details. In this study, two methods of spectral analysis are used namely, Welch's Overlapped Segmented Average (WOSA) technique for spectral estimation of sampled data and through spectrum and phase noise analysers.

### Welch's Overlapped Segmented Average Method for PSD Estimation

Welch's Overlapped Segmented Average Method for PSD estimation, simply referred to as the Welch method [66] is one of the most common approaches to determine the PSD estimate for a given finite length record $\{x(1), ..., x(N)\}$ and is an augmentation of the Bartlett Method [67]. For its simplicity and relative accuracy, this is what will be used in this work to determine the PSD of all discrete time data.

In order to use the Welch estimator, the data is first partitioned into segments. The $i$th data segment of the record $x(t)$ is given by

$$x_i(t) = x((i-1)K + t), \quad t = \{1, ..., M\};\ i = \{1, ..., S\} \tag{5.20}$$

where $(i-1)K$ is the first index for the $j$th sequence of observations.

If $K = M$, the sequences do not overlap but are contiguous and the sample splitting used by the Bartlett method is obtained. Typically, the recommended value of $K$ for the Welch method is $K = M/2$ such that there are $S \approx 2M/N$ data segments with 50% overlap between consecutive segments. However, the pulsed nature of the FMCW waveform makes it such that there are discontinuities in recorded signal which would result in corruption of the spectrum.

A more natural way of segmenting the data is to consider data recorded for each pulse as a segment and processing with 0% overlap.

The windowed periodogram for $x_i(t)$ is then computed as

$$\hat{S}_{x_i}(f) = \frac{1}{M \cdot P} \left| \sum_{t=1}^{M} w(t) x_i(t) e^{-j2\pi ft} \right|^2 \tag{5.21}$$

where $w(t)$ is the window function, and $P$ is the 'power' of the window given by

$$P = \frac{1}{M} \sum_{t=1}^{M} |w(t)|^2 \tag{5.22}$$

As such, the Welch estimator can be computed by employing the FFT.

Finally, the Welch estimate of the PSD is then obtained by averaging the windowed periodograms for all the segments i.e.

$$\hat{S}_{x_W}(f) = \frac{1}{S} \sum_{j=1}^{S} \hat{S}_{x_i}(f) \tag{5.23}$$

This can then be used, as is discussed in the following section, to produce a phase noise profile.

#### Phase Noise Measurement Approaches

There are three primary approaches typically used to measure phase noise each with its merits and shortcomings namely, direct spectrum (using a spectrum/ signal analyser), phase detector method and two-channel cross-correlation methods where the first measures phase noise in the presence of the carrier and latter two demodulate the signal, removing the carrier before measurement [61].

The direct spectrum technique entails processing the PSD of a given signal, and is the only method considered in this work.

To obtain the phase noise profile from the spectral data, the carrier signal power is first subtracted from all the measured values of signal power in order to obtain a result that is measured relative to the carrier. The measured noise power is then normalised to a 1 Hz bandwidth by subtracting $10 \log_{10}(\text{RBW})$ and finally, the normalised, ratiometric power is plotted against frequency offset from the carrier on a log-log plot.

### 5.3.3 Phase Noise in Delta-Sigma PLLs

Phase noise in the PLL output constitutes contributions of the reference clock, VCO and all other circuit elements in the loop.

These sources can be classified either as in-band or out-band mechanisms on account of

the effect of the feedback loop on their phase noise.

In the case of in-band mechanisms, the phase noise spectrum is filtered by the low-pass system transfer function i.e. [44]

$$S_{\phi_{out}}(f) = S_{\phi_{in\text{-}band}}(f) \cdot |Z_{\mathrm{PLL}}(f)|^2 \tag{5.24}$$

Within the passband, defined by $B_{3\mathrm{dB}}$, gain is approximately 1 and in the stopband, the phase noise is attenuated at a roll-off rate dependent on the transfer function.

For out-band mechanisms, phase noise is filtered by the high pass error transfer function i.e.

$$S_{\phi_{out}}(f) = S_{\phi_{out\text{-}band}}(f) \cdot |Z_e(f)|^2 \tag{5.25}$$

The two filtering responses are related as

$$Z_e(f) = 1 - Z_{\mathrm{PLL}}(f) \tag{5.26}$$

which creates conflicting objectives because, in order to suppress more in-band phase noise, one would need a narrower loop bandwidth but this would, in turn, allow more out-band phase noise.

### Reference Input

Phase noise of free-running oscillators such as the reference oscillator is modelled as a combination of power law or $1/f^\alpha$ noises and the Lorentzian function, for close-to-carrier offsets.

The power law model represents the phase noise spectrum as a weighted sum of five independent noise processes [62], [65]

$$S_\phi(f) = \begin{cases} \sum_{\alpha=-4}^{0} h_\alpha f^\alpha & 0 < f < f_h, \\ 0 & f > f_h \end{cases} \tag{5.27}$$

where $h_\alpha$ is a constant and $f_h$ is the cutoff of an ideal brick-wall LPF.

The spectra of these noises grows with low frequency as $1/f^\alpha$ where $f$ is the cyclic frequency and $\alpha$ is a real number usually between 0 and 2.

The model is very accurate but, predicts an asymptotic behaviour of phase noise going off to infinity at a rate of $1/f^4$ as the offset from carrier approaches 0. To resolve this, the Lorentzian function [68], given by

$$\mathcal{L}(\Delta f) \propto \frac{a^2}{a^2 + (\Delta f)^2} \tag{5.28}$$

where $a$ is a fitting parameter, is used to express the phase noise in this region.

The reference clock generates in-band phase noise; therefore, it is low-pass filtered by the PLL as represented in Equation 5.24 and thus, dominates the close-in to mid-range phase noise regions.

### Input Path and N-Divider

Phase noise from elements within the input path and the N-divider can be collectively analyzed since they all contribute to the phase noise at the charge pump output and would eventually be filtered in the same manner by the PLL.

They are all in-band mechanisms and their aggregated phase noise can be modelled as $1/f$ and flat phase noise as [45]

$$\mathcal{L}_{flat} = \mathcal{L}_{1\text{ Hz}} + 10\log\left(\frac{f_{PD}}{1\text{ Hz}}\right) + 20\log(N) \tag{5.29}$$

and

$$\mathcal{L}_{1/f}(f_{out}, f) = \mathcal{L}_{10\text{ kHz}} + 20\log\left(\frac{f_{out}}{1\text{ GHz}}\right) - 10\log\left(\frac{f}{10\text{ kHz}}\right) \tag{5.30}$$

where $\mathcal{L}_{1\text{ Hz}}$ and $\mathcal{L}_{10\text{ kHz}}$ are figures of merit representing noise floors normalised to 1 Hz and 10 kHz respectively, discussed in greater detail in [45].

Equations 5.29 and 5.30 encapsulate the relationship of the phase noise to the PLL parameters such as the output frequency, phase detector frequency and N-divider value which are important for phase noise optimisation.

### Loop Filter

To begin with, consider the passive loop filter. Resistors in the RC filter contribute Johnson-Nyquist (thermal) noise which is as a result of the random motion of charged carriers in conducting media and which degrades the phase noise of the PLL.

It is well documented in literature that a real resistor can be modelled as a Thévenin equivalent circuit comprising a noiseless resistor in series with a voltage source having an RMS voltage over a given bandwidth of

$$v_R = \sqrt{4kTRB} \tag{5.31}$$

where

- $k$ is Boltzmann's constant ($1.380649 \times 10^{-23}$ J/K),
- $T$ is the resistor's absolute temperature in Kelvins (K),
- $R$ is the resistor value in ohms ($\Omega$),
- $B$ is the bandwidth over which the noise is measured in hertz (Hz) [2]

To determine the noise contribution of the resistor in the loop, it is necessary to derive transfer functions from the resistor noise voltage source to the VCO tuning voltage input node.

In the interest of conciseness of this document, the reader is pointed to [45] for the derivations. It suffices, here, to state that according to literature [45], [69] the phase noise due to a specific resistor $R_x$ in the passive loop filter, at a given offset $f$, can be modelled as

$$\mathrm{PN}_{R_x}(f) = 20 \log \frac{\beta(f)}{2} \tag{5.32}$$

where

$$\beta(f) = \frac{f_{dev}(f)}{f_{mod}(f)} = \frac{\sqrt{2} v_{R_x} K_{\mathrm{VCO}}}{f} \cdot \left| \left| \frac{T_{R_x(s)}}{1 + G(s)H(s)} \right| \right|_{s=2\pi jf} \tag{5.33}$$

Phase noise of the active loop filter is obtained in a similar manner and is also discussed in greater detail in [45].

### Voltage Controlled Oscillator

The VCO phase noise has the same model as that of the reference oscillator and the discussion presented on the reference oscillator applies. The key distinction between the two, however, is that the VCO is an out-band mechanism therefore VCO phase noise dominates outside the PLL bandwidth and is attenuated within it.

[2] Since phase noise is evaluated for a 1 Hz bandwidth, $B = 1Hz$.

**Delta-Sigma Modulator**

A critical concern for dual-PLL scheme, as will be shown in Chapter 6, is the phase noise created by the Delta-Sigma modulators [52], [70] which is at very high levels in the mid-range to far-out offsets as exemplified in Figure 5.2.

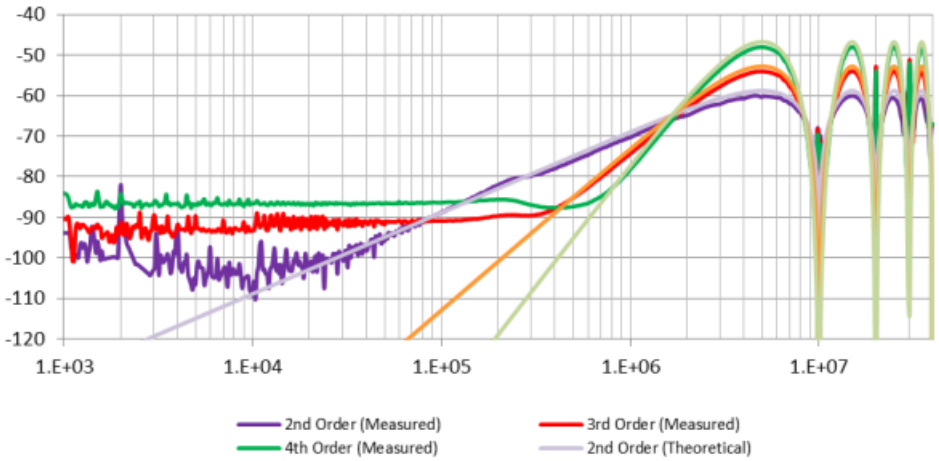


**Figure 5.2:** Delta-Sigma modulator noise for LMX2485 [45].

This noise is modelled as [45]

$$\mathcal{L}_{\Sigma\Delta}(f) = (2\pi)^2 \cdot \left(2\sin\left(\frac{\pi f}{f_{\text{PD}}}\right)\right)^{2(n-1)} \cdot \left|\left|\frac{Q_n(j2\pi f)}{f_{\text{PD}}}\right|\right| \tag{5.34}$$

where $n$ is the order of the Delta-Sigma modulator, and $Q_n(z)$ is the output of the $n^{\text{th}}$ quantiser minus its input.

If the loop bandwidth is sufficiently narrow, the 'Delta-Sigma characteristic bump' can be suppressed. However, when good tracking performance demands the use of a larger loop bandwidth, this bump causes severe performance degradation especially when range correlation filtering is not in effect due to separate PLLs being used.

### 5.3.4 Propagation of Phase Noise through System Signal Chain

In any well designed radar system, the main source of phase noise should be the synthesisers. This has been reviewed in the context of the Delta-Sigma PLL in the previous section. The current section discusses how the synthesiser phase noise propagates through the signal chain.

Of particular interest are the mixer and ADC which transform the phase noise to the IF and digital domains respectively.

### Mixer

As is shown in the analytical development of FMCW SAR in Appendix A, the mixing operation results in the combination of phase errors within the transmit and local oscillators to form the IF phase error. In the case of phase noise, this is termed residual phase noise [71] or differential phase noise [72], and is given by

$$\Delta\phi_n(t,\tau) = \phi_{n_{\mathrm{RX}}}(t-\tau) - \phi_{n_{\mathrm{LO}}}(t) \tag{5.35}$$

An important property of phase noise, exploited to achieve good performance in radar systems, is that the multiplication of two strongly correlated or coherent signals results in a reduction of their phase noise. This is known as range correlation filtering or phase noise decorrelation and is formulated as follows [71]–[74]:

$$\mathcal{L}_{\mathrm{IF}} = \mathcal{L}_{\mathrm{TX}}(f) \cdot 4\sin^2\left(\frac{\tau_d f}{2}\right) \tag{5.36}$$

It is important to note that the frequency offsets map directly from the transmit or local oscillator signal spectrum to the IF spectrum.

The term $4\sin^2\left(\frac{\tau_d f}{2}\right)$ is referred to, in literature, as the delay function [75] or the correlation factor and can be considered to be the squared magnitude of a filter with the transfer function

$$H_{cor}(f) = 2\sin\left(\frac{\tau_d f}{2}\right) \tag{5.37}$$

whose frequency response is plotted in Figure 5.3.

Notably, as the time delay $\tau$ approaches 0 s (i.e. target range approaches 0 m), and $\phi_n(t-\tau)$ and $\phi_n(t)$ converge statistically such that $\Delta\phi_{n_{IF}}$ approaches 0 with the converse being true for increasing time delay.

### ADC

An ADC can be considered to be a time-mixer [73]; therefore, Equation 5.36 applies for the ADC input and the ADC clock.

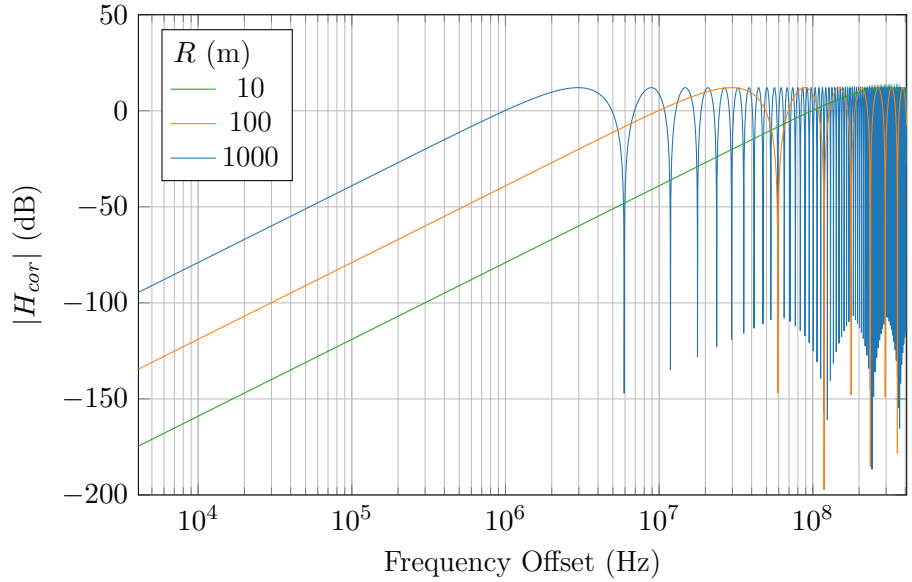


**Figure 5.3:** Phase noise range correlation filter frequency response magnitude for varying target range.

### 5.3.5 Simulation of Phase Noise in FMCW SAR

For the purposes of analysis and design, it is essential to simulate the FMCW SAR system with phase noise in the transmit and local oscillator signals which is in alignment with RO4.

Furthermore, simulated models for the random phase fluctuations will be used extensively in Chapter 6 to demonstrate the impact of phase noise in the miloSAR and to derive system phase noise requirements.

#### Discrete Phase Noise Sequence Simulation Approach

A widely accepted approach to modelling phase noise is as white Gaussian noise driving a linear system (or filter) [65]. The output of this filter is

$$\phi(t) = \int_0^t h(\tau)w(t-\tau)d\tau \tag{5.38}$$

where $h(t)$ is the causal impulse response of the noise shaping filter and $w(t)$ is white Gaussian noise.

The integration limits imply a causal, physically realisable system which, in the Laplace

domain, is represented by

$$\Phi(s) = H(s)W(s) \tag{5.39}$$

where $H(s)$ is the transfer function of the filter and $W(s)$ is the spectrum of the white Gaussian noise.

The filter is realised as a cascade of finite impulse response (FIR) filters or infinite impulse response (IIR) filters whose overall frequency responses give the desired phase noise mask.

### Simulation Setup

A simulation of the miloSAR using system and scene parameters shown in Tables 3.6, 5.2, 5.3 and 5.4 was carried out to observe how phase noise manifests in the SAR image and to derive phase noise requirements.

As will be shown in Chapter 6, the phase noise levels given in Table 5.4 are selected to be similar to those of the actual PLL.

**Table 5.2:** Simulated Scene Setup

| | $\boldsymbol{x}$ **(m)** | $\boldsymbol{y}$ **(m)** | $\boldsymbol{z}$ **(m)** | $\boldsymbol{\sigma(m^2)}$ |
|---|---|---|---|---|
| $S_1$ | 0 | 650 | 0 | 0.01 |

**Table 5.3:** miloSAR Simulation Acquisition Parameters

| **Parameter** | **Symbol** | **Value** |
|---|---|---|
| Platform Nominal Velocity | $v_0$ | 50 m/s |
| Platform Nominal Height | $h$ | 100 m |
| Flight Duration | | 3 s |

**Table 5.4:** Simulated Signal Phase Noise Levels.

| **Offset (Hz)** | $1 \times 10^3$ | $22 \times 10^3$ | $121 \times 10^3$ | $495 \times 10^3$ | $1.38 \times 10^6$ | $8.06 \times 10^6$ |
|---|---|---|---|---|---|---|
| $\mathcal{L}(f)$ **(dBc/Hz)** | -66.000 | -67.361 | -81.500 | -83.000 | -87.000 | -110.113 |

Figure 5.4 shows the frequency response of the FIR filter used for the phase noise mask in Table 5.4.

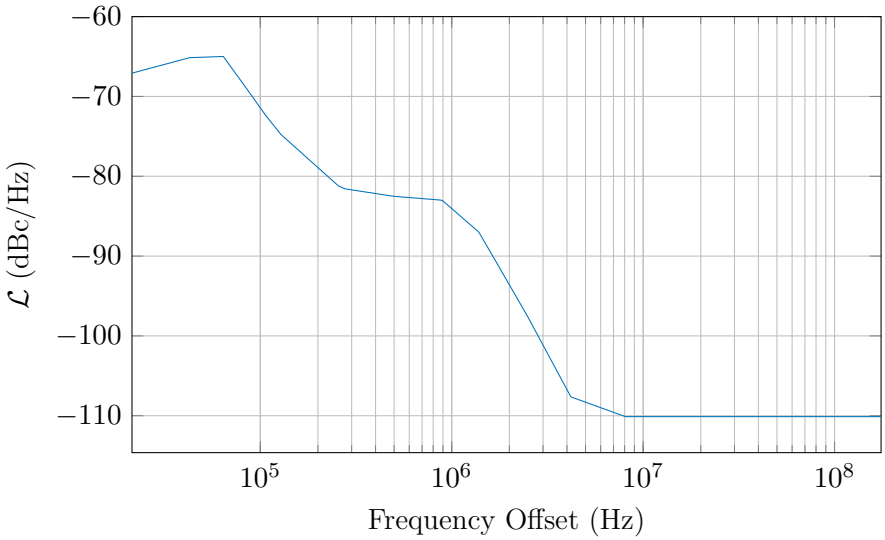


**Figure 5.4:** Phase noise mask FIR filter frequency response.

### Phase Noise in Impulse Response

First, the point target $S_1$ was simulated in isolation without phase noise, and then it was simulated again with the given phase noise configuration where the transmit and range reference signal phase noise was uncorrelated.

Figure 5.5 shows the reconstructed SAR images for the simulations.

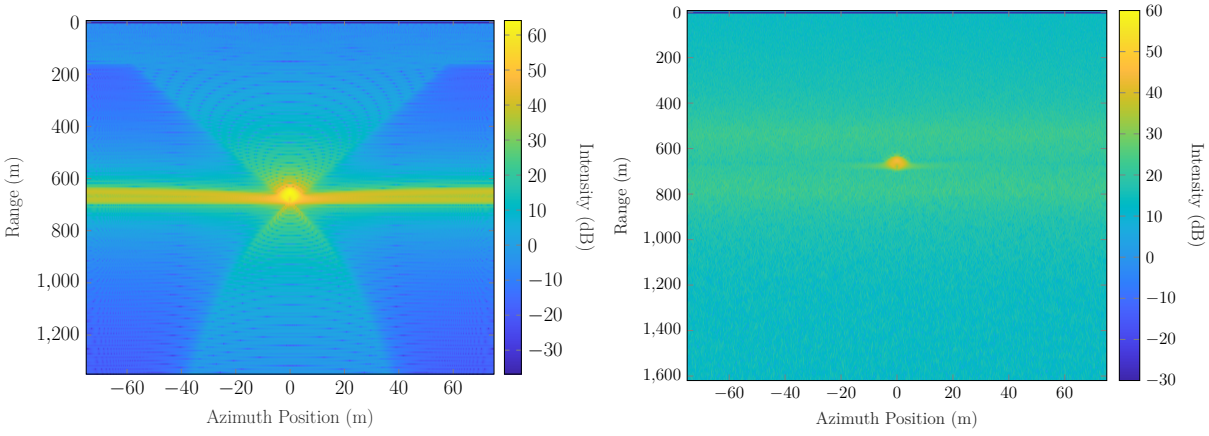


**Figure 5.5:** Simulated point target (a) without phase noise and (b) with phase noise.

The simulation matches expectations with the point target focused at the correct range and azimuth positions.

Evidently, phase noise in the target reflection results in additional energy attributed to the

target being distributed all throughout the image and with higher levels of the undesired energy closer to the target.

Figure 5.6 shows cuts through the center of the target in the range and azimuth dimensions.

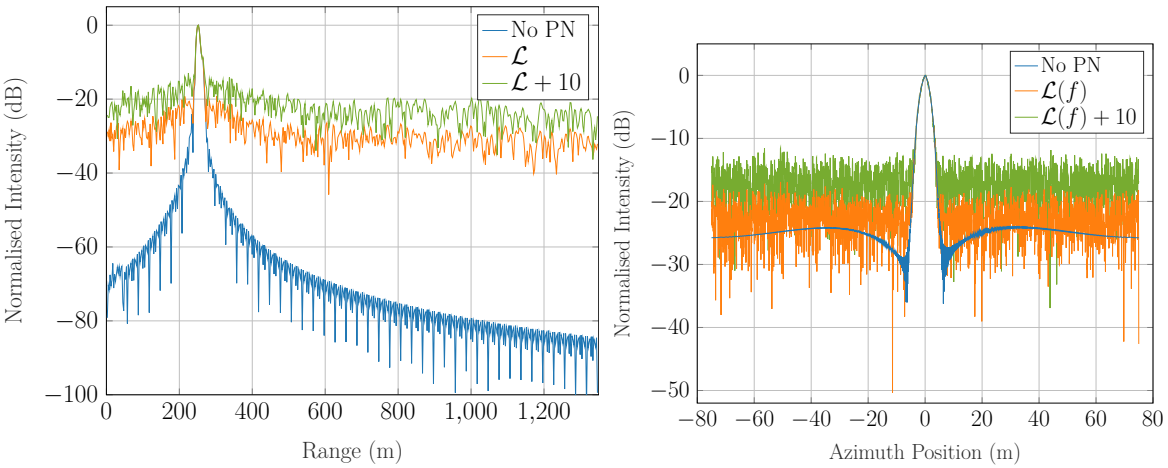


**(a)** **(b)**

**Figure 5.6:** Simulated (a) $\text{IPR}_r$ and (b) $\text{IPR}_a$ for $\text{S}_1$ with and without phase noise and processed using a Hanning range window.

This also depicts what is expected from theoretical knowledge with distinct peaks appearing in both $\text{IPR}_r$ and $\text{IPR}_a$ showing that SNR has been maximised through the matched filtering operations.

In the $\text{IPR}_r$ shown in Figure 5.6 (a), the characteristic pedestal phase noise skirt of PLLs can be observed surrounding the target and dictating the noise floor at farther out offsets as was predicted would be the case in Section 5.3.4.

It is also observed that a 10 dB increase in phase noise levels results in a 10 dB decrease in SNR in the SAR image; therefore, the manifestation of phase noise in the SAR image is quite predictable.

Figure 5.6(b) shows a similar result for $\text{IPR}_a$ which is that SNR of the target return reduces with increasing phase noise. The shape of $\text{IPR}_a$ is, however, not influenced by the phase noise mask shape and it simply appears as a constant level noise floor.

### Leakage Phase Noise

Although it is also as a direct result of impulse response broadening, phase noise due to leakage poses a different challenge to the radar system.

This has been simulated for a leakage power of 8 dB more the return power of $S_1$ which is just enough to begin seeing its phase noise skirt covering the scatterer and the results are as shown in Figures 5.7 and 5.8. The leakage power was chosen such that at the IF offset corresponding to the target location, the phase noise floor of the leakage signal is at approximately the same level as the target response's peak.

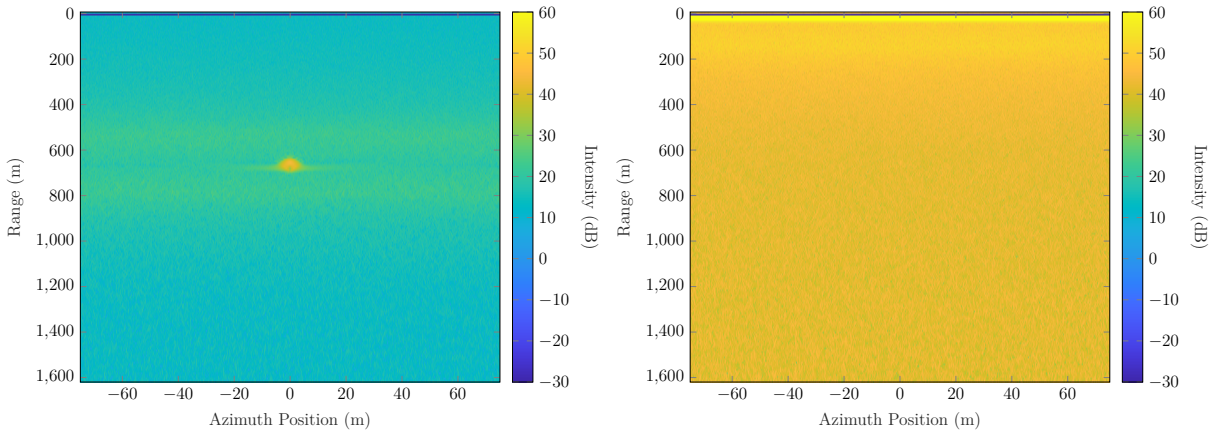


**Figure 5.7:** Simulated point target with phase noise and (a) without leakage and (b) with leakage.

The main challenge with leakage is that it is much higher in power than returns from other targets; thus, it can be seen that the leakage phase noise dominates the noise floor throughout much of the useful portion of the IF spectrum and cannot, simply, be filtered out. This reduces the dynamic range of the FMCW radar and weaker targets are buried in the leakage's phase noise skirt as pointed out in [5] and discussed in Section 2.2.1.

It is especially high in the close-in region making the portion of the spectrum around this unusable which reduces the detectability at close-in offsets range.

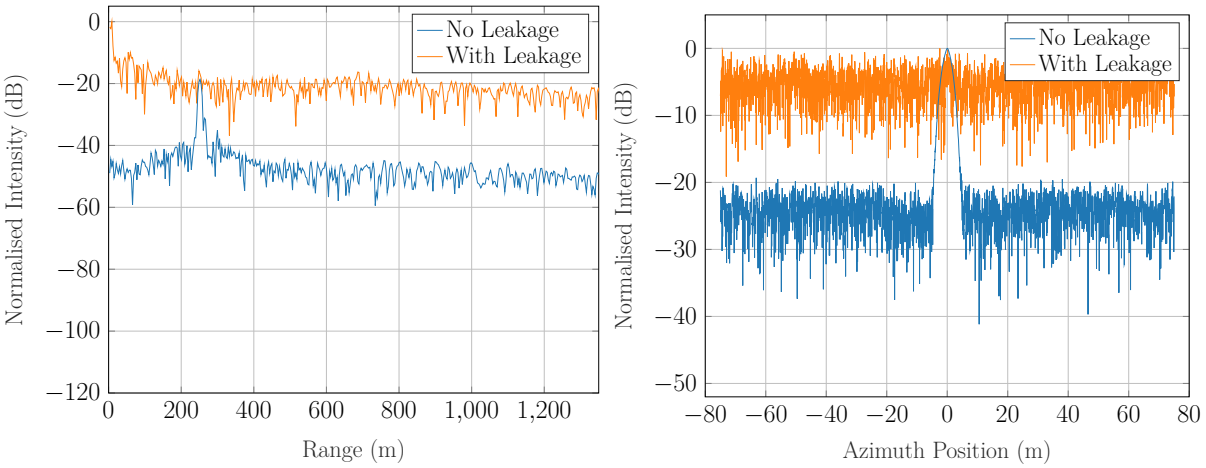


**(a)** **(b)**

**Figure 5.8:** Simulated (a) $\mathrm{IPR}_r$ and $\mathrm{IPR}_a$ for $\mathrm{S}_1$ with and without leakage and obtained using a Hanning range window. Phase noise is also included in the simulation with leakage.

## 5.4 Summary

Phase and frequency instabilities in the synthesised waveform have been identified and their impact on the spectra of the synthesised signals and the IF signal have been discussed.

Ramp quantisation and non-linearity has been shown to not be much of a concern, in Section 5.1, for the current PLL since the loop bandwidth is in the optimum range given by Equation 5.2.

The system has been shown to be afflicted by spurious signals, specifically, fractional spurs. In the interest of avoiding repetition of the work of Jordan [2], the issue of spurs was not discussed to great length.

Phase noise was also noted to be an issue of concern and the focus of the present chapter. In this chapter a theoretical framework for its analysis and optimisation was presented including its mathematical definition characterised by the PSD, the issue of estimating the PSD done via the Welch method and measurement approaches using the obtained PSD.

The actual nature of phase noise in Delta-Sigma PLLs was also discussed. It was found that phase noise due to the reference oscillator, the input path and the N-divider are in-band mechanisms and are therefore filtered by the low-passing PLL transfer function. The VCO is an out-band mechanism and its phase noise is filtered by the high-passing

error function.

In terms of its mapping to the IF domain, the residual phase noise at the output of the mixer is the sum of the phase noise of the two signals at its input ports. However, if the noise sources are correlated, the phase noise is filtered by the range correlation function which can drastically improve performance. The same idea applies for the effect of the ADC on phase noise as sampling can be considered to be a time mixing operation.

To observe how the phase noise manifests in the SAR image, a simulation of the system model was carried out and a stark difference exists between that with and without phase noise. The phase noise skirt of leakage was also simulated and it was observed that it can be detrimental to the system as it raises the noise floor of the IF spectrum to the point that targets may be buried within it.

# Chapter 6

# Integration Testing and Analysis

The fundamental concepts for fractional-N PLL-based waveform synthesis in the miloSAR have been presented in previous sections.

Application of these concepts to characterise the system and implement more performant waveforms, as well as integration of various redesigned components into the system is documented in the present chapter.

The chapter begins with an account of the waveform implementation, which entails validating models for the maximum sweep rate and pull-in time derived in Chapter 4 and applying the findings to synthesise various waveform shapes which, previously, could not be achieved.

Following this, the influence of various system parameter configurations — some of which could only be realised with the new waveforms and system modifications — is investigated. This is done by analysing how changes to the parameters influence the IPR. In the case of changes in PRF, the impact on the quality of the SAR image generated from a dataset acquired by the miloSAR, is examined.

The issue of phase noise as it relates to the real system and the imagery produced is then discussed in greater depth. Characterisation of the system's phase noise performance, analysis of the impact of phase noise and an evaluation of phase noise mitigation strategies are presented.

Finally, the insights obtained from the work documented in the chapter are aggregated and prescriptively presented.

## 6.1 Waveform Implementation

A key objective of this work, RO1, was studying and characterising the PLL synthesiser's loop dynamics so as to implement various FMCW waveforms, including saw-tooth waveforms which were, previously, not achievable. This allows the system to meet certain design specifications such as higher processing gains, avoidance of Doppler aliasing etc.

To this end, the system was modelled, allowing for the extraction of some critical design constraints required to effectively use the synthesiser. Specifically, the maximum sweep rate and the pull-in time constraints were determined and, in this section, measured results are used to validate those obtained from the model.

### 6.1.1 Maximum Sweep Rate Constraint

As previously discussed, one of the primary constraints for PLL-based implementation of FMCW waveforms is the maximum sweep rate. During the effective PRI, the PLL must not lose lock, which would result in undesirable non-linear behaviour such as cycle-slips.

Higher values of sweep rate are pose significant concern because, when attained by reducing the modulation period while keeping the bandwidth fixed, the PLL is likely to lose lock. The maximum sweep rate before the PLL unlocks is given by Equation 4.24 repeated here

$$k_{r_{max}} = \frac{K_{\text{VCO}} K_{\text{PD}}}{a_0} \quad [\text{Hz/s}] \tag{6.1}$$

As shown in Equation 4.3, the phase detector gain, $K_{\text{PD}}$, is related to the charge pump gain (CPG) by

$$K_{\text{PD}} = \frac{\text{CPG}}{2\pi} \quad [\text{A/rad}] \, . \tag{6.2}$$

$a_0$ is computed to be $4.118 \times 10^{-9}$, and the nominal VCO sensitivity of 200 MHz/V is used; therefore, $K_{\text{VCO}}$, is $2\pi \times 200$ MHz $\cdot$ rad/V.

To determine whether the maximum sweep rate constraint holds in practice, the PLL was configured to synthesise ramps at the theoretical maximum sweep rate, $k_{r_{max}}$, and fractions of this. The VCO tuning voltage, which directly influences the output frequency of the PLL, was then measured. For a CPG value of 0.6 mA, a plot of the VCO voltage is shown in Figure 6.1.

It is evident that, for the theoretical $k_{r_{max}}$ and even $k_{r_{max}}/1.5$, the PLL exhibits non-

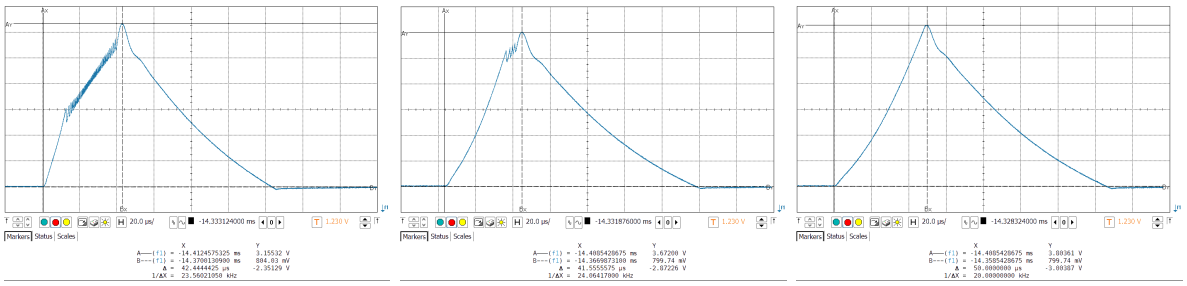

(a) (b) (c)

**Figure 6.1:** VCO voltage for synthesised ramp signals with sweep rate values of (a) $k_{r_{max}}$, (b) $k_{r_{max}}/1.5$, (c) $k_{r_{max}}/3$ with CPG = 0.6 mA

linearity in the form of cycleslips i.e. it loses lock.

Table 6.1 shows the predicted and empirical estimates of the maximum sweep rates.

**Table 6.1:** Theoretical and Practical Maximum Sweep Rate Constraints

| CPG (mA) | Theoretical $k_{r_{max}}$ (Hz/s) | Measured $k_{r_{max}}$ (Hz/s) |
|---|---|---|
| 0.1 | $4.857 \times 10^{12}$ | $2.4285 \times 10^{12}$ |
| 0.6 | $2.914 \times 10^{13}$ | $1.457 \times 10^{13}$ |
| 3.1 | $1.506 \times 10^{14}$ | $1.004 \times 10^{14}$ |

The discrepancy between the predicted values and the measured values is, likely, due to miscalibration of the value of $K_{\text{VCO}}$ in the model as discussed in Section 4.4.1 as well as due to phase noise which can result in the phase error becoming larger than what it nominally is and causing a loss of lock.

Considering the experiments carried out for a variety of CPG values, it was determined that a more practical value of maximum sweep rate is $k_{r_{max}}/2$ where $k_{r_{max}}$ is obtained via Equation 6.1.

### 6.1.2 Pull-in Time Constraint

In order to implement waveforms which involve the PLL losing lock temporarily due to large frequency excursions, such as the sawtooth waveform, it is necessary to know the pull-in time.

This has been modelled in Section 4.4.1 to be given by

$$T_{pull\text{-}in} \approx \Delta\omega_o \frac{NC_1}{K_{\text{PD}} K_{\text{VCO}} \pi} \tag{6.3}$$

To validate this, an experiment was carried out where a step change of $\Delta f = 700$ MHz, in the undivided VCO output, was applied and the approximate time the PLL takes to settle was determined through observing the transient response curve of the VCO voltage after the excitation. This was done for CPG values of 0.1 mA, 0.6 mA and 3.1 mA.

Table 6.2 compares the measured values to the theoretical values of pull-in time.

**Table 6.2:** Modelled and Measured Pull-in Times for $\Delta f = 700$ MHz

| **CPG (mA)** | **Modelled Pull-in Time ($\mu$s)** | **Measured Pull-in Time ($\mu$s)** | **Percentage Error** |
|---|---|---|---|
| 0.1 | 384.610 | 472.0 | 22.8 % |
| 0.6 | 64.101 | 82.822 | 22.6 % |
| 3.1 | 12.407 | 16.924 | 26.7 % |

A strong agreement between the measured and predicted pull-in times can be seen, with an acceptable average error of 24% which is also attributed to errors in model calibration.

The finer details of the pull-in process are discussed in Section 4.4.1; here, the main objective was validating the model.

### 6.1.3 Application

Using knowledge of the dynamic behaviour of the PLL, synthesis of triangular and saw-tooth waveforms was performed. Figures 6.2 and 6.3 show the VCO tuning voltage for synthesis of the saw-tooth and triangular waveforms by the miloSAR for CPG values of 0.1 mA and 3.1 mA.

As presented in Table 6.2 and evident in Figure 6.2a, the pull-in process for CPG = 0.1, when resetting the frequency as required for the sawtooth waveform, is very slow due to a slow reduction of the phase error by the control system with low gain. The resultant waveform instead appears more like an asymmetric triangular ramp rather than the desired saw-tooth form.

The pull-in process for CPG = 3.1 mA is, however, significantly faster which allows the system to operate with the waveforms closer to the sawtooth form albeit having a non-zero frequency reset time. This allows for an increase in duty factor i.e. modulation period and the effects of this are investigated shortly.

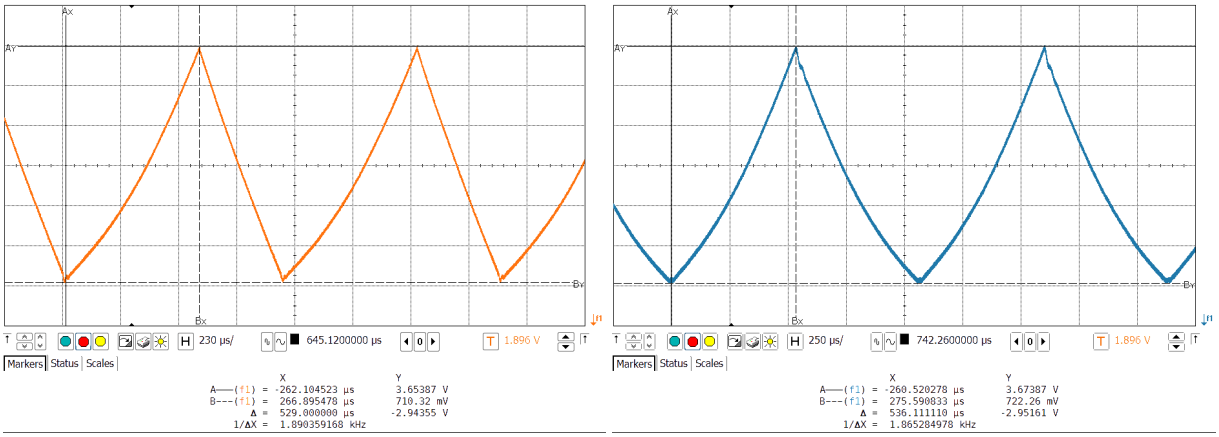


**(a)** **(b)**

**Figure 6.2:** (a) Saw-tooth and (b) triangular waveforms for CPG = 0.1 mA.

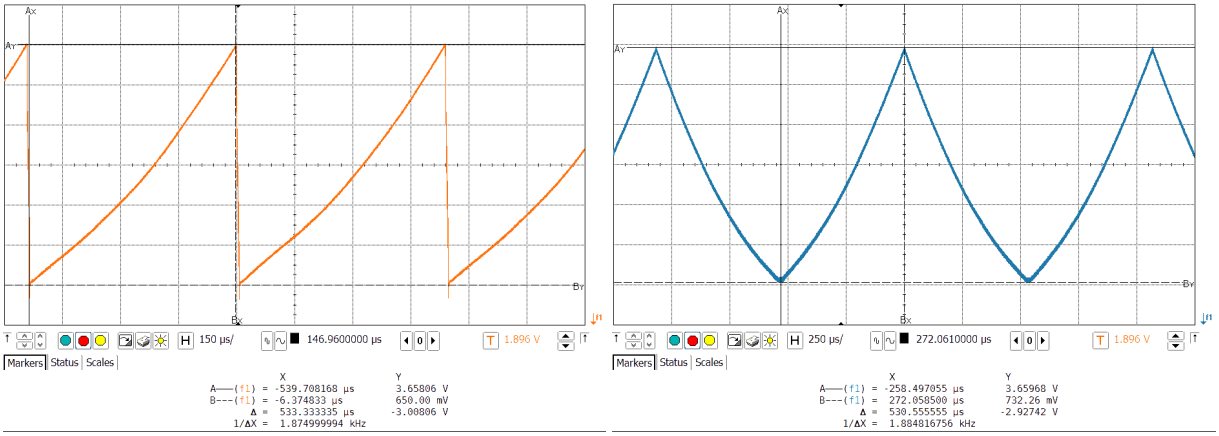


**(a)** **(b)**

**Figure 6.3:** (a) Saw-tooth and (b) triangular waveforms for CPG = 3.1 mA.

## 6.2 Internet Protocol-Based Signal Recording Tests

Modifications were done to increase the throughput of the system as has been discussed in Section 3.1.4 using TCP/IP.

It was of interest to test the throughput of the system and to what extent it could sustain continuous recording at this rate. This investigation was done by carrying out a standard radar loopback test using both the original signal recording scheme (for reference) and the TCP/IP-based recording scheme. The results of the achieved data rates are as shown in Table 6.3.

**Table 6.3:** Comparison of Original and TCP/IP-Based Signal Acquisition Module Throughput

| | **1 min** | **2 min** | **15 min** | **30 min** | **60 min** |
|---|---|---|---|---|---|
| **Original DR (MB/s)** | 10.850 | 10.900 | 10.900 | 10.988 | 10.985 |
| **TCP/IP DR (MB/s)** | 43.555 | 43.301 | 44.205 | 44.500 | 44.530 |

To ensure that the data integrity after transmission over the TCP/IP interface, the original signal recording scheme and the TCP/IP-based recording scheme were used simultaneously and an XOR operation performed on the binary data to check for discrepancies between the two. The data was found to be identical.

This development allows for use of the system with much higher PRFs and at a higher sampling rate that can capture the full 3.8 MHz intermediate frequency bandwidth without aliasing.

## 6.3 Influence of Waveform Parameters on System Performance

Having performed all the necessary system modifications and characterisations to implement and use the system with greater flexibility in the waveforms, it is now of interest to address RO2, which is to determine the role of various waveform parameters in system performance for better system optimisation.

SAR IQ metrics were discussed to great detail in Section 3.3.3. A key takeaway from the section was that these metrics are extracted from the IPR and in the present section, they are used to quantify the impact of various parameters on the system performance.

For the testing and analysis, a loopback cable was deemed to be the most appropriate means of obtaining the range IPR as it isolates issues related to the waveform synthesis from all other issues that would result from operating the radar in motion such as nonlinear motion errors, range migration etc. The particular cable employed for this purpose was the 100 m, 50 Ω HUBER+SUHNER [76] coaxial cable with a signal propagation velocity of 83% that of light in freespace.

Azimuth IPR is much more difficult to obtain through lab tests; thus, is not analysed to the same extent as the range IPR in this chapter. Where appropriate, an azimuth cut through the brightest target in a SAR image is taken for or used to infer the behaviour

of the azimuth IPR.

The fixed system configuration used for the miloSAR prior the author beginning this work is taken as the benchmark and is summarised in Table 6.4. From this, parameters are varied to observe how they affect system performance.

**Table 6.4:** Benchmark System Parameters

| **Parameter** | **Symbol** | **Value** |
|---|---|---|
| Modulation Bandwidth | $B_r$ | 175 MHz |
| IF Bandwidth | $B_{\text{IF}}$ | 3.125 MHz |
| Modulation Period | $T_r$ | $4.026 \times 10^{-4}$ s |
| Sweep rate | $k_r$ | $1.739 \times 10^{12}$ Hz/s |
| Pulse Repetition Frequency | PRF | 1250 Hz |
| Range Processing Window | | Hanning |

Figure 6.4 shows the range IPR for the benchmark system obtained using CPG = 0.6 mA.

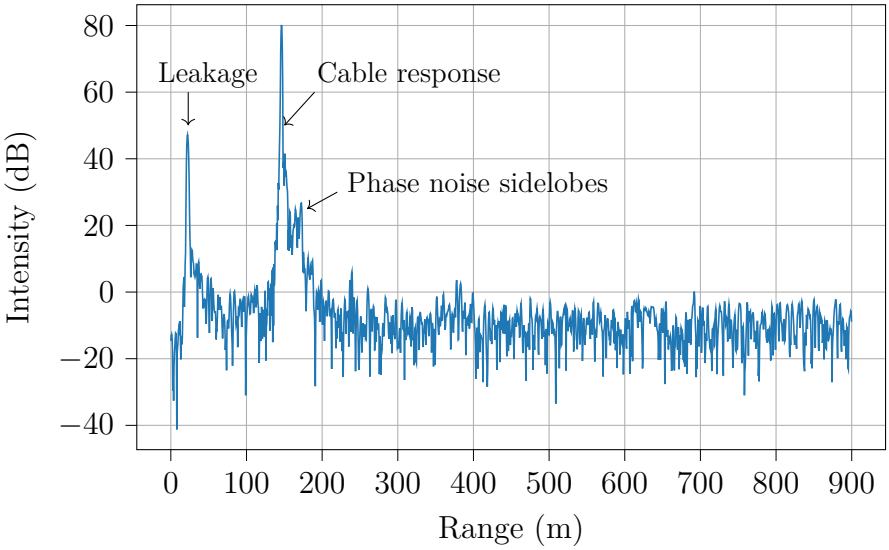


**Figure 6.4:** $\text{IPR}_\text{r}$ for benchmark system following coherent integration of 6250 pulses.

A zoomed in version of the range IPRis as shown in Figure 6.5.

The peak corresponding to the cable's response is seen to appear at 146.3 m after scaling of the frequency axis, using Equation 3.3, which is reasonably accurate taking into account uncertainties in the values of propagation velocity, cable length and sweep rate.

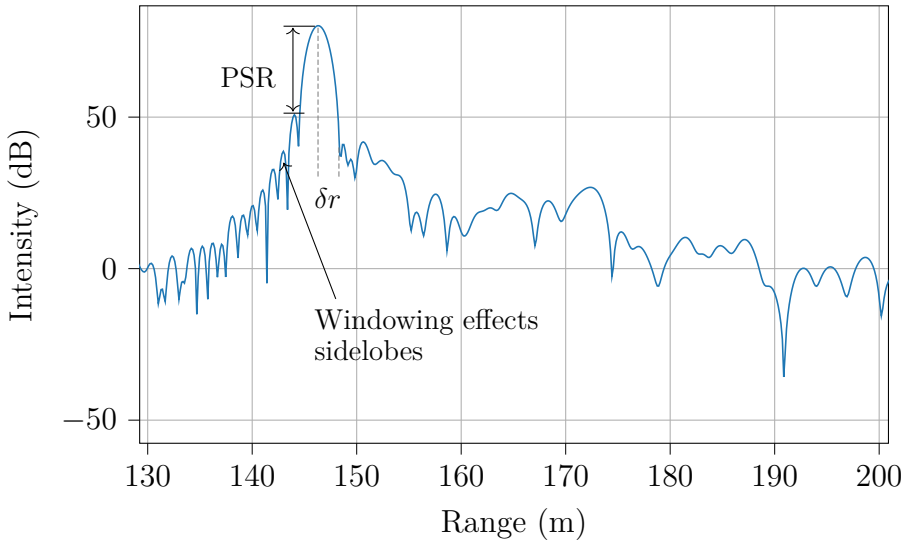


**Figure 6.5:** Zoomed in range IPRfor benchmark system.

Another peak is seen at 18.25 m, corresponding to internal leakage of the system. It will be shown that with the antenna incorporated, the leakage signal is much stronger and has an adverse impact on system performance.

Range resolution of the range IPR is 2.055 m. The theoretical range resolution obtained via Equation 3.17 is 0.711 m which implies that the mainlobe broadening factor due to the Hanning window applied during processing is approximately 2.890. This is reasonably close to the expected factor of 2, according to theory [77], with the discrepancy being, likely due, to approximation errors in the bandwidth measurement used in Equation 3.17.

Sidelobes can be observed with a regular pattern in the direction of decreasing range and a more irregular pattern in that of increasing range. These are a well known phenomenon in signal processing [78], attributed to the non-finite time interval over which the data used to perform the range FFT is collected.

The erratic pattern of the sidelobes in the direction of increasing range is due to the spectral modification effects of phase noise which will be discussed in Section 6.4.

Application of the Hanning window helps apodise these sidelobes from a PSR of -13.25 dB to -33.7 dB for the LFM waveform and considering the range IPR from the 100 m to 900 m, the ISR is 24.129 dB. While literature does not specify exact values for acceptable ISR levels, this metric holds significance as it indirectly quantifies the contrast of the SAR image. It provides system designers with insight into how the image's contrast will vary based on different design choices that affect the ISR.

The rest of this section is focused on investigating how system parameters affect these

and other image quality metrics.

### 6.3.1 Influence of Sweep Rate on Impulse Response

Sweep rate, by definition, can be altered by changing one of two parameters: the modulation period or the modulation bandwidth. It is a critical design parameter in radar systems as has been noted in Section 4.5.2 and its impact is explored here.

The waveforms used to investigate this are summarised in Table 6.5.

**Table 6.5:** Waveforms for investigating effect of varying sweep rate on impulse response.

| **Waveform Label** | **Sweep rate ($k_r$) (Hz/s)** | **Modulation bandwidth ($B_r$) (MHz)** | **Modulation period ($T_r$) (s)** |
|---|---|---|---|
| W1 | $4.347 \times 10^{11}$ | 175 | $4.026 \times 10^{-4}$ |
| W2 | $1.883 \times 10^{12}$ | 175 | $9.296 \times 10^{-5}$ |
| W3 | $2.557 \times 10^{11}$ | 175 | $6.843 \times 10^{-4}$ |
| W4 | $2.484 \times 10^{11}$ | 100 | $4.026 \times 10^{-4}$ |

#### Varying Modulation Period for Fixed Modulation Bandwidth and PRF

Consider a fixed modulation bandwidth of 175 MHz and PRF of 1250 Hz but varying modulation period. Figures 6.6 and 6.7 show the range IPR, for a single pulse, of the benchmark system but with waveforms W2 ($T_r = 9.296 \times 10^{-5}$ s) and W3 ($T_r = 6.843 \times 10^{-4}$ s) respectively.

The range processing gains, $G_r$, for the short ramp and long ramp are predicted, via Equation 3.5 to be 42.113 dB and 50.782 dB respectively which is approximately what is observed in the plots.

The long ramp has an SNR which is, approximately, 8.669 dB more than that of the short ramp and the implication of this is evident in the plots as the internal leakage visible in Figure 6.7 has completely disappeared into the noise floor in Figure 6.6. Similarly, very weak targets may be invisible below noise and background clutter but detectable with a higher range processing gain; therefore, the gain should be as high as possible to ensure maximum visibility of targets, which requires the high duty cycle capability offered by the sawtooth waveform.

It can also be observed, that since the sampling rate is fixed, the short ramp results in less samples being available for processing by means of the FFT. Since each frequency

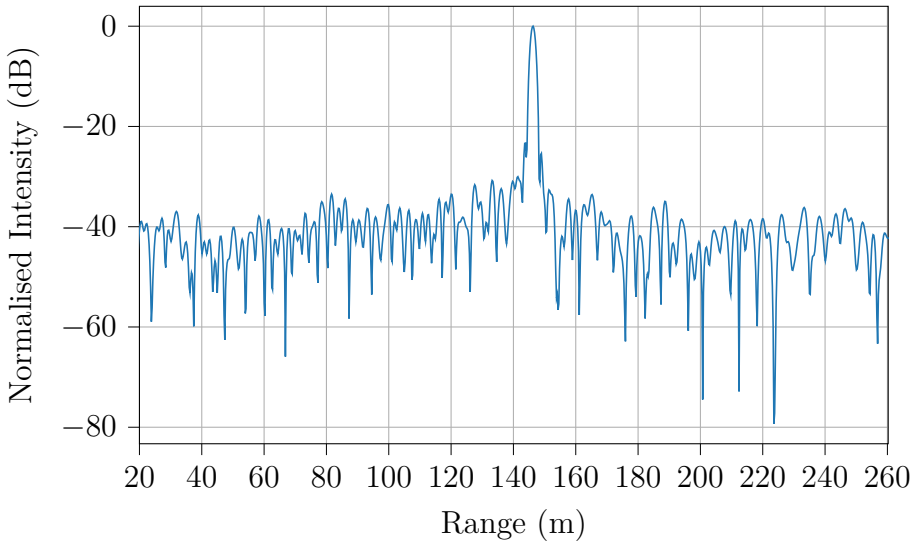


**Figure 6.6:** Single pulse range IPR for waveform W2 ($T_r \approx 9.296 \times 10^{-5}$ s) and CPG = 3.1 mA.

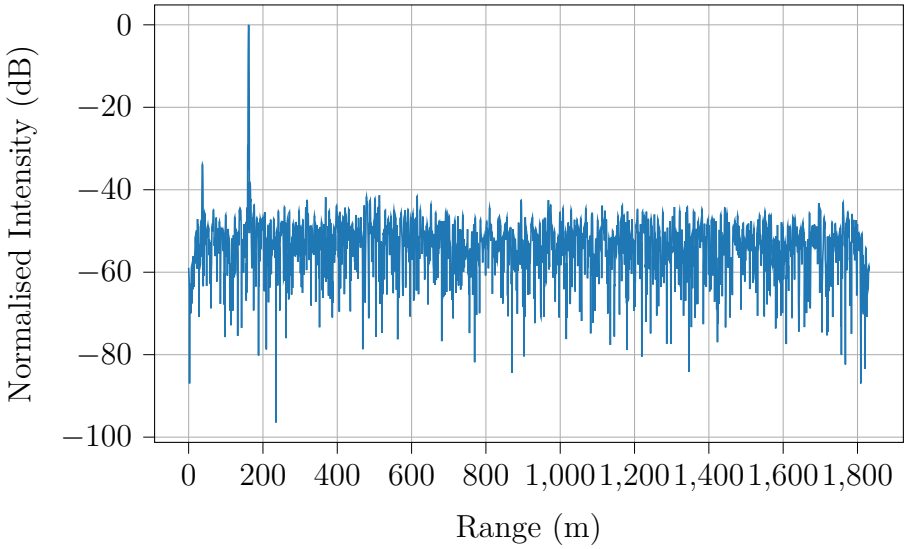


**Figure 6.7:** Single pulse range IPR for waveform W3 ($T_r \approx 6.843 \times 10^{-4}$ s) and CPG = 3.1 mA.

bin corresponds to a fixed (when modulation bandwidth is fixed) distance, less samples means a smaller swath width.

### Varying Bandwidth for Fixed Modulation Period and PRF

It is generally understood that a reduction in bandwidth results in loss of range resolution.

The single pulse result of testing the system with waveform W4 ($B_r = 100$ MHz) and the benchmark waveform W1 ($B_r = 175$ MHz) is shown in Figures 6.8 and 6.9.

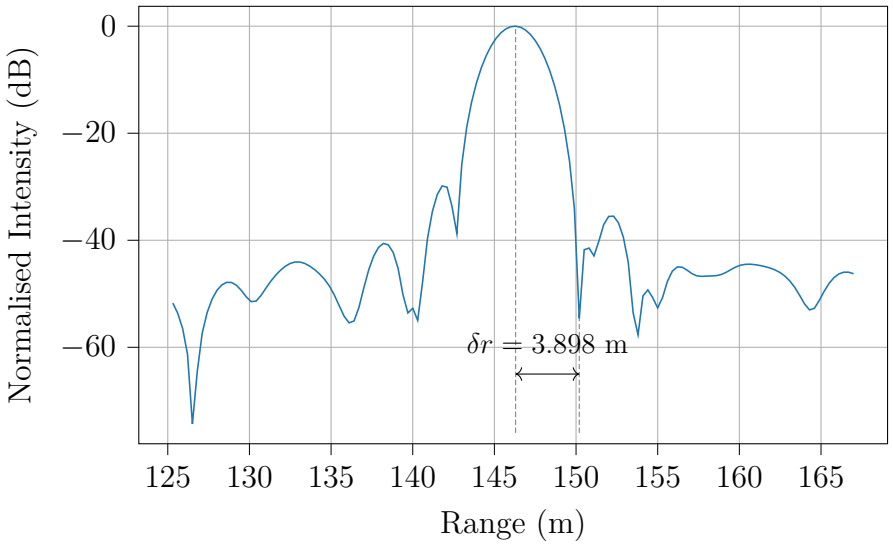


**Figure 6.8:** Single pulse range IPR for waveform W4 ($B_r \approx 100$ MHz).

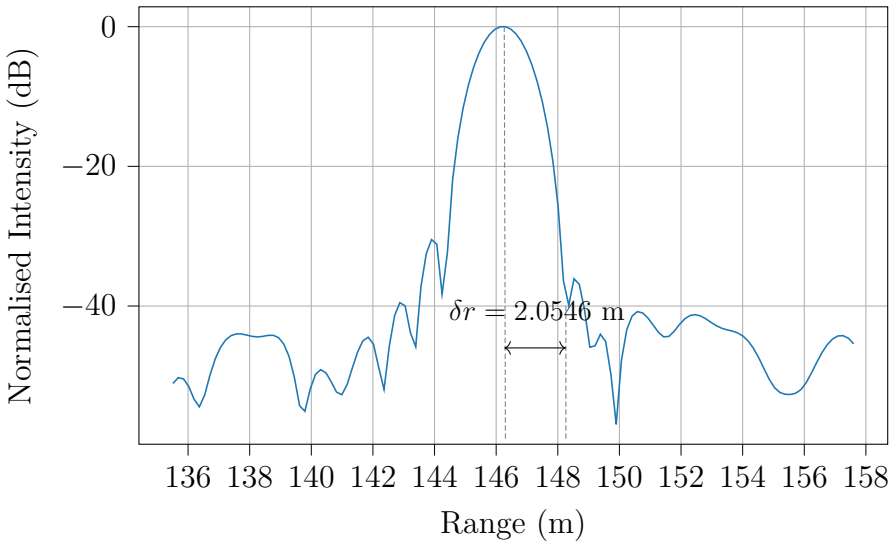


**Figure 6.9:** Single pulse range IPR for waveform W1, ($B_r \approx 175$ MHz).

A significant difference in range resolution, of 1.8434 m, is observed for a 75 MHz difference in modulation bandwidth. The achieved range resolution is 3.898 m which is in strong agreement with 3.595 m obtained through using Equation 3.17 and the aforementioned mainlobe broadening factor of 2.890.

### 6.3.2 Influence of Pulse Repetition Frequency

The role of PRF has been discussed in Sections 3.2.2 and 4.5.2. It has been noted to impact the coherent integration gain. Additionally, since the Doppler bandwidth is sampled at the PRF, the PRF is required to satisfy the Nyquist criterion for a given

platform velocity, in order to avoid Doppler aliasing.

It is also important to highlight that any challenges with the PRF being too low are exacerbated by operation of the system in its multi-polarimetric mode which has the effect of halving the PRF.

The primary means to increase the PRF, in terms of the actual ramp and not mode of operation, is by changing the sweep rate either by decreasing modulation period or modulation bandwidth. The consequences of both have been shown in prior sections. Presently, the general effects of PRF variations are explored.

### Coherent Processing Gain

The expressions for computing azimuth processing gain and number of pulses during the CPI are given in Equations 3.6 and 3.7 respectively.

Figure 6.10 shows the range IPR obtained using the loopback cable for varying integration gains (i.e. number of pulses coherently integrated).

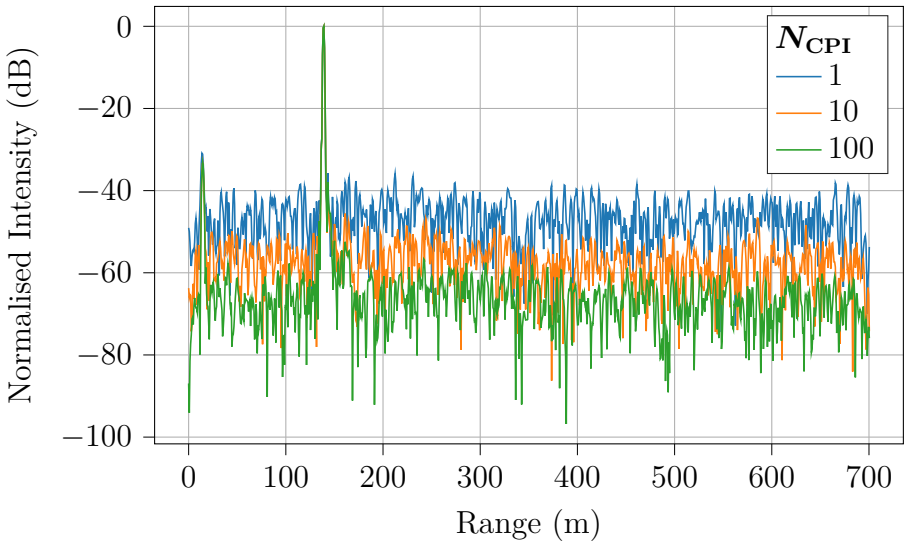


**Figure 6.10:** Range IPRfor varying number of coherently integrated pulses.

The measured SNR is approximately -44.7 dB for $N = 1$, -54.0 dB for $N = 10$ and -64.9 dB for $N = 100$. This is, exactly, in accordance the discussion in Section 3.2.2 which states that the processing gain achieved by coherently integrating $N$ pulses is $N$. This means that SNR is improved by $10 \log N$dB which could significantly aid the visibility of weak targets in the SAR image.

### Doppler Aliasing

To observe the role of the PRF in terms of Doppler aliasing, multi-rate processing is applied on a test dataset collected at Fisantekraal, Cape Town by the miloSAR.

The approach of using a single dataset and, through signal processing techniques, altering the parameters in this manner is employed for a number of reasons. Firstly, in order to make meaningful comparisons, it is essential that the dataset be identical save for the phenomena under investigation otherwise incorrect conclusions are most likely to be drawn. It is not possible to obtain exactly the same image twice, more so with the miloSAR, because platform cannot follow the exact same path and even if it could, there are phase changes that occur between the imaging intervals. Secondly, it is laborious and very expensive to acquire data with deliberate errors merely for the sake of analysis especially when the issue can be reproduced exactly by means of software routines on the data.

As such, the aforementioned reference dataset was used, and the azimuth sampling rate, i.e. the PRF, was decimated to achieve varying PRFs. The platform velocity for this collection was, approximately, 31.045 m/s which means that the required PRF to avoid Doppler aliasing is 600 Hz.

While the actual waveforms had a PRF of 1250, a pre-summing factor of 2 was used bringing down the effective PRF to 625 Hz. For the current investigation the image was formed with both the PRF of 625 Hz and 156.25 Hz where the latter was achieved through decimation by a factor of 4.

Figure 6.11 shows the processed SAR images.

There is a very apparent degradation in image quality, mostly, as a result of distortion of the Doppler spectrum due to aliasing. A ghost image is seen to overlay the true image, formed as a result of spectral replication caused by the aliasing.

Consequently, the background increases and since the two images are not in alignment, this rise in the background levels can be treated as a rise in the noise floor. This causes severe deterioration of target visibility an apparent loss in image contrast.

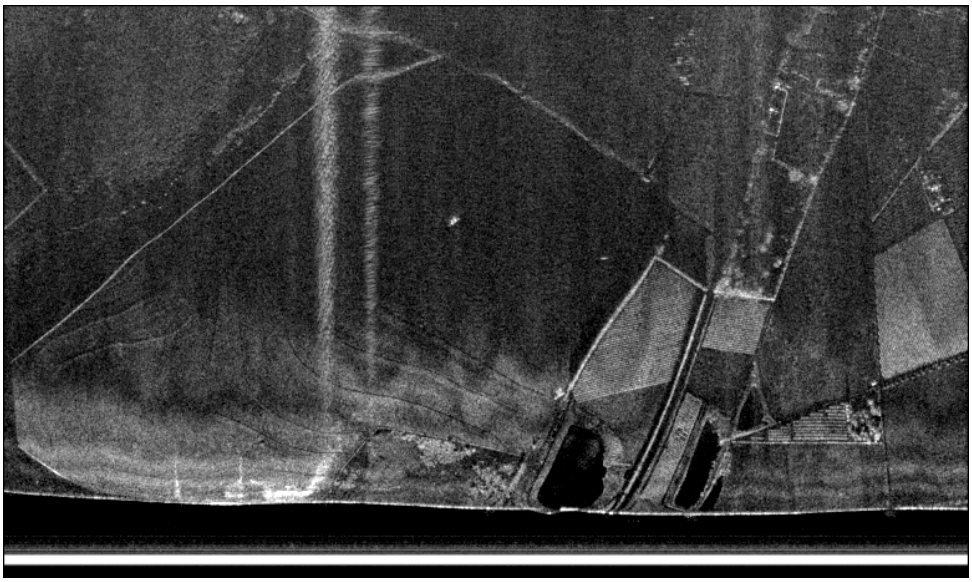

**(a)**

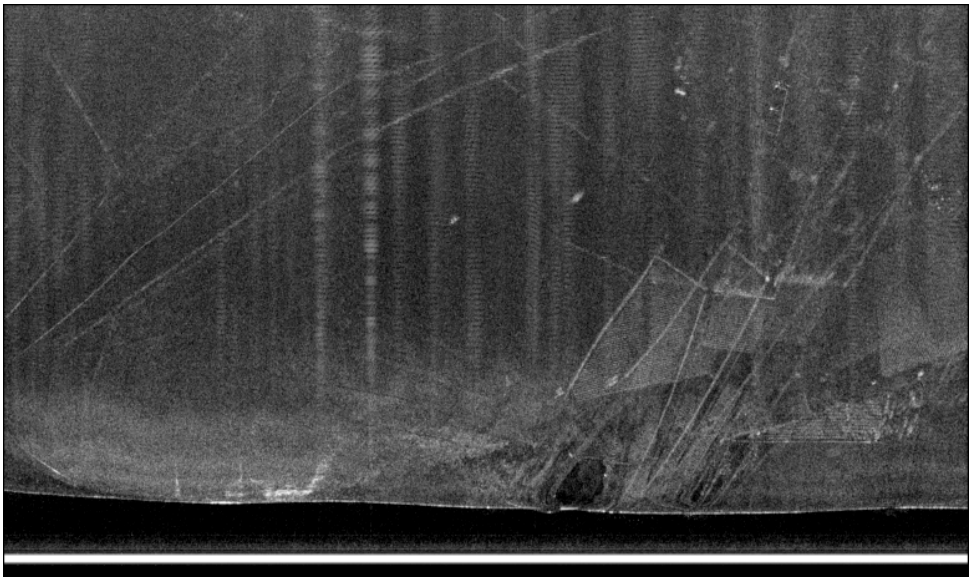

**(b)**

**Figure 6.11:** Doppler aliasing in reproduced SAR image for data acquired by the miloSAR in Fisantekraal, Cape Town with PRF values of (a) 625 Hz and (b) 156.25 Hz.

## 6.4 Phase Noise

Phase noise has been noted to be a key specification for radar systems and has been a primary focus of this work. In Chapter 5, it was concluded that it causes spectral artifacts that may appear as targets in the SAR image and, non-uniformly, raises the noise floor

of the IF spectrum resulting in SNR and dynamic range degradation.

Presently, the studied concepts are applied to a real FMCW SAR system, the miloSAR, in order to obtain *bona fide* results for how phase noise behaves in practice and to identify any characteristics of significance.

### 6.4.1 System Phase Noise Performance Characterisation

Determining how the system, in its present state, performs in terms of phase noise is imperative as it sets a baseline for evaluating the effectiveness of improvements and gives insights to drive future design choices.

#### PLL Phase Noise

The primary sources of phase noise within the system are the PLL synthesisers, as has been previously stated.

Figure 6.12 shows the phase noise profiles of one of the LMX2492EVM synthesiser boards, measured using the spectrum analyser as discussed in Section 5.3.2, at different frequency outputs along the sweep bandwidth. The frequencies selected were 2.35 GHz, 2.4375 GHz and 2.525 GHz which are the minimum, median and maximum, respectively, over the range of the PLL (with the VCO divider factor of 4). Again, the CPG used was 3.1 mA.

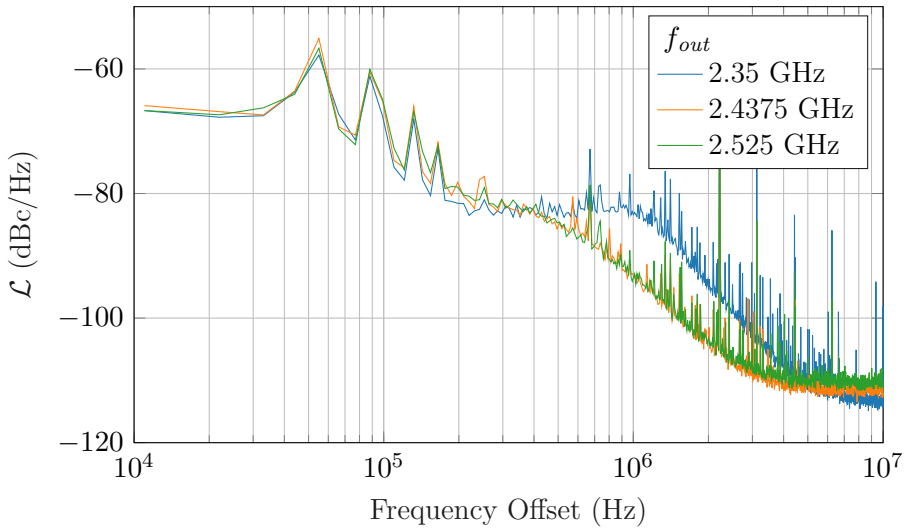


**Figure 6.12:** PLL output phase noise over the range of the PLL with a CPG of 3.1 mA.

The low pass phase error filtering characteristic of the PLL is evident as predicted in

theory, with no attenuation being observed at smaller offsets from the carrier and a large attenuation farther away from the carrier.

In-band phase noise is, seen to be dominated by the phase noise of the CXO BFBC90 (125 MHz) reference oscillator which is shown in Figure 6.21. The in-band phase noise is at an average level of, approximately, -66.5 dBc/Hz and is consistent for all the selected PLL output frequencies.

The Delta-Sigma phase noise bump is also apparent, as discussed, starting from offsets of around 400 kHz and is seen to reach levels of -83 dBc/Hz. It is more pronounced for the 2.35 GHz output frequency which suggests that it increases with a decrease in the PLL's N-divider value, $N$.

At offsets beyond 5 MHz, the phase noise profile is seen to flatten into the noise floor of approximately -115 dBc/Hz and, as will be shown, is dominated by the VCO phase noise. In this noise floor, the PLL's output frequency, which is controlled by the N-divider value, $N$, also influences the phase noise and a decrease in the noise is observed for a decrease in the output frequency (i.e. a decrease in $N$).

### Phase Noise in IF Spectrum

The mapping of phase noise from the transmit and local oscillator signals to the IF spectrum was discussed in Section 5.3.4 and it was pointed out that phase noise of the aforementioned signals overlaps to form residual phase noise given by

$$S_{\Delta\phi_n}(f) = \kappa\, S_\phi \quad [\text{rad}^2/\text{Hz}] \tag{6.4}$$

where,

$$\kappa = \begin{cases} 2 & \text{if noise sources are correlated} \\ 4\sin^2\left(\frac{\tau_d f}{2}\right) & \text{if noise sources are uncorrelated} \end{cases} \tag{6.5}$$

Figure 6.13 shows the phase noise profile of a 9.5 MHz beat signal generated by mixing and bandpass filtering 2.3595 GHz and 2.35 GHz tones from the transmit and local oscillator synthesisers with PLL bandwidths[1] of 26.201 kHz, 73.568 kHz and 302 kHz which correspond to CPG values of 0.1 mA, 0.6 mA and 3.1 mA respectively. The 50 dB attenuator was used and the frequencies selected were 2.3595 GHz and 2.35 GHz because when mixed, they result in a beat frequency at 9.5 MHz which is around the middle (i.e.

[1]The PLL bandwidth is discussed in Section 4.3.

median) of the system's IF frequency range. This median is a good observation point for making generalisations. This is measured just before the ADC.

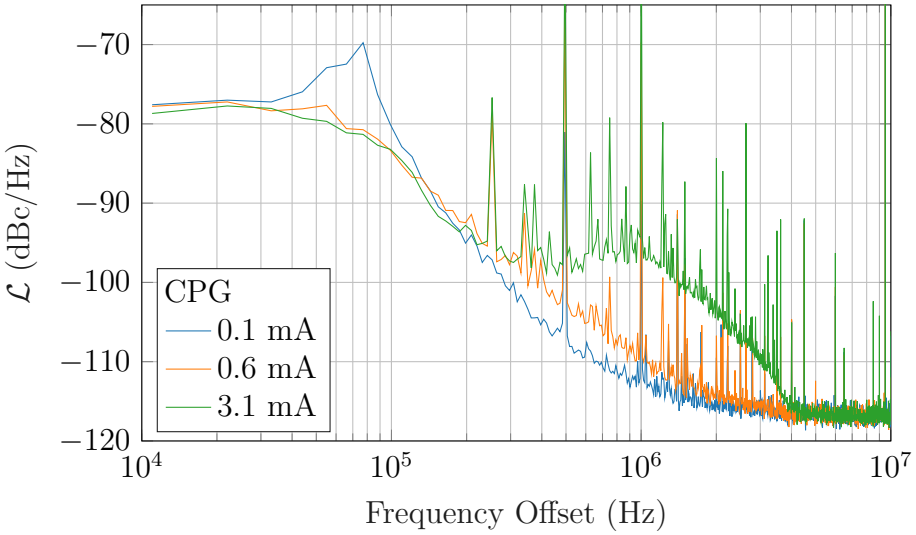


**Figure 6.13:** Phase noise in IF spectrum obtained by mixing 2.3595 GHz and 2.35 GHz frequency tones.

The most notable result is that, range correlation filtering is observed to manifest. This is due to using the same clock as the reference for both PLLs which resulted in the phase noise of the PLLs being partially correlated, specifically, in the PLL bandwidth.

This filtering resulted in a 10.892 dB decrease in in-band phase noise to a level of approximately -77.591 dBc/Hz. This is not nearly as much as the 150 dB reduction predicted by Equation 6.4 but the discrepancy can be attributed to several issues including the fact that the in-band phase noise is not completely correlated and the fact that the derivation of the correlation filter transfer function assumes stationarity which is not the case in PLL phase noise.

A resonant peak is also seen to be very pronounced for the PLL bandwidth of 26.201 kHz due to a lower damping ratio caused by the decrease in bandwidth. At an offset of 80 kHz, the resonant peak is 10 dB more than for the other PLL bandwidths and this is concerning because it may appear as a target in the SAR image.

To observe the phase noise of the IPR in the digital domain (i.e. sampled by the ADC), a 50 dB attenuator in series with a 30 cm loop back cable was used to obtain a phase noise profile and the result is as shown in Figure 6.14. Since phase noise is measured relative to the carrier (i.e. peak), the peak's signal level is of not much significance so long as it is high enough that it allows for observation of the phase noise profile above the noise floor at the desired frequency offsets and low enough that it does not damage the system. The

signal through the attenuator meets this criteria. The frequency range considered is 10 kHz — 4 MHz and the RBW was taken to be 762.939 Hz.

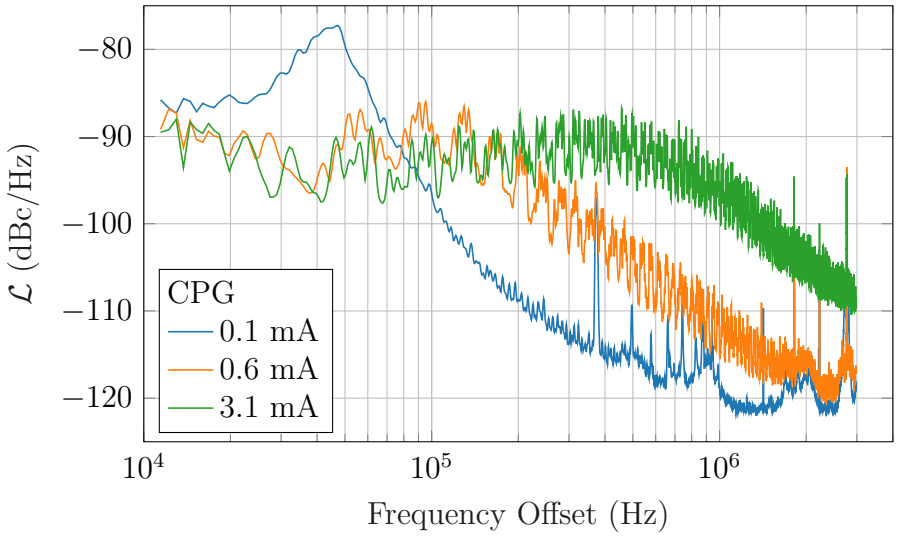


**Figure 6.14:** Phase noise of sampled IF spectrum with near zero-range return.

It can be noted that a further -12.622 dB reduction in the in-band phase noise was achieved due to range correlation filtering because the same clock used as the PLL reference was also used as the ADC clock. This brought the phase noise down to an average of -90.213 dBc/Hz which is approximately the same level as the Delta-Sigma characteristic bump.

Ripples can also be observed in the response throughout the analysed spectrum which are as a result of *spur chirps* and whose treatment is the subject of Jordan's work [2] as mentioned earlier.

### 6.4.2 Impact of Phase Noise on System Performance

Having quantified the system's phase noise characteristics, attention is now shifted towards exploring what implications this has on the radar's ability to perform its intended function.

As previously stated, the phase noise problem in FMCW SAR can be broken down into two elements which are phase noise due to bright, in an RCS-sense, targets and phase noise effects of the leakage signal.

### Leakage Phase Noise

The miloSAR antenna has, approximately, -80 dB of leakage. While this could be improved by increasing antenna separation, the separation cannot be too large as the system would become too large for UAVs and small aircraft.

The phase noise skirt of the leakage is known to raise the system noise floor as reported in literature and observed in simulation results.

To test and assess the severity of the problem, the system, with PLL bandwidths of 2.081 MHz and 8.976 MHz, was used to detect corner reflectors as shown in Figure 6.15.

**(a)** **(b)**

**Figure 6.15:** Static radar system test setup.

The range profile, after coherent integration, and the PSD are as shown in Figures 6.16 and 6.17 respectively.

It is very noticeable that an increase in the PLL bandwidth allowed more phase noise to pass through the PLL unfiltered which resulted in the leakage signal's phase noise skirt raising noise significantly throughout the IF spectrum.

SBR of the first two reflectors does not appear affected as it is within a region where the in-band phase noise is the same for both loop bandwidth configurations. However, SBR of CR3 is 22.3 dB with the narrower PLL bandwidth and 12.2 dB with the wider bandwidth because the response of corner reflector appears at a point where the PLL, with the narrower loop bandwidth, begins filtering out the leakage signal's phase noise skirt.

The PSD plot shows that several other targets can be observed past the lamppost for $B_{3\text{dB}} = 2.081$ MHz owing to the fact that the PLL filters out leakage phase noise that clearly masks the targets in the plot for $B_{3\text{dB}} = 8.976$ MHz. SBR for target TR1, for

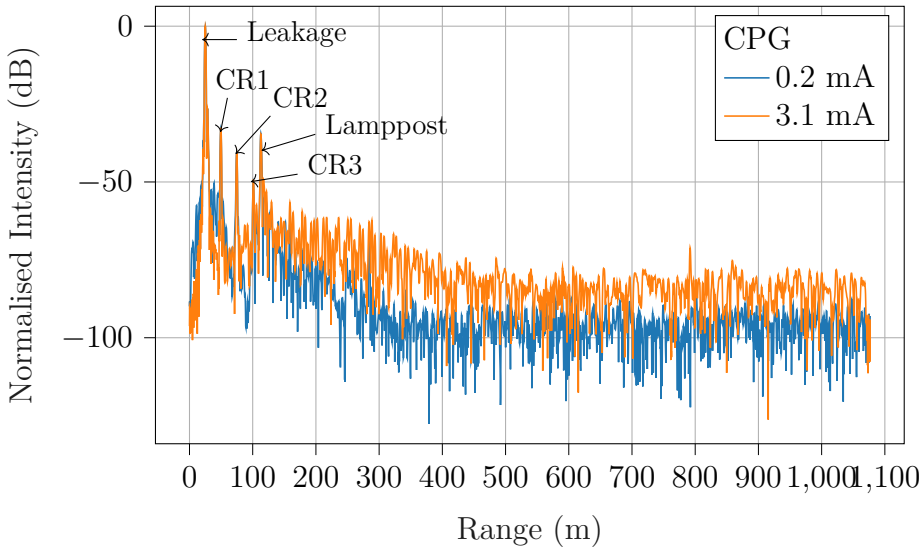


**Figure 6.16:** Range profile for field test setup.

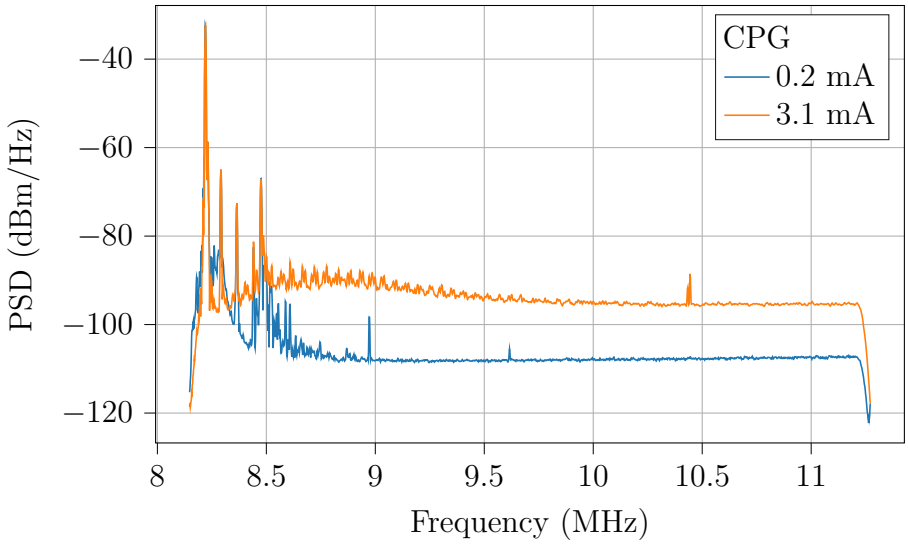


**Figure 6.17:** PSD of IF spectrum for field test setup.

instance, is 9.66 dB while it is completely buried in noise for $B_{3\text{dB}} = 8.976$ MHz.

As was discussed in Section 3.3.1, this is the anti-objective of SAR systems as they are required to achieve detectability of targets as much as possible.

It can also be seen that the noise floor for the configuration with the wider bandwidth does not reach levels as low as that of the narrower bandwidth configuration within the portion of the IF of interest and there is a difference of 12.08 dB in the background floor at ranges past 1000 m.

### Large RCS Scatterers

Determining effects of phase noise due to strong targets using the same system setup as that used for antenna leakage is challenging to do for two main reasons.

Firstly, with the antennas incorporated in the device under test (DUT), the effects of the strong scatterers cannot be isolated from those of leakage. Secondly, it is difficult to obtain an open area with long ranges where the targets can be placed. Instead, the aforementioned loopback cable was used and a plot of its response's PSD for PLL bandwidths of 2.081 MHz and 8.976 MHz is shown in Figure 6.18

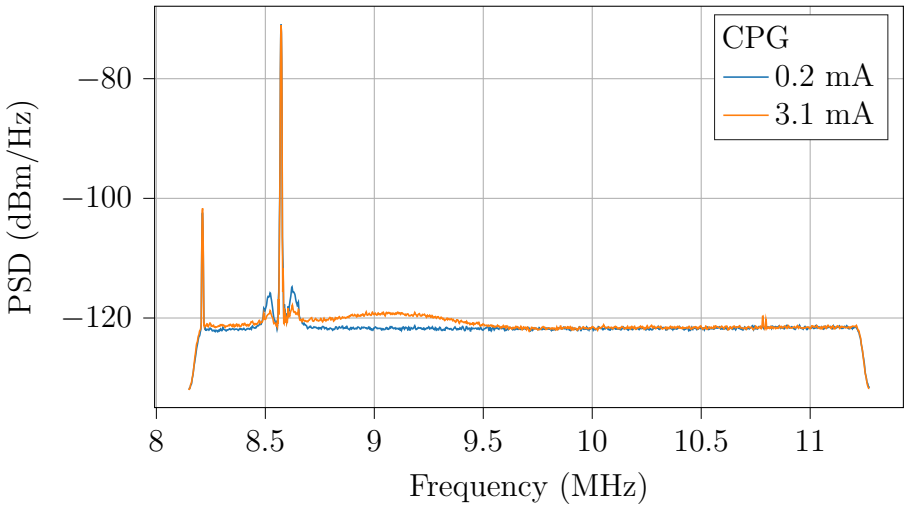


**Figure 6.18:** PSD of IF spectrum for 100 m loopback test.

It can be seen from the plot that, because the return power is relatively low, the phase noise skirt of the loopback cable is partially buried under the thermal noise floor. However, in-band phase noise as well as the Delta-Sigma characteristic curve *can* be seen to be protruding through. For the narrower bandwidth, especially, the phase noise that leaks through the resonant peaks of the PLL filtering response can be seen appearing like actual targets. This can be a big problem because these peaks appear in the frequency band of interest and cannot be discarded like they could be for leakage.

The fact that the phase noise for the the loopback cable is mostly buried under noise also highlights what to expect in a real imaging scenario. When carrying out actual imaging, the clutter would most likely be much stronger than noise and the signal peaks of interest would most likely be just slightly above the clutter. Therefore, due to range correlation filtering, it is expected that phase noise due to scatterers with a strong RCS would not be a problem in miloSAR images because an SCR of above 65 dB would be required for the phase noise to become visible and this is quite unlikely to happen.

### 6.4.3 Manifestation in SAR Image

The challenges of comparing the role of variation of parameters in SAR image quality for the current work have been discussed in Section 6.3.2.

In addition to the issues pointed out, obtaining several datasets under different system configurations for analysis also results in a limitation in the degree of control of phase noise levels.

Fortunately, the effects of phase noise can also be emulated, by modulating the phase of the IF signal with a random sequence of phase errors having an appropriate PDF — in this case, Gaussian — and the appropriate frequency domain characteristics. This is done by generating the sequence as described in Section 5.3.5 and convolving it, in the frequency domain, with each range profile's IF spectrum. Implementation of the convolution is more efficiently done as a multiplication of the corresponding time domain signals.

To prove validity of this approach, the response of the aforementioned attenuator with the system having as low phase noise as possible in the IF spectrum (i.e. having a narrow PLL bandwidth) was obtained and augmented to resemble the response that would be obtained if the system had high out-band phase noise as well as if the system had high in-band phase noise.

Figure 6.19 shows the PSDs of the responses of the attenuator with no augmentations for a narrow and wide PLL bandwidth as well as the response of the attenuator with a narrow PLL bandwidth but augmented to resemble scenarios for high out-band phase noise and high in-band phase noise.

It can be seen that the IF spectrum of the attenuator's response, augmented to resemble a high out-band phase noise configuration, is similar to the IF spectrum of the system when operated with a CPG of 3.1. The actual system with the CPG of 3.1, however, shows ripples due to the aforementioned spur chirps, but these are of no relevance to the investigation of phase noise.

Furthermore, the plots for the actual system response with a CPG of 0.1 mA and for the system with modelled high in-band phase noise reveal the presence of spurs which get buried under a high noise floor for higher CPG values.

Since the response for a CPG of 0.1 mA was augmented to generate the modelled responses, the resonant peak associated with wide PLL bandwidths as discussed in Section 4.3.2 manifests in the modelled response for high out-band phase noise resulting in a large

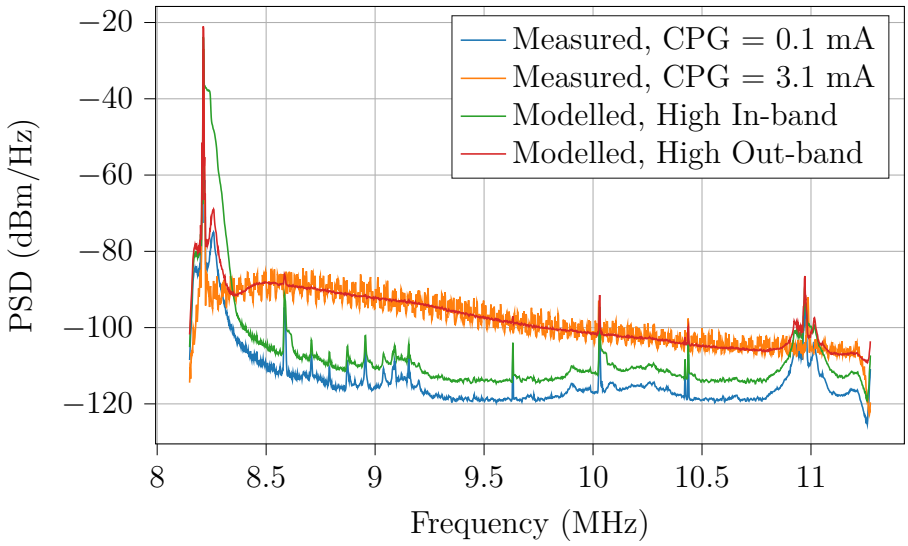


**Figure 6.19:** PSD of attenuator loopback test with varying additive phase noise levels.

discrepancy at small offsets. However, this is acceptable as the focus for this case will be on the regions of the IF spectrum corresponding to the out-band region.

Figure 6.20 shows the Fisantekraal dataset with relatively low phase noise as it was originally collected and with the above augmentations for high out-band phase noise and high in-band phase noise.

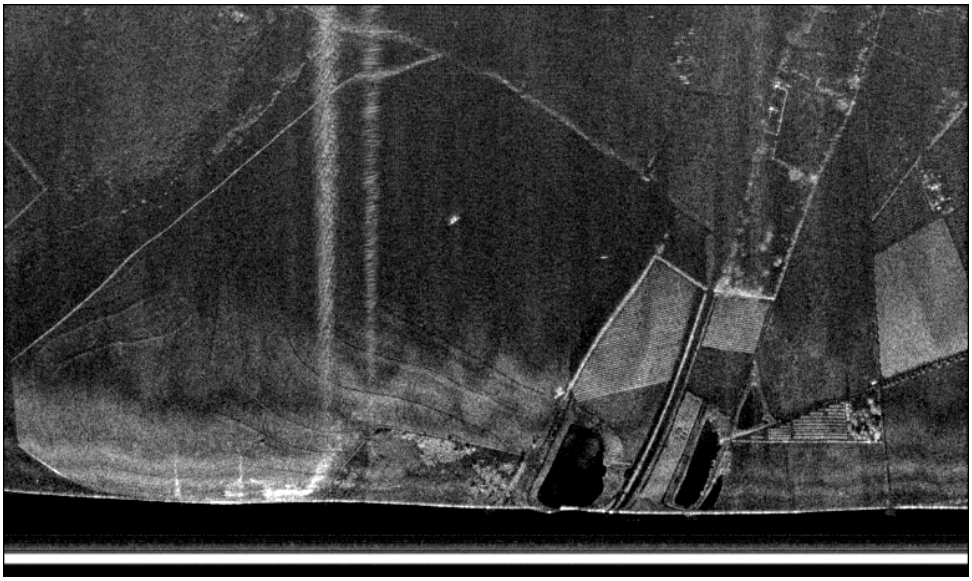

**(a)**

**(b)**

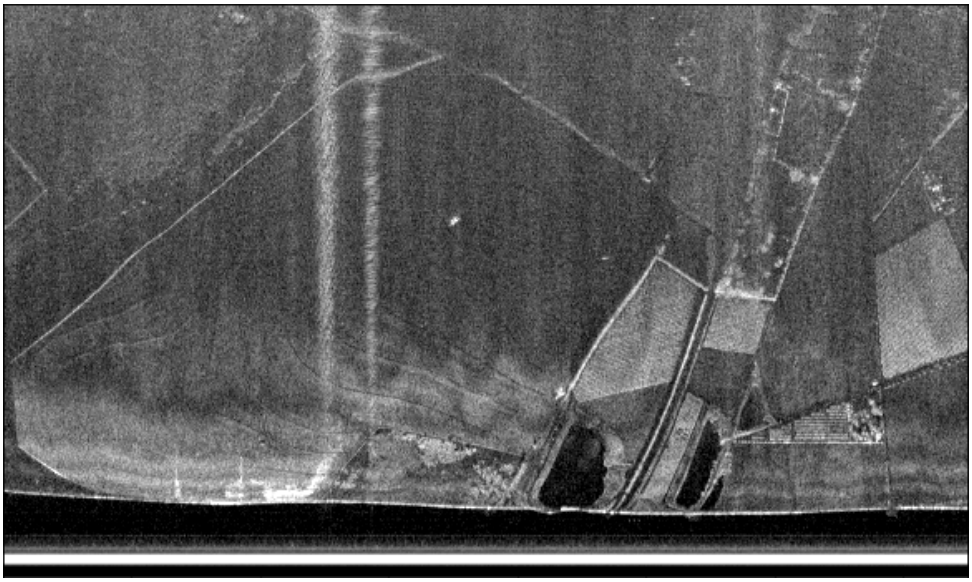

**(c)**

**Figure 6.20:** Manifestation of phase noise in miloSAR image. (a) With low phase noise, (b) with larger out-band phase noise similar to that obtained for a wide loop bandwidth, and (c) with larger in-band phase noise.

It can be seen that both high in-band and out-band phase noise result in a degradation of dynamic range and image contrast.

For the case of high out-band phase noise, shown in Figure 6.20 (b), which is the same as what would be obtained if the data had been collected with CPG = 3.1 mA, the leakage phase noise skirt is the primary cause of the image quality degradation as it adds significant noise power throughout the IF spectrum. This was observed in the context of the stationary radar detection of the corner reflectors. In addition to affecting contrast and making objects which are dark in an RCS-sense less so, this also hinders the visibility of several objects in the imaged scene.

For the Figure 6.20 (c) where in-band phase noise was increased drastically and loop bandwidth was kept small, a more slight reduction in visibility, relative to that in Figure 6.20 (b), can be seen. However, this requires an in-band phase noise much higher than it would typically be in practice.

### 6.4.4 Phase Noise Mitigation Approaches

Having demonstrated the phase noise challenges in FMCW SAR imaging, this section evaluates several strategies aimed at minimizing the phase noise or its influence in the generated images.

#### Reference Oscillator

The in-band phase noise is dominated by the phase noise of the reference oscillator; hence, if reducing in-band phase noise is a requirement, the reference oscillator should be substituted for one having lower phase noise.

Figure 6.21 shows the phase noise profiles for clocks available for use in the miloSAR.

As mentioned previously, the miloSAR makes use of the 125 MHz CXOBFBC90 clock. This can be seen to have significantly higher phase noise, at offsets below 2.5 MHz, than a readily available alternative, the 100 MHz CWX183 clock. The difference in phase noise is as much as approximately 20 dB at a 600 kHz offset. This is important because considering Figure 6.14, a reduction of phase noise by 20 dB at an offset of 600 kHz for the system operating with a CPG of 3.1 mA results in the system's phase noise profile looking similar to that of the system with a CPG of 0.1 mA. Moreover, the performance would get even better for lower loop bandwidths given the filtering characteristic of the PLL. It can also be observed that the CWX183 clock has far less spurs than the CXOBFBC90.

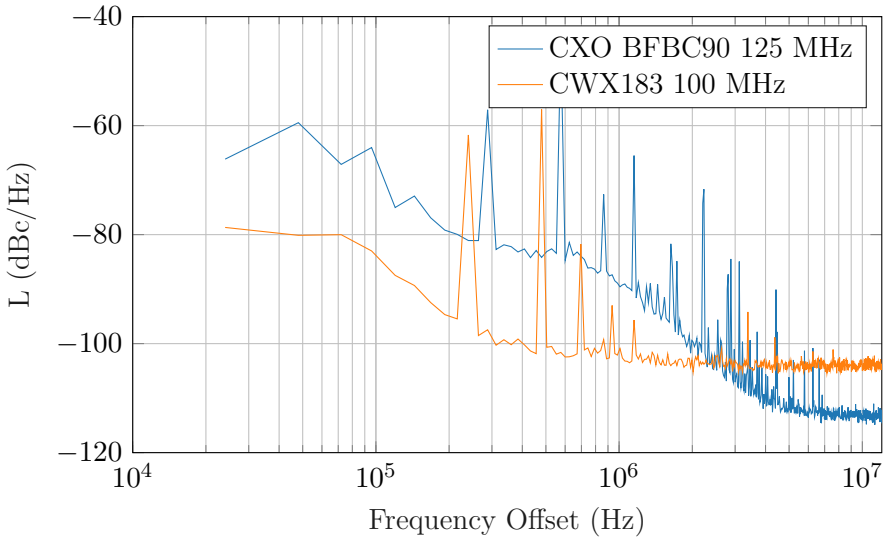


**Figure 6.21:** Phase noise of reference oscillator options available for use in the miloSAR.

While the phase noise performance of the CXOBFBC90 begins getting better than that of the CWX183 past the 2.5 MHz offset, the PLL filtering effect would be stronger by then even for large loop bandwidths.

The main caveat, however, is that all elements requiring a clock source would need to be syntonised to one clock so as to ensure the range decorrelation filtering effect. As such, a STEMlab 125-14 that accepts an external clock [79] should be used.

### Loop Bandwidth

Another method to improve phase noise of the synthesiser is by varying the loop bandwidth. The loop bandwidth has been discussed throughout this work and has been used as a means to demonstrate the distinction between high and low amounts of phase noise.

While this result has been shown already in earlier discussions, it is presented here again.

It can also be shown that a small loop bandwidth results in the suppression of more spurs; hence, it can be conclusively said that using a small loop bandwidth results in, generally, better frequency response characteristics.

However, this comes at the expense of a slower transient response which impacts such parameters as the PRF. A key objective of the waveform design process is, therefore, determining an optimal loop bandwidth for phase noise and spur suppression and acceptable dynamic parameters.

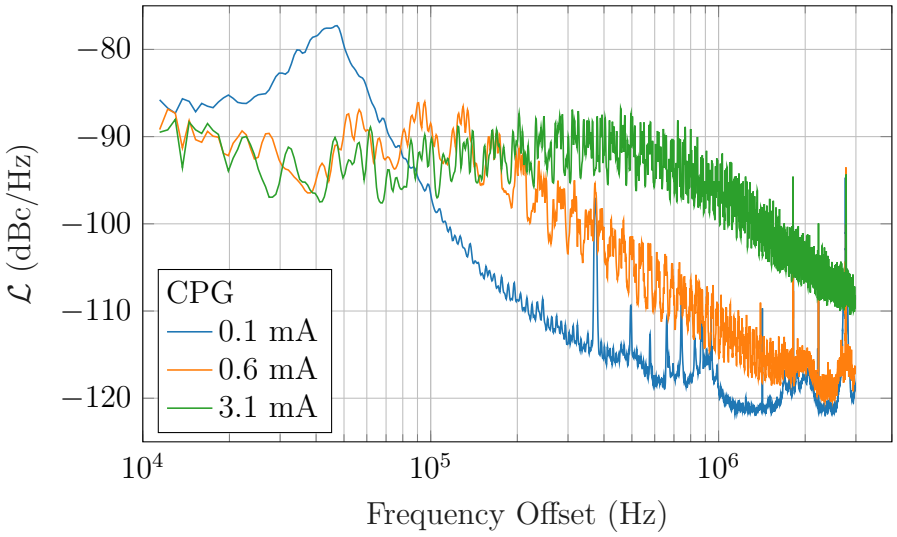


**Figure 6.22:** Phase noise of sampled IF spectrum with near zero-range return for varying loop bandwidths.

### Frequency Offset-Based Heterodyne Architecture

Range correlation filtering effects, as shown in Section 6.4.1, manifest within the PLL bandwidth. This is because the dominant source of phase noise is the reference clock, which is used for both the transmit and local oscillator synthesizers; as a result, the in-band phase noise of the synthesizers is correlated. However, outside the PLL bandwidth, the phase noise is dominated by the VCO and since two separate VCOs are required, the out-band phase noise is uncorrelated and does not cancel out after performing a mixing operation.

To explore this issue further, the system, operating in its homodyne state using a single PLL as well as using two PLLs with no time offset, was tested. The results of this exercise are as shown in Figure 6.23.

It is evident from the obtained results that range correlation filtering is a powerful means by which phase noise can be managed. Within the PLL bandwidth, the phase noise is reduced by a significant 43.5 dB from -66.5 dBc/Hz to -110 dBc/Hz. This is even more significant than the reduction observed in Section 6.4.1 because even with the same reference clock for two PLLs, the in-band phase noise is not completely correlated as there are other sources contributing to it.

The observation of interest, however, is that even at frequency offsets well outside the PLL bandwidth, the reduction of phase noise continues for the single-PLL in spite of the synthesiser having a wide loop bandwidth. Contrastingly, a sudden rise in phase noise is observed for the dual-PLL setups due to the fact that the VCO phase noise begins

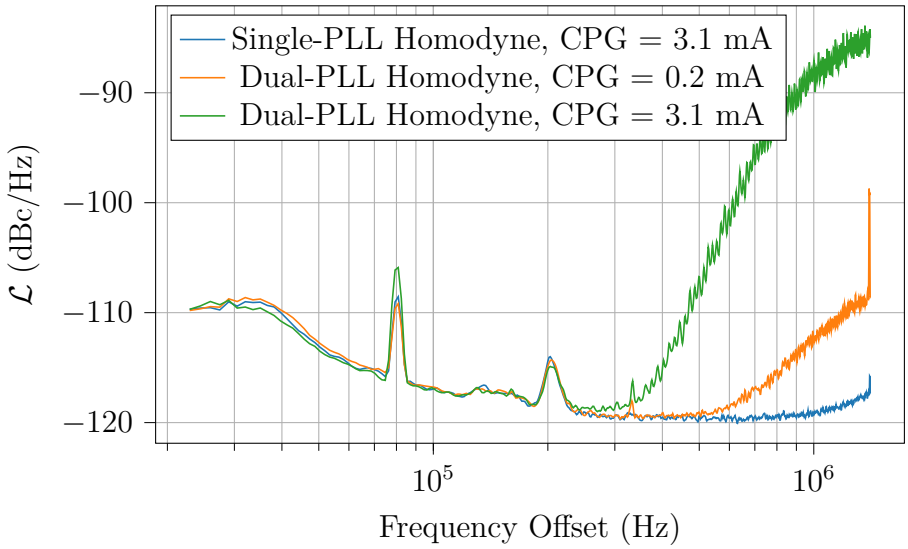


**Figure 6.23:** Comparison of phase noise of IF spectra of miloSAR operating as homodyne system with single PLL and with two PLLs having no time offset between them.

dominating and since two VCOs, having uncorrelated phase noise are being used, their phase noise combines rather than canceling out by the range correlation effect as discussed in Section 5.3.4.

This answers RQ4 by revealing that the main limitation of using a dual-PLL time offset heterodyne architecture is that the uncorrelated phase noise of the VCOs results in high levels of out-band phase noise and this noise, within the leakage signal, is detrimental to the system. One would have to use a narrower PLL bandwidth to avert it at the cost of poor PLL dynamics.

In order to circumvent this problem altogether, the following single-PLL frequency offset-based heterodyne architecture is proposed:

This architecture uses a single PLL as the source of the transmit and receive signals. The PLL output is split two-ways and one of the splitter outputs is mixed to a higher frequency by the constant frequency signal obtained directly from the 125 MHz clock. Dechirping by using the two frequency offset signals results in range correlation filtering of the phase noise in both the in-band and out-band regions due to a single PLL being used and the use of the ADC clock to achieve the frequency offset adds to the range correlation effect. Furthermore, since there is no time offset between the transmit and receive signals, this means that, for any given frequency offset, more phase noise reduction than observed with the dual-PLL system is expected.

Implementation of this architecture requires significant hardware, firmware and software

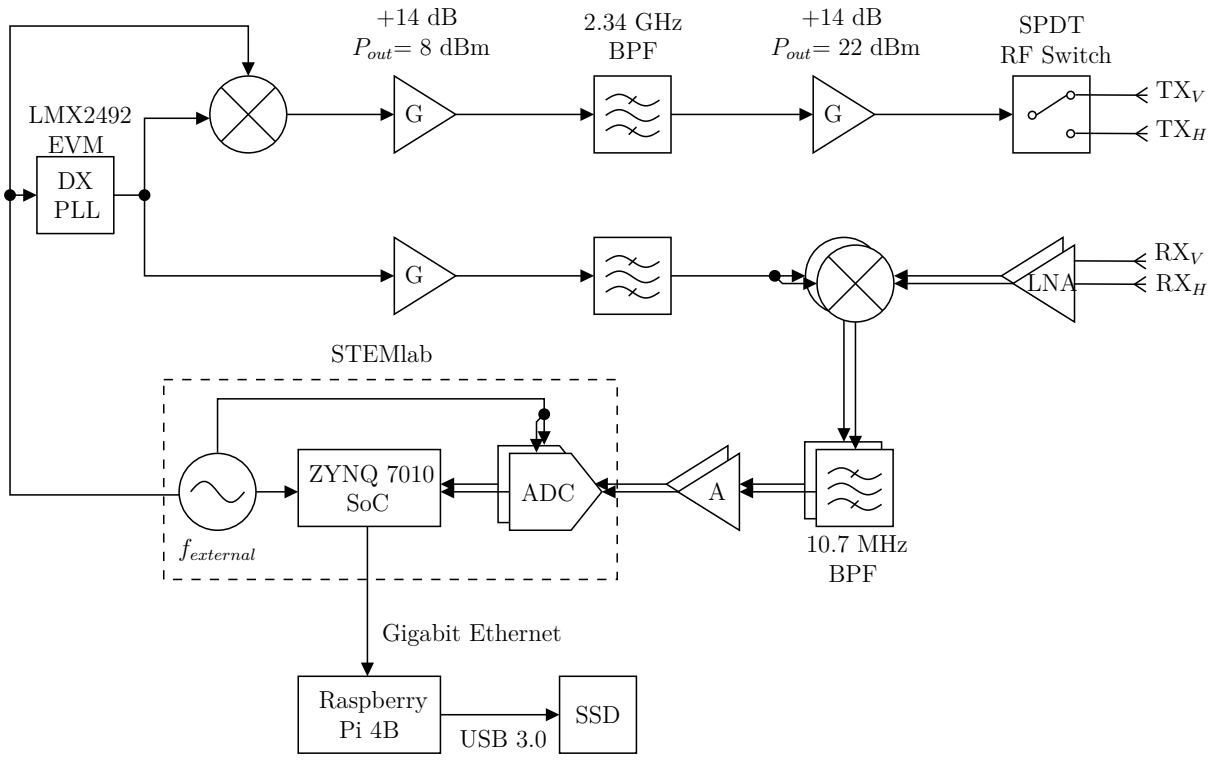


**Figure 6.24:** Frequency offset-based heterodyne architecture.

changes and is, therefore, left for future work.

## 6.5 Summary

In this chapter, tangible improvements and advancements to the system performance driven by the work conducted and documented in prior chapters have been presented. Furthermore, through various testing scenarios, a profound understanding of the system's intricacies, capabilities and limitations was obtained.

The chapter began by validating theoretical expressions to determine the maximum sweep rate and pull-in time of the synthesiser to facilitate more flexible and informed waveform design exercises and realise waveforms types such as sawtooth waveforms which were previously not achievable due to a lack of adequate knowledge about the PLL dynamics.

It was discovered the practical pull-in time constraint matched what was proposed in theory to 24% accuracy. However, the practical maximum sweep rate constraint was fairly different from the theoretical with the discrepancies being attributed to such things as modelling errors and phase noise. Instead, it was found that half the theoretical maximum sweep rate was more suitable.

Using the findings on the pull-in time, sawtooth waveforms were synthesised which was a tremendous achievement as this prevents wastage of the transmitted energy through discarding the down-ramp portion of the triangular waveform as a result of processing complexity. It was discovered, however, that this is only possible with a high CPG because with low CPG the pull-in time is so slow that the waveform will appear as an asymmetric triangular waveform. For a near-100% duty cycle, CPG = 3.1 mA should be used.

Following this, the re-implemented signal acquisition system was tested. The system was able to achieve an average maximum throughput of, 44.018 MB/s which was above 4 times the original throughput of the system at 10.925 MB/s. The increased data rate allowed for a lower decimation factor of 32 to be used which increased the bandwidth of the IF spectrum that could be sampled unambiguously from 3.125 MHz to 3.8 MHz thereby increasing the maximum unambiguous range. Additionally, the improvement in the throughput negated the need for presumming and together with increased flexibility in sweep rate and near-100% duty cycle, this allowed for higher PRFs to be used which is imperative for avoiding Doppler aliasing on fast-moving platforms. With a CPG of 3.1 mA, the PRFs of up to 250 kHz, in the fully-polarimetric mode, could be realised which is far beyond the required 2386 Hz that could not be achieved previously due to the need for longer pulses to compensate for discarded data and presumming.

The waveform parameters were then investigated, primarily, to identify areas for performance optimisation but also to determine if theoretical values can be used for design during mission planning in accordance with RQ1. This was done using the IPR obtained from a loopback test with a 100 m cable as well as using a dataset collected by the miloSAR. It was shown that a longer ramp period resulted in higher range processing gain and the value of the sawtooth waveforms was illuminated. Implementation of this waveform allowed for an increase of duty factor from 53.5% in the original system to 95.6% which increased the range processing gain. The effect of bandwidth was also studied and it was observed that a 75 MHz increase in bandwidth improves range resolution by 1.8464 m. The role of PRF was examined and it was shown that SNR improved by $10 \log N$ dB where $N$ is dependent on the PRF used. It was also demonstrated that a PRF below the Doppler bandwidth resulted in Doppler aliasing which manifested as a ghost image overlayed on top of the true image, reinforcing the arguments for deterministic behaviour when the ramp sweep rate is varied as well as for a faster signal acquisition system.

Following this set of experiments, the frequency domain behaviour of the system, specifically phase noise performance was explored.

A characterisation of the system phase noise performance was carried out and it was seen that the PLL has an average in-band phase noise level of -66.5 dBc/Hz and an average

out-band phase noise level of -115 dBc/Hz. With wider loop bandwidths, a Delta-Sigma phase noise bump is present in the phase noise profiles reaching levels of -83 dBc/Hz.

It was shown that, in the IF spectrum, range correlation filtering manifests within the PLL bandwidth because the same reference clock was used for both the transmit and local oscillator synthesisers and the ADC. At the output of the mixer, there was a 10.892 dB dB reduction in phase noise and after sampling, there was a further 12.622 dB reduction.

A test to detect corner reflectors with the radar revealed that the main challenge with phase noise in the system is related to the leakage signal whose phase noise skirt extends throughout the IF bandwidth for wide PLL bandwidths. This results in a severe deterioration of SBR with a difference of as much as 15 dB between a systems with PLL bandwidths of 2.081 MHz and 8.976 MHz. Due to taking advantage of range correlation filtering effects, the phase noise of scatterers with large RCS was made much less of a concern with the system requiring an SBR of over 65 dB for phase noise of such targets to show up.

Finally, phase noise mitigation approaches were evaluated. If in-band phase noise is a concern, it was noted that various clock sources that perform better are available as options for the miloSAR. Decreasing the loop bandwidth was also highlighted as a means by which phase noise can be reduced; however, it does so at the detriment of the PLL's dynamic performance. Finally, a single-PLL frequency-offset heterodyne architecture was proposed which takes advantage of range correlation filtering effects even in the out-band and reduces the phase noise throughout the IF spectrum by as much as 43.5 dB without sacrificing dynamic performance of the PLL.

# Chapter 7

# Conclusions and Recommendations

The research conducted in this study has effectively validated the hypothesis, demonstrating its veracity through rigorous investigation and meticulous analysis.

## 7.1 Summary of Findings

It was deduced from the simulation and integration testing results that improving the synthesised waveform does, indeed, improve SAR imaging accuracy. Presently, the key findings, in view of the research objectives, are summarised.

In Chapter 1 the main shortcomings, related to waveform synthesis, of the system in its original state were identified. These were an inability to operate with different waveform parameters and waveform types and a low throughput of 10 MB/s. The former issue resulted in use of a triangular waveform where half the signal was discarded and it was desired that the system be able to realised sawtooth waveforms with deterministic behaviour when various parameters were altered. The latter problem meant that the system could not support high PRFs; hence, it could not be deployed on the platform of choice because due to the high minimum velocity of the aircraft, Doppler aliasing would occur. Aside from addressing these and other challenges, an overarching objective of the research was to gather more knowledge about the system behaviour and find opportunities for its optimisation.

Chapters 2 and 3 were focused mainly on developing the theoretical background around the system. It was identified in Chapter 2 that other state-of-the-art FMCW SAR systems face similar challenges as the miloSAR and a significant portion of this chapter was spent looking into how other engineers tackled a variety of these challenges. An

overview of the miloSAR was presented in Chapter 3. The formulation of the relationship between throughput and other system parameters was given and the TCP/IP-based signal acquisition system implementation was presented. SAR processing was discussed and it was noted that processing gain is related to ramp duration, PRF and velocity. System performance was also discussed and it was noted the most critical metrics for target detection in the SAR image are signal-to-background ratio (SBR), resolution and sidelobe ratios. Improving these is the primary driver in SAR system design. A model for the miloSAR was also developed to facilitate rapid design and investigation of various phenomena which satisfied RO4.

Chapter 4 discussed the intricacies of fractional-N PLL-based waveform synthesis. The components that make up the LMX2492EVM PLL in the miloSAR were reviewed and different behaviours, parameter formulations, limits of linearity etc. were identified. A phase domain model for the synthesiser was generated, which also assisted in fulfilling RO4.

Using this model, the frequency response and dynamic response of the synthesiser were determined. From the frequency response, it was observed that an increase in CPG results in an increase in loop and PLL bandwidth, a result which would be used in later sections for to vary the bandwidth. From the dynamic response, the Laplace domain model was validated to be correct. The PLL was also observed to lose lock with the appearance of cycle-slips in its output in response to large frequency excursions. The details about parameter choices for FMCW SAR waveforms were also reviewed and a particularly important result was that for the Cessna 702 aircraft on which the radar was to be deployed, a PRF of 2386 Hz was required which created a specification to work toward.

Phase and frequency stability were assessed in Chapter 5 where three key concerns were identified namely, ramp non-linearity, spurs and phase noise. Ramp non-linearity of the system was found to be acceptable based on theoretical and experimental analysis and spurs were addressed, to a great extent, in the work of Jordan [2]. Phase noise was, therefore, the focus of the chapter and details of its definition, measurement, sources in and propagation through the system, simulation and so on were presented. A notable insight from this chapter was that when a mixing operation is applied on correlated phase noise, a filter appears which reduces the level of the noise. Manifestation of phase noise in FMCW SAR was also discussed with the aid of simulations and it was seen to decrease SNR and dynamic range thereby hindering visibility of some targets in the image and degrading image contrast.

The ideas and concepts explored in the chapters prior were brought together and applied

to the real system in Chapter 6. Several important discoveries were made and performance improvements were observed. These are summarised extensively in Section 6.5 and will not be replicated here.

## 7.2 Research Questions

In Chapter 1, some research questions were posed. These are answered presently.

1. **RQ1:** How does the theory on FMCW radar design match up with practical systems? Can theoretically predicted parameters be relied on for system design?

   For the most part and to some acceptable degree of accuracy, theoretical predictions for system parameters required to meet certain specifications match up with the real values required. The value of maximum sweep rate was the only one that was seen to deviate significantly from what was obtained from theoretical principles. It was found that half the predicted maximum sweep rate was what was required to operate the synthesisers without incurring non-linearities. Therefore, with testing and suitable calibrations, and by factoring in the appropriate safety margins, theoretically computed system parameters can be used directly for system design.

2. **RQ2:** What is the relationship between dynamic response characteristics and frequency response characteristics of the synthesiser and how do these affect the generated waveforms?

   It was observed that a wider PLL bandwidth, achieved through increasing the CPG, resulted in faster transient responses of the PLL but less spectral purity of the synthesised signal. Both the PLL lock and pull-in times were considerably lower for CPG = 3.1 mA than CPG = 0.1 mA. This had implications in realisation of waveforms such as sawtooth waveforms as, for CPG = 0.1 mA, the pull-in time was so slow that the synthesised waveform appeared as an asymmetric ramp waveform rather than a sawtooth waveform and the sawtooth waveform with maximum duty cycle of 96.0% which implies maximum processing gain was achieved with CPG = 3.1 mA. However, observing the phase noise profiles of the synthesised signals revealed that the wider PLL bandwidth resulted in the cutoff frequency of the low-passing PLL filtering frequency response increasing; hence, more phase noise and spurs were allowed to pass through unfiltered.

3. **RQ3:** Phase noise is widely reported to be a major problem in radar systems. To what extent is it a concern in FMCW SAR and how much should it drive the design process?

Phase noise was proven to be a major concern for FMCW SAR systems which can cause devastating image quality loss. Specifically, the phase noise skirt of the leakage signal is problematic because it is very high in power and, for wide PLL bandwidths, it extends throughout the entire IF spectrum drastically increasing the SBR and covering targets of interest. Due to the manifestation of range correlation filtering, phase noise of strong targets within the scene was deemed to be less of a concern as the in-band phase noise was reduced to the level of the out-band phase noise. For it to be visible in the SAR image, very high values of SCR would be required for the strong target.

4. **RQ4:** What are the performance limitations of a time-offset heterodyne architecture as it relates to waveform synthesis?

   Following on from the previous discussion, for the dual-PLL time-offset heterodyne architecture, this means that the PLL cannot be used with wide bandwidths, which means that efficient waveforms such as the sawtooth waveform cannot be used as efforts to improve processing gain by increasing duty cycle would only be in vain and counteracted by the phase noise. Other architectures such as the proposed dual-PLL, frequency-offset heterodyne architecture must be explored.

## 7.3 Recommendations

A number of recommendations are made for future waveform design procedures and design iterations of the the system.

- Given the volume of parameters required for system configuration and the conflicting relationships between several of them, it would be highly beneficial to write an optimisation algorithm to determine their values.
- Phase noise mitigation techniques have been proposed in Section 6.4.4. Redesigning the architecture to become a frequency-offset heterodyne system using a single PLL for the transmit and local oscillator signal offers great promise for reduction of the leakage phase noise skirt through range correlation filtering.
- The Raspberry Pi used in the signal acquisition system is a power-hungry device running a full operating system and other features that are not necessary. Instead, replacing it with a microcontroller capable of interfacing with Ethernet is a more efficient solution.

- Using an active loop filter allows for a drastic improvement of range resolution by increasing the bandwidth and should be considered along with other techniques such as adaptive windowing functions that can improve PSR without affecting the resolution.

# Appendices

# Appendix A

# SAR Model

The basis of the current work is the FMCW SAR signal model. It describes how the synthesised waveform interacts with a point scatterer in the scene of interest and how the energy reflected by the object back to the radar system is manipulated to represent the object's properties.

As such, this model is used in this work to drive the design decisions, to explain certain results and for simulation of the SAR system. Furthermore, system imperfections such as phase noise, fundamentally, alter the signal from the ideal or assumed case and their impact can be understood via the signal model.

## A.1 Transmit Signal

An FMCW radar system transmits a frequency ramp signal, otherwise known as a chirp signal, which, in its analytic[1] form is expressed

$$x_{TX}(t) = \text{rect}\left(\frac{t}{T_r}\right) A \exp(j(2\pi f_0 t + \pi k_r t^2 + \phi_0)) \tag{A.1}$$

where

$$\text{rect}\left(\frac{t}{T_r}\right) = \begin{cases} 1 & |t| \leq T_r/2, \\ 0 & \text{else} \end{cases} \tag{A.2}$$

and

[1] An analytic signal is a complex-valued representation of a signal, having no negative frequency components and comprised of the original function and its Hilbert transform.

$t$ is the fast-time variable,
$f_0$ is the center frequency of the transmitted band of frequencies,
$T_r$ is the ramp's modulation period,
$A$ is the nominal amplitude of the transmitted ramp,
$\phi_0$ is the nominal phase of the chirp, and
$k_r$ is ramp sweep rate (chirp rate) given by

$$k_r = \frac{B_r}{T_r} \tag{A.3}$$

with $B_r$ being the modulation bandwidth of the ramp.

In the interest of avoiding mathematical clutter, the truncation term, amplitude term and initial phase are dropped in the rest of this work save for where they are significant in the discussion.

## A.2 Receive Signal

A scatterer reflects the transmitted signal to the radar system such that the signal at the receive antenna is a delayed and attenuated replica of the transmitted. Time delay $\tau_d$ between transmitting a signal and receiving the echo is directly proportional to slant range of the scatterer, $R$, and is approximated by

$$\tau_d = \frac{2R}{c} \tag{A.4}$$

In traditional pulsed systems, the stop-and-go approximation (SAG) is applied for simplicity, which assumes that the radar is stationary while it transmits and captures a pulse before moving to the next azimuth location. FMCW systems, however, employ very long pulses and SAG is no longer an acceptable approximation. Instead, change in platform position is accounted for within the pulse and the scatterer's is approximated by [7], [80]

$$R(t, t_a) = \sqrt{R_0^2 + v^2(t_a + t - t_{a_0})^2} \tag{A.5}$$

where $R_0$ is the minimum range during acquisition from the scatterer to antenna's phase center, $v$ is the platform velocity and $t_a$ is azimuth time, sampled at the pulse repetition frequency (PRF).

The reflected echo of the transmitted signal by an isotropic target at range $R(t, t_a)$ is,

thus, represented by

$$x_{RX}(t, t_a) = \sigma(R_0, \tau_{d_0})\, x_{TX}(t - \tau_d) \tag{A.6}$$
$$= \sigma(R_0, \tau_{d_0}) \exp(j(2\pi f_0(t - \tau_d) + \pi k_r(t - \tau_d)^2)) \tag{A.7}$$

where $\sigma(R_0, \tau_{d_0})$ is the reflection coefficient.

## A.3 Intermediate Frequency Signal

Demodulation is then performed on the received signal which, in a majority of FMCW systems including the miloSAR, is done by use of a technique known as 'stretch-processing' or 'dechirp-on-receive'.

This refers to mixing the received echo with a reference signal which is, itself, a frequency ramp signal, expressed as

$$x_{LO}(t) = \exp(j(2\pi f_0 t + \pi k_r t^2)) \tag{A.8}$$

and low pass filtering the mixer output such that a constant frequency sinusoid is obtained, thereby reducing sampling and data rate requirements.

The dechirp and filtering operation is the equivalent of multiplication of the reference signal with the complex conjugate of the received signal [2] which results in the intermediate frequency (IF) or beat signal

$$X_{IF}(t, t_a) = x_{LO}(t) x^*_{RX}(t, t_a) \tag{A.9}$$
$$= \exp(j(2\pi f_0 \tau_d + 2\pi k_r t \tau_d - \pi k_r \tau_d^2)) \tag{A.10}$$

The last term in Equation A.10 is the so-called residual video phase (RVP). The rest of the signal model analysis assumes the RVP has been removed.

Defining the range spatial frequency, $\eta_r$, as

$$\eta_r = \frac{4\pi}{c} k_r \left( \frac{f_0}{k_r} + t \right) \tag{A.11}$$

[2] Or multiplication of the complex conjugate of the reference signal with the received signal.

and azimuth position, $x$, as

$$x = vt_a \tag{A.12}$$

and substituting both, as well as the expression of $R(t, \tau_d)$ into Equation A.10, along with some further algebraic rearrangements, the intermediate frequency signal can be re-written as

$$\exp(j\eta_r\sqrt{R_0^2 + (x + vt - x_0)^2}) \tag{A.13}$$

## A.4 2D Frequency Spectrum

In terms of signal model analysis, the expression for $X_{IF}$ in Equation A.10 is considered to already be in the range spectrum domain; therefore, only an Fourier Transform with respect to the azimuth axis variable is required to obtain the 2D spectrum.

The mathematical result of this Fourier Transform solved by the Principle of Stationary Phase (POSP) is

$$X_{IF}(\eta_r, \eta_x) = \exp\left(j\eta_x vt\right) \exp\left(jR\sqrt{\eta_r^2 - \eta_x^2} - j\eta_x x_0\right) \tag{A.14}$$

where $\eta_x$ is the azimuth spatial frequency.

# Appendix B

# Range-Doppler Algorithm

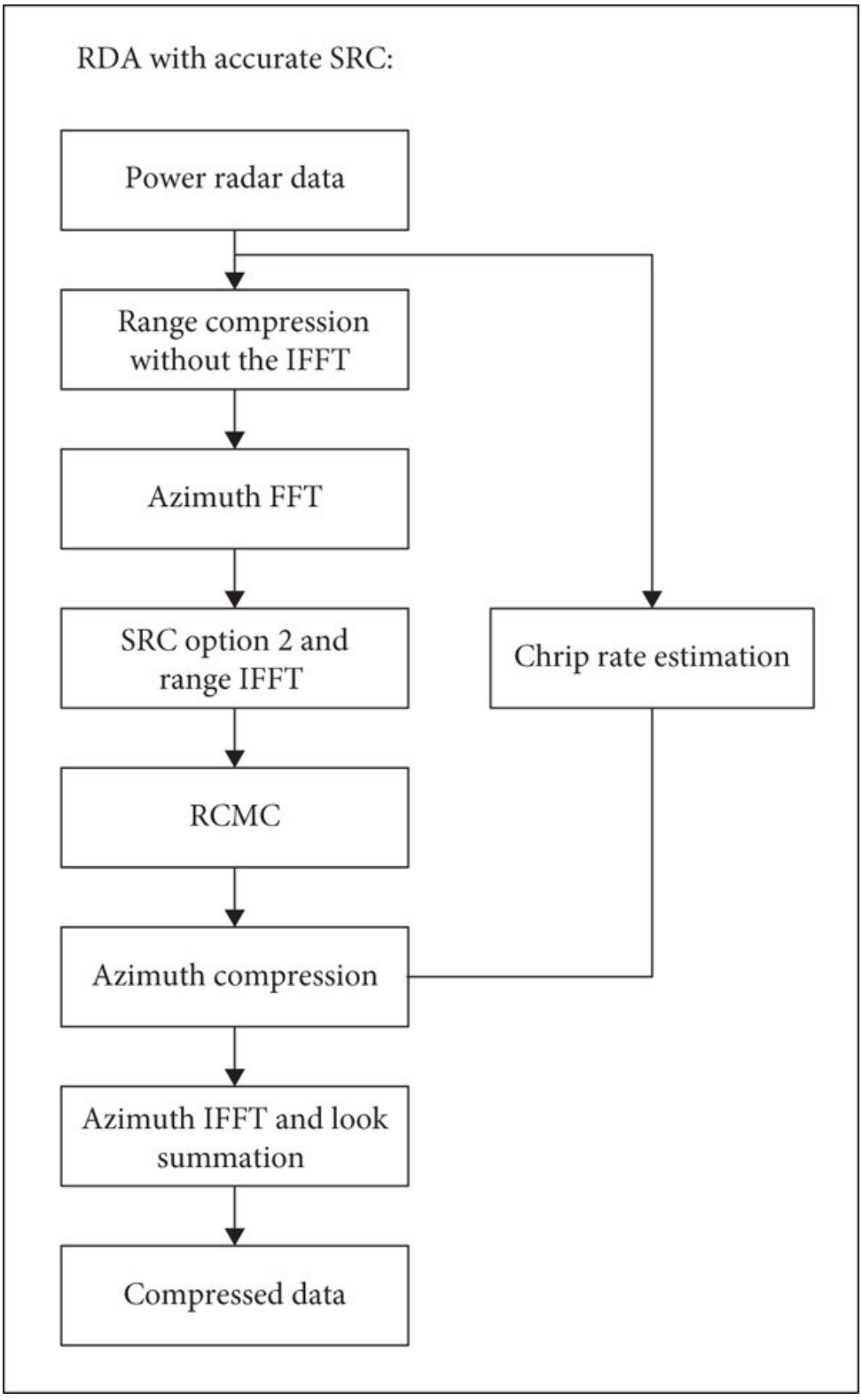


**Figure B.1:** Range-Doppler algorithm flow diagram

# Appendix C

# FMCW SAR Simulation

```
%%%%%%%%%%%%%%%%%%%%%%%%%%%%%%%%%%%%%%%%%%%%%%%%%%%%%%%%%%%%%%%%%%%%%%%%%%%%
%
% File: fmcwSARSim.m
% Author: Thomas Gwasira
% Date: Oct, 2022
%
% FMCW SAR simulation.
%
% The signal model is based on [1 - 3].
%
% References:
% [1] Yang, J. (2017). GMTI and GMTIm in FMCW SAR. In: Study on Ground
%     Moving Target Indication and Imaging Technique of Airborne SAR
% [2] Li, Y.; O'Young, S. Focusing Bistatic FMCW SAR Signal by Range
%     Migration Algorithm Based on Fresnel Approximation. Sensors ...
    2015, 15,
%     32123-32137. https://doi.org/10.3390/s151229910
%%%%%%%%%%%%%%%%%%%%%%%%%%%%%%%%%%%%%%%%%%%%%%%%%%%%%%%%%%%%%%%%%%%%%%%%%%%%


%%%%%%%%%%%%%%%%%%%%%%%%%%%%%%%%%%%%%%%%%%%%%%%%%%%%%%%%%%%%%%%%%%%%%%%%%%%%
%% Simulation Parameters
%%%%%%%%%%%%%%%%%%%%%%%%%%%%%%%%%%%%%%%%%%%%%%%%%%%%%%%%%%%%%%%%%%%%%%%%%%%%
c = physconst('LightSpeed');

% --------------------
% Waveform Parameters
% --------------------
fc = 2.4e9;                     % Carrier frequency (Hz)
```

```
29 lambda = c/fc;                % Carrier wavelength (m)
30 BW = 175e6;                    % FMCW chirp bandwidth (Hz)
31 PRF = 1000;                   % FMCW waveform effective PRF (Hz)
32 Tp = 1/PRF;                   % FMCW chirp period. Take up whole PRF. (s)
33 fADC = 2*BW;                  % ADC sample rate. Depends on beat ...
       spectrum.
34 tauc = 0;                     % Time delay of reference signal (s) [1]
35 delR = c/(2*BW);              % Range resolution (m)
36
37 Pt = (10^(22/10))/1000 ;      % Peak transmit power (W)
38 Z = 50;                       % System impedance (Ohms)
39
40 % ------------------
41 % Antenna Parameters
42 % ------------------
43 Daz = 10e-2;                  % Physic antenna aperture size in ...
       azimuth (m)
44 azBeamwidth = lambda/Daz;     % Azimuth beamwidth of physical antenna ...
       (rad)
45
46
47 % Antenna Isolation
48 Rft = 5;                      % Range of feedthrough (m)
49 tdft = 2*Rft/c;               % Time delay for feedthrough (s)
50
51 % ----------------------
52 % Acquisition Parameters
53 % ----------------------
54 v0 = 50;
55 height = 10;
56 flightDuration = 3;
57
58 % ------------
59 % Time Vectors
60 % ------------
61 t = -Tp/2:1/fADC:Tp/2;        % Fast time
62 Tp = 2*max(t);     % Actual chirp duration based on fast-time vector (s)
63 kr = BW/Tp;                   % Chirp rate (Hz/s)
64
65 tau = -flightDuration/2:1/PRF:flightDuration/2; % Azimuth time [3]
66 nPulses = length(tau);
67
68
69 % -------------------
70 % Sampling Parameters
71 % -------------------
```

```
% Truncate the fast time samples to get less data at expense of dechirp
% resolution
truncate = 70000;


% ----------
% IQ Metrics
% ----------


% -------
% Targets
% -------
% Format: [x1, y1, 0, sigma1; x2, y2, 0, sigma2]
targets = [75, 250, 0, 1;];
% targets = [75, 600, 0, 1; 45, 600, 0, 1; 65, 600, 0, 1; 85, 600, ...
    0, 1; 105, 600, 0, 1; 75, 700, 0, 0.5; 75, 900, 0, 0.5; 75, 1300, ...
    0, 0.5;];
% targets = [75, 2000, 0, 1;75, 1000, 0, 1;];

% -----------
% Phase Noise
% -----------
withPn = true;


%%%%%%%%%%%%%%%%%%%%%%%%%%%%%%%%%%%%%%%%%%%%%%%%%%%%%%%%%%%%%%%%%%%%%%%%%%%
%% Transmit and Receive Signal
%%%%%%%%%%%%%%%%%%%%%%%%%%%%%%%%%%%%%%%%%%%%%%%%%%%%%%%%%%%%%%%%%%%%%%%%%%%
srx = zeros(truncate,nPulses);
sref = zeros(truncate,nPulses);

Atarg = zeros(1, nPulses);

for n = 1:nPulses
    taun = tau(n);
    vtaun = v0;

    if withPn
        % Obtain phase noise for pulse
        pn1 = ones(length(t), 1);
        pn1 = phaseNoise(pn1);

        pn2 = ones(length(t), 1);
        pn2 = phaseNoise(pn2);
    end
```

```
116
117     % Create range reference function for dechirp
118     if ¬withPn
119         srefProfile = fmcwChirp(BW, Tp, fADC, t, fc, 0, 0);
120     else
121         srefProfile = pn1.*fmcwChirp(BW, Tp, fADC, t, fc, 0, 0);
122     end
123
124     sref(:,n) = srefProfile(1:truncate);
125
126     for ti = 1:size(targets, 1)
127         x = targets(ti,1);
128         y = targets(ti,2);
129         z = targets(ti,3);
130         sigma = targets(ti,4);
131
132         % TODO: Compute azimuth time at Doppler minimum from Catesian
133         % coordinates
134         tau0 = x/v0 - flightDuration/2; % must use fixed velocity ...
                can't be moving around
135
136         % Compute target range at Doppler minimum from Catesian ...
                coordinates
137         R0 = sqrt(y^2 + height^2);
138
139         % Compute time delay without SAG
140         taun_t = taun + t - tau0; % [3]
141         R = sqrt(R0^2 + (vtaun^2)*(taun_t.^2));
142         td = 2*R/c;
143
144         % Compute antenna pattern weighting factor
145         A = sinc((Daz/lambda)*atan(v0*taun/R0))^2;
146         Atarg(n) = A;
147
148         % tpnShift = mean(td);
149         % spnShift = floor(tpnShift * fADC);
150         % pn2 = circshift(pn1, 100);
151
152         % Get echo and accumulate into matrix of echos
153         if ¬withPn
154             srxTarget = Pt*sigma*A*fmcwChirp(BW, Tp, fADC, t - td, ...
                    fc, 0, 0);
155         else
156             srxTarget = Pt*sigma*A*(pn2.*fmcwChirp(BW, Tp, fADC, t - ...
                    td, fc, 0, 0)); % IP: Phase Noise
157         end
```

```
158
159         srx(:,n) = srx(:,n) + srxTarget(1:truncate);
160
161         % Feedthrough
162         % feedthrough = fmcwChirp(BW, Tp, fADC, t - tdft, fc, 0, 0);
163         % feedthrough = pn2.*fmcwChirp(BW, Tp, fADC, t - tdft, fc, ...
                0, 0);
164         % srx(:,n) = srx(:,n) + feedthrough(1:truncate);
165     end
166 end
167
168
169 %%%%%%%%%%%%%%%%%%%%%%%%%%%%%%%%%%%%%%%%%%%%%%%%%%%%%%%%%%%%%%%%%%%%%%%%
170 %% Dechirp
171 %%%%%%%%%%%%%%%%%%%%%%%%%%%%%%%%%%%%%%%%%%%%%%%%%%%%%%%%%%%%%%%%%%%%%%%%
172 disp('Performing dechirp')
173
174 % Reference signal for dechirp. NOTE: Azimuth is along rows.
175 % TODO: Delete this
176 % sref = fmcwChirp(BW, Tp, fADC, t, fc, 0, 0);
177 % sref = sref(1:truncate);
178 % sref = repmat(sref, 1, nPulses);
179
180 % Dechirp
181 sdx = sref.*conj(srx);
182
183 % IP: Add White Gaussian Noise to dechirped signal
184 % TODO: Sort out noise floor properly.
185 % sdx = awgn(sdx,10);
186
187 clear srxTarget;
188 clear srx;
189 clear sref;
190
191
192 %%%%%%%%%%%%%%%%%%%%%%%%%%%%%%%%%%%%%%%%%%%%%%%%%%%%%%%%%%%%%%%%%%%%%%%%
193 %% Windowing
194 %%%%%%%%%%%%%%%%%%%%%%%%%%%%%%%%%%%%%%%%%%%%%%%%%%%%%%%%%%%%%%%%%%%%%%%%
195 disp("Applying window function")
196
197 % Taylor
198 wProfile = hann(size(sdx, 1));
199 w = repmat(wProfile, 1, nPulses);
200 sdx = sdx.*w;
201
202 clear wProfile;
```

```
203 clear w;
204
205
206 %%%%%%%%%%%%%%%%%%%%%%%%%%%%%%%%%%%%%%%%%%%%%%%%%%%%%%%%%%%%%%%%%%%%%%%%%%%%
207 %% Range Compression
208 %%%%%%%%%%%%%%%%%%%%%%%%%%%%%%%%%%%%%%%%%%%%%%%%%%%%%%%%%%%%%%%%%%%%%%%%%%%%
209 disp('Performing range compression')
210
211 rcData = fftshift(fft(sdx, 120000)); % do not do an fftshift
212 % imagesc(10*log10(abs(fftshift(rcData))));
213
214 rcFFTSize = size(rcData, 1); % same as truncate if not changed in fft
215 frcData = (-rcFFTSize/2:rcFFTSize/2-1)*fADC/rcFFTSize;
216 range = Tp/BW * c/2 * frcData;
217
218 % figure()
219 % imagesc(tau, range, 10*log10(abs(rcData)));
220 % xlabel("Azimuth (m)")
221 % ylabel("Range (m)")
222 % title("Range Compressed Data")
223
224 clear sdx;
225
226
227 %%%%%%%%%%%%%%%%%%%%%%%%%%%%%%%%%%%%%%%%%%%%%%%%%%%%%%%%%%%%%%%%%%%%%%%%%%%%
228 %% RVP Compensation
229 %%%%%%%%%%%%%%%%%%%%%%%%%%%%%%%%%%%%%%%%%%%%%%%%%%%%%%%%%%%%%%%%%%%%%%%%%%%%
230 disp('Applying RVP compensation')
231
232 % TODO: Come back and have a re-look at this
233 HRVPProfile = exp(1i*pi*(frcData.^2)/kr).';
234 HRVP = repmat(HRVPProfile, 1, nPulses);
235 rcData = rcData.*HRVP;
236
237 % Crop RVP compensated range compressed data
238 maxRangeSamples = 540; % TODO: Evaluate this from actual maxrange
239 rcData = rcData(rcFFTSize/2:rcFFTSize/2+maxRangeSamples,:);
240 range = range(rcFFTSize/2:rcFFTSize/2+maxRangeSamples);
241
242 figure()
243 imagesc(tau, range, 10*log10(abs(rcData)));
244 xlabel("Azimuth (m)")
245 ylabel("Range (m)")
246 title("RVP Compensated Range Compressed Data")
247
248 clear HRVPProfile;
```

```
249 clear HRVP;
250
251
252 %%%%%%%%%%%%%%%%%%%%%%%%%%%%%%%%%%%%%%%%%%%%%%%%%%%%%%%%%%%%%%%%%%%%%%%%%%%%
253 %% range-Doppler Domain
254 %%%%%%%%%%%%%%%%%%%%%%%%%%%%%%%%%%%%%%%%%%%%%%%%%%%%%%%%%%%%%%%%%%%%%%%%%%%%
255 disp('Performing conversion to range-Doppler domain')
256
257 rdData = (fft(rcData, [], 2));
258 rdData = fftshift(rdData, 2); % note dimension
259
260 rdFFTSize = size(rdData, 2); % same as truncate if not changed in fft
261 frdData = (-rdFFTSize/2:rdFFTSize/2-1)*PRF/rdFFTSize;
262
263 figure()
264 imagesc(tau, range, 10*log10(abs(rdData)));
265 xlabel("Azimuth (m)")
266 ylabel("Range (m)")
267 title("Range-Doppler Map")
268
269
270
271 %%%%%%%%%%%%%%%%%%%%%%%%%%%%%%%%%%%%%%%%%%%%%%%%%%%%%%%%%%%%%%%%%%%%%%%%%%%%
272 %% Azimuth Reference Function
273 %%%%%%%%%%%%%%%%%%%%%%%%%%%%%%%%%%%%%%%%%%%%%%%%%%%%%%%%%%%%%%%%%%%%%%%%%%%%
274 ha = zeros(length(range),nPulses);
275
276 for rangei = 1:length(range)
277     R0 = range(rangei);
278     ha(rangei,:) = exp(1i * (((2*pi*v0^2)/(lambda*R0)) * tau.^2 - ...
            ((4*pi*v0^2)/(lambda*c)) * tau)); % [Stringham]
279 %     ha(rangei,:) = exp(1i * pi * ((2*v0^2)/(lambda*R0)) * tau.^2); ...
        % [GMTI book] not conjugated yet
280 end
281
282 Ha = fftshift(fft(ha, [], 2), 2); % Note dimension
283
284
285 %%%%%%%%%%%%%%%%%%%%%%%%%%%%%%%%%%%%%%%%%%%%%%%%%%%%%%%%%%%%%%%%%%%%%%%%%%%%
286 %% Azimuth Compression
287 %%%%%%%%%%%%%%%%%%%%%%%%%%%%%%%%%%%%%%%%%%%%%%%%%%%%%%%%%%%%%%%%%%%%%%%%%%%%
288 disp("Performing azimuth compression")
289
290 img = 10*log10(abs(ifft(rdData.*conj(Ha), [], 2)));
291
292 figure()
```

```
293 imagesc(tau*v0, range, img)
294 xlabel("Azimuth Position (m)")
295 ylabel("Range (m)")
296 title("Azimuth Compressed SAR Image")
297
298 % Crop SAR image in range
299 maxImgRangeSamples = 210; % TODO: Evaluate this from actual maxrange
300 imgCropped = img(1:maxImgRangeSamples,:);
301 rangeCropped = range(1:maxImgRangeSamples);
302
303 %%%%%%%%%%%%%%%%%%%%%%%%%%%%%%%%%%%%%%%%%%%%%%%%%%%%%%%%%%%%%%%%%%%%%%%%%%%
304 %% Save Data
305 %%%%%%%%%%%%%%%%%%%%%%%%%%%%%%%%%%%%%%%%%%%%%%%%%%%%%%%%%%%%%%%%%%%%%%%%%%%
306 save("largerPnT1.mat");
```

# Appendix D

# Loop Filter Coefficients

**Table D.1:** Filter coefficients for passive loop filters [52].

| Filter Order | Symbol | Filter Coefficient Calculation |
|---|---|---|
| 2 | $a_0$ | $C1 + C2$ |
| | $a_1$ | $C1 \cdot C2 \cdot R2$ |
| | $a_2$ | 0 |
| | $a_3$ | 0 |
| 3 | $a_0$ | $C1 + C2 + C3$ |
| | $a_1$ | $C2 \cdot R2 \cdot (C1 + C3) + C3 \cdot R3 \cdot (C1 + C2)$ |
| | $a_2$ | $C1 \cdot C2 \cdot C3 \cdot R2 \cdot R3$ |
| | $a_3$ | 0 |
| 4 | $a_0$ | $C1 + C2 + C3 + C4$ |
| | $a_1$ | $C2 \cdot R2 \cdot (C1 + C3 + C4) + R3 \cdot (C1 + C2) \cdot (C3 + C4) + C4 \cdot R4 \cdot (C1 + C2 + C3)$ |
| | $a_2$ | $C1 \cdot C2 \cdot R2 \cdot R3 \cdot (C3 + C4) + C4 \cdot R4 \cdot (C2 \cdot C3 \cdot R3 + C1 \cdot C2 \cdot R2 + C2 \cdot C3 \cdot R2)$ |
| | $a_3$ | $C1 \cdot C2 \cdot C3 \cdot C4 \cdot R2 \cdot R3 \cdot R4$ |

**Table D.2:** Filter coefficients for active loop filters [52].

| **Filter Order** | **Symbol** | **Filter Coefficient Calculation** |
|---|---|---|
| 2 | $a_0$ | $C2$ |
| | $a_1$ | $C1 \cdot C2 \cdot R1$ |
| | $a_2$ | 0 |
| | $a_3$ | 0 |
| 3 | $a_0$ | $C2$ |
| | $a_1$ | $C2 \cdot (C1 \cdot R1 + C3 \cdot R3)$ |
| | $a_2$ | $C1 \cdot C2 \cdot C3 \cdot R1 \cdot R3$ |
| | $a_3$ | 0 |
| 4 | $a_0$ | $C2$ |
| | $a_1$ | $C2 \cdot (C1 \cdot R1 + C3 \cdot R3 + C4 \cdot R4 + C4 \cdot R3)$ |
| | $a_2$ | $C1 \cdot C2 \cdot R1 \cdot (C3 \cdot R3 + C4 \cdot R4 + C4 \cdot R3) + C2 \cdot C3 \cdot C4 \cdot R3 \cdot R4$ |
| | $a_3$ | $C1 \cdot C2 \cdot C3 \cdot R1 \cdot R3 \cdot R4$ |

# Bibliography


[1] I. Tchekashkin, "Design and implementation of a low-cost fmcw imaging radar," M.S. dissertation, Dept. of Elec. Eng., University of Cape Town, Cape Town, South Africa, 2015. [Online]. Available: https://open.uct.ac.za/handle/11427/24299.

[2] D. Jordan, "Time-offset fractional-n plls for heterodyne fmcw sar," Ph.D. dissertation, Dept. of Elec. Eng., University of Cape Town, Cape Town, South Africa, 2021. [Online]. Available: https://hdl.handle.net/11427/33820.

[3] *Lmx2492 evaluation instructions ultra low noise frequency synthesizer with integrated vco evaluation board operating instructions*, LMX2492 SNAU160C, Revised November 2014, Texas Instruments Incorporated, Mar. 2014.

[4] M. Jankiraman, *FMCW Radar Design* (Artech House radar library). Artech House, 2018, ISBN: 9781630815677. [Online]. Available: https://books.google.co.za/books?id=TvX0tQEACAAJ.

[5] J. Park, S. Park, D.-H. Kim, and S.-O. Park, "Leakage mitigation in heterodyne fmcw radar for small drone detection with stationary point concentration technique," *IEEE Transactions on Microwave Theory and Techniques*, vol. 67, no. 3, pp. 1221–1232, 2019. DOI: 10.1109/TMTT.2018.2889045.

[6] P. Beasley, A. Stove, B. Reits, and B. As, "Solving the problems of a single antenna frequency modulated cw radar," in *IEEE International Conference on Radar*, 1990, pp. 391–395. DOI: 10.1109/RADAR.1990.201197.

[7] A. Meta, "Signal processing of fmcw synthetic aperture radar data," Ph.D. dissertation, Delft University of Technology, Delft, Netherlands, Oct. 2006. [Online]. Available: https://repository.tudelft.nl/islandora/object/uuid:24352ff9-c11a-46c9-87d4-4d9d8968ed81/datastream/OBJ/download.

[8] J. Yang, *Study on Ground Moving Target Indication and Imaging Technique of Airborne SAR*. Singapore: Springer Singapore, 2017, p. 16, ISBN: 978-981-10-3075-8. DOI: 10.1007/978-981-10-3075-8_5. [Online]. Available: https://doi.org/10.1007/978-981-10-3075-8%5C_5.

[9] S. Rao and A. V. Mani, "Interference characterization in fmcw radars," in *2020 IEEE Radar Conference (RadarConf20)*, 2020, pp. 1–6. DOI: 10.1109/RadarConf2043947.2020.9266283.

[10] M. Edrich, "Design overview and flight test results of the miniaturised sar sensor misar," in *First European Radar Conference, 2004. EURAD.*, 2004, pp. 205–208.

[11] M. Mahdi, H. Tork, A. A. Eltager, and M. Darwish, "X-band transmitter leakage canceller for fmcw radar applications," in *2021 IEEE Radio and Wireless Symposium (RWS)*, 2021, pp. 151–153. DOI: 10.1109/RWS50353.2021.9360384.

[12] A. Melzer, A. Onic, F. Starzer, and M. Huemer, "Short-range leakage cancelation in fmcw radar transceivers using an artificial on-chip target," *IEEE Journal of Selected Topics in Signal Processing*, vol. 9, no. 8, pp. 1650–1660, 2015. DOI: 10.1109/JSTSP.2015.2465298.

[13] F. O'hara and G. Moore, "A high performance cw receiver using feedthru nulling," *Microwave Journal*, vol. 6, no. 9, pp. 63–71, 1963.

[14] K. Lin, Y. E. Wang, C.-k. Pao, and Y.-C. Shih, "A ka-band fmcw radar front-end with adaptive leakage cancellation," *IEEE Transactions on Microwave Theory and Techniques*, vol. 54, pp. 4041–4048, 2006.

[15] K. Kulpa, "Focusing range image in vco based fmcw radar," in *2003 Proceedings of the International Conference on Radar (IEEE Cat. No.03EX695)*, 2003, pp. 235–238. DOI: 10.1109/RADAR.2003.1278745.

[16] J. Fuchs, K. Ward, M. Tulin, and R. York, "Simple techniques to correct for vco nonlinearities in short range fmcw radars," vol. 2, Jul. 1996, 1175–1178 vol.2. DOI: 10.1109/MWSYM.1996.511239.

[17] D. J. Weyer, "Design of digital fmcw chirp synthesizer plls using continuous-time delta-sigma time-to-digital converters," Ph.D. dissertation, University of Michigan, 2018. [Online]. Available: https://deepblue.lib.umich.edu/bitstream/handle/2027.42/147732/dweyer%5C_1.pdf?sequence=1.

[18] T. Mitomo, N. Ono, H. Hoshino, Y. Yoshihara, O. Watanabe, and I. Seto, "A 77 ghz 90 nm cmos transceiver for fmcw radar applications," *Solid-State Circuits, IEEE Journal of*, vol. 45, pp. 928–937, May 2010. DOI: 10.1109/JSSC.2010.2040234.

[19] J. W. T. Bruce P. Bogert M. J. R. Healy, "The quefrency analysis of time series for echoes : Cepstrum, pseudo-autocovariance, cross-cepstrum and saphe cracking," 1963.

[20] M. S. Hossain and M. S. Hussain, "A comparative analysis between homodyne and heterodyne receiver architecture," 2016. [Online]. Available: https://api.semanticscholar.org/CorpusID:195728250.

[21] R. Feger, E. Kolmhofer, F. Starzer, F. Wiesinger, S. Scheiblhofer, and A. Stelzer, "A heterodyne 77-ghz fmcw radar with offset pll frequency stabilization," in *2011 IEEE Topical Conference on Wireless Sensors and Sensor Networks*, 2011, pp. 9–12. DOI: 10.1109/WISNET.2011.5725023.

[22] M. Budge and M. Burt, "Range correlation effects on phase and amplitude noise," in *Proceedings of Southeastcon '93*, 1993, 5 p.-. DOI: 10.1109/SECON.1993.465731.

[23] B. Kim, J.-s. Koo, D. Kim, and S. Nam, "A wall-clutter rejection technique using two plls and a phase controller for wall-penetrating fmcw radar," *IEEE Geoscience and Remote Sensing Letters*, vol. 14, no. 4, pp. 471–474, 2017. DOI: 10.1109/LGRS.2016.2643002.

[24] J. Ye, G. Zhou, and H. Liu, "Design and research of improved digital phase-locked loop based on fpga," *Procedia Engineering*, vol. 29, pp. 547–552, Dec. 2012. DOI: 10.1016/j.proeng.2012.01.001.

[25] X. Du and J. Zhang, *Dds phase-locked swept source and study design*, 2011. DOI: 10.1109/ICCSNT.2011.6181928.

[26] M. Edwards, D. Madsen, C. Stringham, A. Margulis, B. Wicks, and D. G. Long, "Microasar: A small, robust lfm-cw sar for operation on uavs and small aircraft," in *IGARSS 2008 - 2008 IEEE International Geoscience and Remote Sensing Symposium*, vol. 5, 2008, pp. V - 514-V –517. DOI: 10.1109/IGARSS.2008.4780142.

[27] E. C. Zaugg, "The byu microsar: Theory and application of a small, lfm-cw synthetic aperture radar," 2015. [Online]. Available: https://api.semanticscholar.org/CorpusID:195178072.

[28] E. Zaugg, M. Edwards, and A. Margulis, "The slimsar: A small, multi-frequency, synthetic aperture radar for uas operation," in *2010 IEEE Radar Conference*, 2010, pp. 277–282. DOI: 10.1109/RADAR.2010.5494612.

[29] E. C. Zaugg, "Generalized image formation for pulsed and lfm-cw synthetic aperture radar," Ph.D. dissertation, Brigham Young University, Apr. 2010. [Online]. Available: https://www.mers.byu.edu/long/theses/phddiss%5C_zaugg.pdf.

[30] W. Chang, H. Tian, and C. Gu, "Fmcw sar: From design to realization," in *2016 IEEE International Geoscience and Remote Sensing Symposium (IGARSS)*, 2016, pp. 1122–1125. DOI: 10.1109/IGARSS.2016.7729284.

[31] *Vbfz-2340+ datasheet*, REV. A ECO-005139, Mini Circuits, P.O. Box 350166, Brooklyn, New York.

[32] *Zx60-272ln-s+: Coaxial low noise amplifier*, Rev. C M171494, Mini Circuits, P.O. Box 350166, Brooklyn, New York.

[33] *Lumped lc band pass filter, 9.5 - 11.5 mhz, 50* Ω, REV. B M151107, Mini Circuits, P.O. Box 350166, Brooklyn, New York.

[34] *14-bit, 125msps/105msps/80msps low power dual adcs*, Linear Technology, Milpitas, California, USA.

[35] J. M. Horrell, "Range-doppler synthetic aperture radar processing at vhf frequencies," Ph.D. dissertation, Dept. of Elec. Eng., University of Cape Town, Cape Town, South Africa, 1999. [Online]. Available: http://hdl.handle.net/11427/16092.

[36] A. W. Doerry, "Performance limits for synthetic aperture radar," Sandia National Laboratories, Albuquerque, New Mexico 87185 and Livermore, California 94550, Tech. Rep., 2006, Second Edition, SAND2006-0821.

[37] C. Stringham, "Developments in lfm-cw sar for uav operation," Ph.D. dissertation, Department of Electrical and Computer Engineering, Brigham Young University, Provo, Utah, USA, Dec. 2014. [Online]. Available: https://www.mers.byu.edu/docs/thesis/phddiss%5C_stringham.pdf.

[38] W. Carrara, R. Goodman, and R. Majewski, *Spotlight Synthetic Aperture Radar: Signal Processing Algorithms* (Artech House remote sensing library). Artech House, 1995, ISBN: 9780890067284. [Online]. Available: https://books.google.co.za/books?id=uztiQgAACAAJ.

[39] A. W. Doerry, "Radar receiver oscillator phase noise," Sandia National Laboratories, Albuquerque, New Mexico 87185 and Livermore, California 94550, Tech. Rep., 2018, SAND2018-3614.

[40] M. Richards, J. Scheer, J. Scheer, and W. Holm, *Principles of Modern Radar: Basic Principles, Volume 1* (Electromagnetics and Radar). Institution of Engineering and Technology, 2010, ISBN: 9781891121524. [Online]. Available: https://books.google.co.za/books?id=nD7tGAAACAAJ.

[41] M. A. Richards, *Fundamentals of Radar Signal Processing*, 2nd ed. Georgia Institute of Technology, USA: McGraw-Hill Education, 2014.

[42] A. W. Doerry and D. L. Bickel, "Antenna requirements for gmti radar systems," Sandia National Laboratories, Albuquerque, New Mexico 87185 and Livermore, California 94550, Tech. Rep., 2020, SAND2020-2378.

[43] W. Stutzman and G. Thiele, *Antenna Theory and Design* (Antenna Theory and Design). Wiley, 2012, ISBN: 9780470576649. [Online]. Available: https://books.google.co.za/books?id=xhZRA1K57wIC.

[44] R. E. Best, *Phase-locked Loops: Design, Simulation and Applications*. McGraw-Hill, 2004.

[45] D. Banerjee, *PLL Performance, Simulation and Design*. Dog Ear Publishing, 2006.

[46] F. Gardner, "Charge-pump phase-lock loops," *IEEE Transactions on Communications*, vol. 28, no. 11, pp. 1849–1858, 1980. DOI: 10.1109/TCOM.1980.1094619.

[47] *Lmx2492/lmx2492-q1 14 ghz low noise fractional n pll with ramp/chirp generation*, SNAS624B, Rev B, 2015 (Revised November 2015), Texas Instruments Incorporated, Mar. 2014.

[48] *9.8ghz to 11.3ghz mmic vco with f0/2 and f0/4 outputs*, RFVC1843, RF Micro Devices, 2013.

[49] S. Pamarti, *Delta-sigma fractional-n pll*, IEEE Solid-State Circuits Society, 2020. [Online]. Available: https://www.youtube.com/watch?v=7Di2jv%5C_rlko.

[50] F. Gardner, *Phaselock Techniques*. Wiley, 2005, ISBN: 9780471732686. [Online]. Available: https://books.google.co.za/books?id=r5yjPuWQde0C.

[51] S.-H. Kim, "Chapter 2 - control of direct current motors," in *Electric Motor Control*, S.-H. Kim, Ed., Elsevier, 2017, pp. 39–93, ISBN: 978-0-12-812138-2. DOI: https://doi.org/10.1016/B978-0-12-812138-2.00002-7. [Online]. Available: https://www.sciencedirect.com/science/article/pii/B9780128121382000027.

[52] D. Banerjee. "Optimizing loop filter bandwidth for modulated pll ramping waveforms." (Feb. 2020), [Online]. Available: https://www.planetanalog.com/optimizing-loop-filter-bandwidth-for-modulated-pll-ramping-waveforms/.

[53] K. Ogata, *Modern Control Engineering* (Instrumentation and controls series). Prentice Hall, 2010, ISBN: 9780136156734. [Online]. Available: https://books.google.co.za/books?id=Wu5GpNAelzkC.

[54] M. Ugarte and A. Carlosena, "Performance comparison and design guidelines for type ii and type iii plls," *Circuits, Systems, and Signal Processing*, vol. 34, Oct. 2015. DOI: 10.1007/s00034-015-0011-y.

[55] R. He, J. Li, W. Rhee, and Z. Wang, "Transient analysis of nonlinear settling behavior in charge-pump phase-locked loop design," in *2009 IEEE International Symposium on Circuits and Systems (ISCAS)*, 2009, pp. 469–472. DOI: 10.1109/ISCAS.2009.5117787.

[56] *Pilot operating handbook*, Issue 4 - Rev.5, COMCO IKARUS GmbH, Hohentengen/Swabia, Germany, 2019. [Online]. Available: https://www.comco-ikarus.de/wp-content/uploads/2019/11/POH-C42-Series-Issue-4-Rev.%5C_5%5C_23.08.2019.pdf.

[57] *Pilot's operating handbook*, Skyhawk, Cessna Model 172M, 1976, Cessna Aircraft Company, Wichita, Kansas, USA, 1976. [Online]. Available: https://www.rochesterair.com/documents/Cessna-172M-POH.pdf.

[58] DJI, *Matrice 30 series - specs*, Accessed Sep. 4, 2022 [Online]. [Online]. Available: https://www.dji.com/matrice-30/specs.

[59] I. Milosavljević, L. Saranovac, and V. Milovanović, "A highly linear and fully-integrated fmcw synthesizer for 60 ghz radar applications with 7 ghz bandwidth," *Analog Integrated Circuits and Signal Processing*, vol. 90, Mar. 2017. DOI: 10.1007/s10470-016-0910-2.

[60] D. Weyer, M. B. Dayanik, L. Jie, *et al.*, "Design considerations for integrated radar chirp synthesizers," *IEEE Access*, vol. 7, pp. 13 723–13 736, 2019. DOI: 10.1109/ACCESS.2019.2893313.

[61] *Phase noise measurement solutions*, Keysight Technologies, Inc., USA, 2018. [Online]. Available: https://www.keysight.com/us/en/assets/7018-02528/technical-overviews/5990-5729.pdf.

[62] "Ieee standard definitions of physical quantities for fundamental frequency and time metrology–random instabilities," *IEEE Std 1139-2008 (Revision of IEEE Std 1139-1999)*, 2009. DOI: 10.1109/IEEESTD.2009.6581834.

[63] S. Miller and D. Childers, *Probability and Random Processes: With Applications to Signal Processing and Communications*. Elsevier Science, 2004, ISBN: 9780121726515. [Online]. Available: https://books.google.co.za/books?id=BVVeTWFhhMsC.

[64] N. Wiener, *Extrapolation, Interpolation, and Smoothing of Stationary Time Series, with Engineering Applications*. Martino Fine Books, 2013, ISBN: 9781614275176. [Online]. Available: https://books.google.co.za/books?id=bqFnngEACAAJ.

[65] N. J. Kasdin, "Discrete simulation of colored noise and stochastic processes and $1/f^{\alpha}$ power law noise generation," 5, vol. 83, Institute of Electrical and Electronics Engineers Inc., May 1995. DOI: 10.1109/5.381848.

[66] P. Welch, "The use of fast fourier transform for the estimation of power spectra: A method based on time averaging over short, modified periodograms," *IEEE Transactions on Audio and Electroacoustics*, vol. 15, no. 2, pp. 70–73, 1967. DOI: 10.1109/TAU.1967.1161901.

[67] M. S. Bartlett and J. Medhi, "ON THE EFFICIENCY OF PROCEDURES FOR SMOOTHING PERIODOGRAMS FROM TIME SERIES WITH CONTINUOUS SPECTRA," *Biometrika*, vol. 42, no. 1-2, pp. 143–150, Jun. 1955, ISSN: 0006-3444. DOI: 10.1093/biomet/42.1-2.143. eprint: https://academic.oup.com/biomet/article-pdf/42/1-2/143/662349/42-1-2-143.pdf. [Online]. Available: https://doi.org/10.1093/biomet/42.1-2.143.

[68] A. Demir, A. Mehrotra, and J. Roychowdhury, "Phase noise in oscillators: A unifying theory and numerical methods for characterization," *IEEE Transactions on Circuits and Systems I: Fundamental Theory and Applications*, vol. 47, no. 5, pp. 655–674, 2000. DOI: 10.1109/81.847872.

[69] L. Lascari, "Accurate phase noise prediction in pll synthesizers here is a method that uses more complete modeling for wireless applications," vol. 12, May 2000.

[70] P. Tschapek, G. Körner, A. Hofmann, C. Carlowitz, and M. Vossiek, "Phase noise spectral density measurement of broadband frequency-modulated radar signals," *IEEE Transactions on Microwave Theory and Techniques*, vol. 70, no. 4, pp. 2370–2379, 2022. DOI: 10.1109/TMTT.2022.3148311.

[71] M. C. Budge and M. P. Burt, "Range correlation effects in radars," *The Record of the 1993 IEEE National Radar Conference*, pp. 212–216, 1993.

[72] M. Adamski, K. Kulpa, M. Nalecz, and A. Wojtkiewicz, "Phase noise in two-dimensional spectrum of video signal in fmcw homodyne radar," in *13th International Conference on Microwaves, Radar and Wireless Communications. MIKON - 2000. Conference Proceedings (IEEE Cat. No.00EX428)*, vol. 2, 2000, 645–648 vol.2. DOI: 10.1109/MIKON.2000.914017.

[73] K. Siddiq, M. K. Hobden, S. R. Pennock, and R. J. Watson, "Phase noise in fmcw radar systems," *IEEE Transactions on Aerospace and Electronic Systems*, vol. 55, no. 1, pp. 70–81, 2019. DOI: 10.1109/TAES.2018.2847999.

[74] A. Stove, "Linear fmcw radar techniques," English, *IEE Proceedings F (Radar and Signal Processing)*, vol. 139, 343–350(7), 5 Oct. 1992, ISSN: 0956-375X. [Online]. Available: https://digital-library.theiet.org/content/journals/10.1049/ip-f-2.1992.0048.

[75] S. Goldman, *Phase Noise Analysis in Radar Systems Using Personal Computers*. Wiley, 1989, ISBN: 9780471618942. [Online]. Available: https://books.google.co.za/books?id=ZzUfAQAAIAAJ.

[76] *Coaxial cable s_04162_b-60*, Application Note AN-1879, HUBER_SUHNER Incorporated, 8530 Steele Creek Place Drive, Suite H Charlotte, NC 28273, USA, 2016. [Online]. Available: https://www.datasheets.com/en/part-details/s-04162-b-60-huber-suhner-52670585#datasheet.

[77] S. J. Orfanidis, "Electromagnetic waves and antennas,"

[78] R. Lyons, *Understanding Digital Signal Processing*. Pearson Education, 2010, ISBN: 9780137028528. [Online]. Available: https://books.google.co.za/books?id=UBU7Y2tpwWUC.

[79] RedPitaya, *Stemlab 125-14 external clock*, Accessed: April 4, 2024. [Online]. Available: https://redpitaya.readthedocs.io/en/latest/developerGuide/hardware/125-14%5C_EXT/top.html.

[80] Y. Li and S. O'Young, "Focusing bistatic fmcw sar signal by range migration algorithm based on fresnel approximation," *Sensors*, vol. 15, no. 12, pp. 32 123–32 137, 2015, ISSN: 1424-8220. DOI: 10.3390/s151229910. [Online]. Available: https://www.mdpi.com/1424-8220/15/12/29910.